Dalitz Plot Analysis of $B^0 \to K^+\pi^-\pi^0$ Decays at the Belle II Experiment

Markus Reif

München 2024

Dalitz Plot Analysis of $B^0 \to K^+\pi^-\pi^0$ Decays at the Belle II Experiment

Markus Reif

Dissertation
an der Fakultät für Physik
der Ludwig-Maximilians-Universität
München

vorgelegt von
Markus Reif
aus Nürnberg

München, den 1. August 2024

Erstgutachter: Prof. Dr. Thomas Kuhr
Zweitgutachter: Prof. Dr. Christian Kiesling
Tag der mündlichen Prüfung: 26. September 2024

Zusammenfassung

Diese Arbeit präsentiert Bestimmungen des Verzweigungsverhältnisses ($\mathcal{B}$) und der *CP*-verletzenden Ladungsasymmetrie ($\mathcal{A}^{CP}$) des Dreikörperzerfalls $B^0 \to K^+\pi^-\pi^0$ am Belle II Experiment. Zusätzlich zum inklusiven $\mathcal{B}$ und der $\mathcal{A}^{CP}$, d.h. $B^0 \to K^+\pi^-\pi^0$, messen wir $\mathcal{B}$ und $\mathcal{A}^{CP}$ exklusiv für individuelle Zweikörperresonanzen, die im $K^+\pi^-\pi^0$ System auftreten. Hierfür verwenden wir eine modellabhängige Dalitzplot-Messung mit den sieben dominierenden Zwischenresonanzen und einer nicht-resonanten Komponente. Die analysierten Daten wurden zwischen 2019 und 2022 aufgenommen und entsprechen einer integrierten Luminosität von $362\,\mathrm{fb}^{-1}$, produziert in e^+e^- Kollisionen bei der $\Upsilon(4S)$ Resonanz vom SuperKEKB Beschleuniger und enthalten 387×10^6 Bottom-Antibottom Mesonenpaare. Die Analyse wurde ausschließlich auf simulierten Daten und Kontrollkanälen entwickelt. Die Verzweigungsverhältnisse und *CP*-Asymmetrien werden in einem vier-dimensionalen erweiterten Maximum-Likelihood Fit bestimmt. Da die Analyse noch in der Belle II internen Überprüfung ist, verdecken wir die Zentralwerte und geben nur deren Unsicherheiten an. Wir messen das Verzweigungsverhältnis und die *CP*-verletzende Ladungsasymmetrie inklusiv, sowie exklusiv für die Kanäle $B^0 \to K^*(892)^+\pi^-$, $B^0 \to K^*(892)^0\pi^0$, $B^0 \to \rho(770)^-K^+$, $B^0 \to (K\pi)_0^{*+}\pi^-$, $B^0 \to (K\pi)_0^{*0}\pi^0$, $B^0 \to \rho(1450)^-K^+$, $B^0 \to \rho(1700)^-\pi^0$ und $B^0 \to K^+\pi^-\pi^0$ nicht-resonant.

Diese Arbeit stellt die erste modellabhängige Dalitplot-Analyse bei Belle II dar. Wir erreichen Unsicherheiten auf Augenhöhe mit früheren Messungen. Die $B^0 \to K^*(892)\pi$ Kanäle sind Input für eine Summenregel, basierend auf dem Isospin, um das Standardmodell zu testen.

Abstract

This thesis reports a determination of the branching fraction ($\mathcal{B}$) and *CP*-violating charge asymmetry ($\mathcal{A}^{CP}$) of the three-body decay $B^0 \to K^+\pi^-\pi^0$ at the Belle II experiment. In addition to the inclusive $\mathcal{B}$ and $\mathcal{A}^{CP}$, i.e. for $B^0 \to K^+\pi^-\pi^0$ decays, we measure $\mathcal{B}$ and $\mathcal{A}^{CP}$ exclusively for individual two-body resonances appearing in the $K^+\pi^-\pi^0$ system. To this end, we employ a model dependent Dalitz plot analysis, including the seven dominant intermediate resonances and a non-resonant contribution. The analyzed data were recorded between 2019 and 2022 and correspond to an integrated luminosity of $362\,\mathrm{fb}^{-1}$ produced in e^+e^- collisions at the $\Upsilon(4S)$ resonance by the SuperKEKB collider containing 387×10^6 pairs of bottom-antibottom mesons. The analysis is developed on simulated data and control mode data solely. The branching fractions and *CP*-asymmetries are extracted in a four-dimensional extended maximum likelihood fit. As the analysis is still under Belle II internal review, we blind central values and state uncertainties only. We measure the branching fraction and *CP*-violating charge asymmetry inclusively as well as exclusively for the channels $B^0 \to K^*(892)^+\pi^-$, $B^0 \to K^*(892)^0\pi^0$, $B^0 \to \rho(770)^-K^+$, $B^0 \to (K\pi)_0^{*+}\pi^-$, $B^0 \to (K\pi)_0^{*0}\pi^0$, $B^0 \to \rho(1450)^-K^+$, $B^0 \to \rho(1700)^-\pi^0$ and $B^0 \to K^+\pi^-\pi^0$ non-resonant.

This thesis presents the first model dependent Dalitz plot analysis at Belle II. We achieve uncertainties on par with known determinations. The $B^0 \to K^*(892)\pi$ modes will serve as inputs for a sum rule based on isospin to probe the Standard Model.

Contents

List of Figures

List of Tables

List of Abbreviations

basf2 Belle II Analysis Software Framework.

ARICH Aerogel Ring-Imaging CHerenkov.
AUC area under curve.

CDC Central Drift Chamber.
CKM Cabibbo-Kobayashi-Maskawa.

DEPFET DEpleted P-channel Field Effect Transistor.

ECL Electromagnetic CaLorimeter.

GBDT gradient boosted decision tree.

HAPD Hybrid Avalanche Photo-Detector.
HER high-energy ring.

IP interaction point.

KDE kernel density estimation.
KLM K_L^0 and μ detector.

LER low-energy ring.
LHC Large Hadron Collider.
LS1 long shutdown 1.

PDF probability density function.
PID particle identification.
PMT photo-multiplier tube.
PXD Pixel Vertex Detector.

QCD quantum chromodynamics.

ROC receiver operating characteristic.
RPC resistive plate chamber.

SCF self-cross-feed.
SiPM silicon photomultiplier.
SM Standard Model.
SVD Silicon Vertex Detector.

TM truth-matched.
TOP Time-Of-Propagation.

VXD Vertex Detector.

1 Introduction

The Standard Model (SM), at present, is our best theoretical framework of the fundamental particles and their interactions (excluding gravity). It beautifully describes all our current experimental observations of the microscopic world, with remarkable precision. Have we therefore found the ultimate theory of our universe? The answer is "No". Plenty of observed phenomena are not described within the SM. For example, in our universe the visible matter, which is described by the SM, accounts for only about 5% of the total energy content, 25% is made up by dark matter and the remaining 70% are dark energy [1], both of which we have no experimentally confirmed explanation for.

Also, visible matter exhibits features the SM cannot explain. One of them is the asymmetry between the amount of matter and antimatter in our universe. According to the "hot Big Bang" scenario about 13.8 billion years ago, equal amounts of matter and antimatter were created. Matter and antimatter particles should have annihilated each other during the early expansion phase, asserting that today's universe should only contain radiation. However, there are large structures such as galaxies, stars and planets, all of them being matter. Therefore the antimatter must have disappeared somehow, before annihilating all matter, i.e. there must be some fundamental differences in the way matter and antimatter behave. The physical term for this difference in behavior is charge-parity (CP) violation. The SM allows for some small CP-violating effects, but they are not sufficient to explain the observed matter-antimatter asymmetry [2].

In the last decade the focus in high energy particle physics has therefore shifted from confirming the Standard Model to the search for physics beyond. In high-energy particle physics, there are two approaches to find physics beyond the SM, also called "new physics". Experiments at the Large Hadron Collider (LHC) (such as Atlas or CMS) are operating at the energy frontier, aiming to directly produce new particles in high energy collisions. A more subtle approach is chosen at the intensity frontier. Instead of directly creating new particles, the goal is to measure SM parameters very precisely. New heavy particles could contribute to processes as virtual particles in quantum loops and modify the SM predictions even at collision energies below their mass limits. However these virtual contributions are highly suppressed with respect to SM processes. In order to measure such small effects large datasets ("intensity frontier") are needed.

A state-of-the-art experiment at the intensity frontier is Belle II located in Tsukuba, Japan. It is primarily aimed at studying the B-meson and its decays. B-meson decays are of great interest for SM studies in particular due to their large CP-violating effects. At Belle II, pairs of B-mesons are produced in the collisions of electrons and positrons, which are provided by the high luminosity SuperKEKB accelerator. The high luminosity should be achieved by a new beam focusing technique, squeezing the electron and positron bunches to nano-meter scales, i.e. the bunch density is increased. This results in more

e^+e^- collision per time, such that a large dataset of B-mesons can be collected in a short time.

B-mesons can decay to various different final states, characterized by weak transformations of a b quark inside the B-meson to one of the lighter quarks, such as c, s, u or d. One class of decays is called charmless. Here, the B-meson decays to final state hadrons which do not contain a charm quark. These decays are dominated by loop transitions, in which additional new particles can contribute, and hence are potentially sensitive to new physics. However, as there are complex interactions in the hadronic final states, governed by strong interactions, the accuracy of theory predictions is limited. Internal symmetries such as isospin[1] can be exploited in related decay modes to cancel theory uncertainties and create so-called isospin sum rules. One example of four isospin related modes are the decays $B^0 \to K^{*+}\pi^-$, $B^0 \to K^{*0}\pi^0$, $B^+ \to K^{*+}\pi^0$ and $B^+ \to K^{*0}\pi^+$. We utilize K^* as abbreviation of $K^*(892)$ and imply charge-conjugation throughout this thesis unless stated otherwise. The sum rule requires the measurement of branching fractions and direct CP-violation of all four modes [3]. The Belle II experiment recently tested the $K\pi$ isospin sum rule to be in agreement, within the experimental uncertainties, with the SM prediction [4]. At present, the measurement is limited by the large statistical uncertainties and it remains to be shown whether the sum rule holds if performed on larger datasets.

The $K^*\pi$ isospin sum rule, until now, has not been tested experimentally. The K^* meson is an exited state (resonance) of the K-meson, i.e. it further decays into a kaon and a pion. Therefore, we cannot directly measure properties of the K^*. Instead, we measure decays into final states that can proceed via intermediate K^* resonances. One example is the $B^0 \to K^+\pi^-\pi^0$ decay, which is analyzed in this thesis. This decay can proceed via two of the four $K^*\pi$ modes, namely $B^0 \to K^{*0}\pi^0$ and $B^0 \to K^{*+}\pi^-$. However, these are not the only occurring resonances. Further resonances like ρ^- or K_0^* also contribute and interfere with each other. In order to disentangle all the resonance contributions we need to model the overall $B^0 \to K^+\pi^-\pi^0$ decay amplitude. We uses the isobar formalism, where the B^0 decay is modeled as subsequent two-body decays with intermediate resonances. We include seven resonances and one non-resonant[2] contribution. In B-meson decays to three pseudo-scalar (i.e. spin-parity=0^-) particles, the amplitude is only a function of two invariant masses squared. The two dimensional distribution of these invariant masses squared is called Dalitz plot, owing to its "inventor" Richard H. Dalitz [5, 6]. Therefore, this type of analysis are nowadays called Dalitz plot analysis. The goal of this thesis is to perform a $B^0 \to K^+\pi^-\pi^0$ Dalitz plot analysis to measure the branching fractions and CP-violating charge asymmetries of all considered modes, in particular the ones of the $B^0 \to K^{*0}\pi^0$ and $B^0 \to K^{*+}\pi^-$ decays, to provide the inputs for the $K^*\pi$ isospin sum rule. The analyzed data correspond to an integrated luminosity of $362\,\text{fb}^{-1}$, which are 387×10^6 B-meson pairs.

A similar analysis was conducted in a PhD thesis at the Belle experiment, in 2014, using the entire data sample of Belle II's predecessor experiment Belle, which is about two times the size of the dataset used in this thesis [7]. However, this analysis was not

[1] Isospin describes an internal symmetry of strong interactions to characterize different particles that or not distinguishable by strong interactions, e.g. protons and neutrons.

[2] Non-resonant means that the B^0 directly decays to $K^+\pi^-\pi^0$ without an intermediate resonance.

published in any journal. The most precise measurement of $B^0 \to K^+\pi^-\pi^0$ decays was published in 2011 by the *BABAR* experiment [8] using a dataset $\sim 14\%$ larger than the dataset used in this analysis. This thesis presents the first model dependent Dalitz plot analysis at the Belle II experiment and follows similar strategies as the ones used in the two aforementioned analysis. We aim to improve the precision by utilizing the expected large Belle II dataset and state-of-the-art analysis techniques.

The following summarizes the contents of this thesis:

Chapter 2 introduces the Standard Model and concepts like *CP*-violation, focusing on flavor physics and B-meson decays.

Chapter 3 elucidates the Dalitz plot analysis formalism and the amplitude model used in this thesis.

Chapter 4 introduces the experimental setup including the SuperKEKB collider, the Belle II experiment and its sub-systems.

Chapter 5 summarizes how the B-mesons are reconstructed from final state particles and how we suppress backgrounds.

Chapter 6 presents the fit model to extract the physics parameters of interest.

Chapter 7 shows tests to validate the fit model.

Chapter 8 covers corrections we apply to account for differences between simulated data and real data.

Chapter 9 explains the systematic uncertainties we consider.

Chapter 10 shows the final results of this thesis.

A simple one page flow diagram depicting the main steps of the analysis part is shown in the Appendix in Figure A.1.

2 The Standard Model of Particle Physics

The SM is a quantum field theory consistent with quantum mechanics and special relativity. It describes our current knowledge of elementary particles in the universe and three of the four fundamental forces, i.e. the weak, the strong and the electromagnetic force. The attempt of the unification of the last fundamental force, gravity, described by general relativity, and the SM is called quantum gravity and poses one of the main challenges in todays theoretical particle physics [9]. However, the Standard Model is lacking explanations for some observations. One of such is that the surveyed rotational speed of galaxies differs from the one calculated with all the visible (luminous) matter. Adding additional invisible (non-luminous) mass resolves the difference [10]. The Standard Model has no good candidate for this additional mass, called dark matter.

Despite its limitations, the Standard Model has, thus far, passed all experimental validations with remarkable accuracy. This chapter will give a general introduction of the SM, briefly describing its mathematically concepts. Following, flavor physics is discussed to pave the way towards the measurement performed in this thesis. Finally, studies of charmless hadronic B-meson decays (e.g. $B^0 \to K^+\pi^-\pi^0$) are motivated and their current experimental and theoretical status are summarized. This chapter is mainly based on the standard works [11], [12] and [13].

2.1 Elementary Particles

In the SM there are two types of fundamental particles. Matter consists of fermions, which have spin one-half. They interact via quantized fields, of which they are the sources. The corresponding particles of the interaction fields are bosons with integer spin [11]. An illustration of all fundamental particles is shown in Figure 2.1. Fermions are sub-grouped into quarks and leptons. Interestingly, experimental observations suggest that both have three generations. The six quarks come in u- and d-types, i.e. in doublets of weak isospin. The u-type quarks carry an electric charge of $+\frac{2}{3}$, while d-type quarks have an electric charge of $-\frac{1}{3}$. Quarks also carry a so-called color charge, which allows them to couple via the strong interaction. They don't exist as individual particles, but always form colorless bound states called hadrons. Examples are protons (u, u, d) and neutrons (u, d, d), which form atomic nuclei. Particles containing three quarks are called baryons. Particles like the B^0 ($\overline{b}$, d), which contain a quark and an antiquark, are called mesons. The quarks within a hadron can differ in their internal configuration. For mesons containing an u and an $\overline{s}$ quark the ground state is called K^+ meson. Here, the spins of both quarks are aligned anti-parallel and there is no angular momentum between the two of them (S-wave), such that the total spin is zero. Its mass is $494\,\mathrm{MeV}/c^2$. The first excited state of the K-meson, the $K^*(892)$-meson contains the same quarks, but the spins are aligned parallel, such that

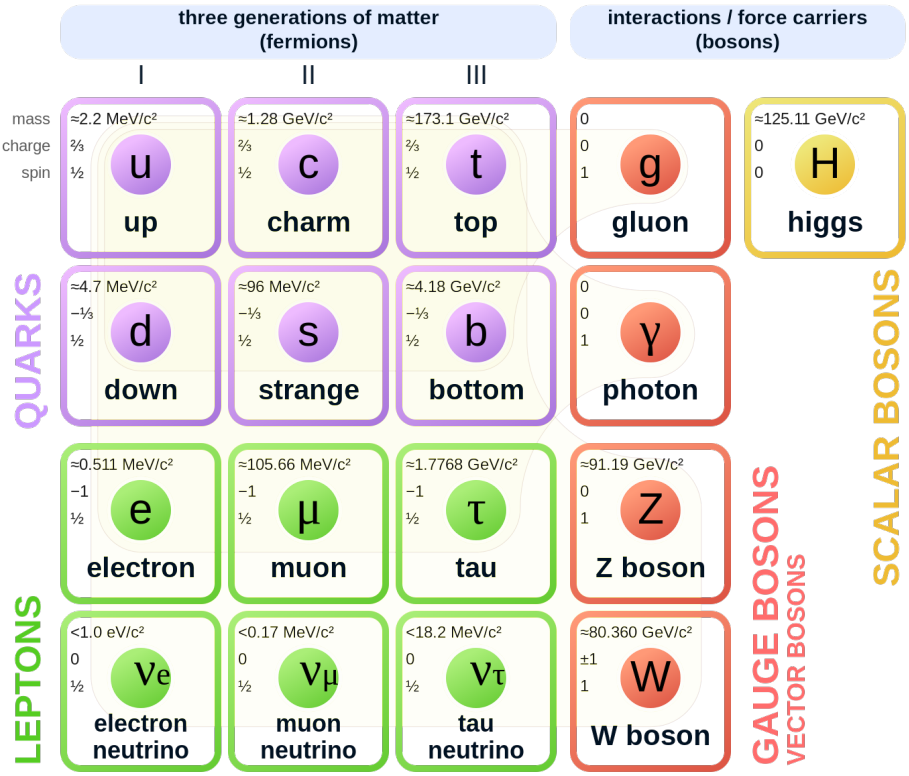

Figure 2.1: Illustration of the elementary particles described by the SM [14].

the total spin is one. Its mass is $892\,\mathrm{MeV}/c^2$ [15]. Adding angular momentum or radial excitations between the quarks yields plenty more excited kaon states. Since they are excited, the will decay via the strong interaction to their ground state.

The leptons also come in doublets of weak isospin, with electric charge -1 and its corresponding neutral neutrino. They do not carry any color charge and hence the charged leptons only interact electromagnetically and weakly, and the neutrinos only weakly.

The bosons are the mediators of the forces. The gluon and the photon are the interaction particles of the strong force and the electromagnetic force, while the Z and W boson are the mediators of weak interactions. The spin zero Higgs boson interacts only weakly and is responsible for giving mass to the quarks, leptons and weak bosons (see next section). Both gluons and photons are massless.

2.2 Gauge Symmetries and Mass-Generation of Particles

Mathematically the Standard Model is formulated in terms of the $SU(3)_C \otimes SU(2)_L \otimes U(1)_Y$ gauge symmetry, where $SU(3)_C$ is the symmetry group for the strong interaction described by quantum chromodynamics (QCD). The subscript C is the color charge which can take three values (red, green, blue). $SU(2)_L \otimes U(1)_Y$ describes the combination of

electromagnetic and weak interaction with L being the weak isospin and Y the weak hyper-charge.

Each force is formulated via a so-called *Lagrangian*. For example the Lagrangian for non-relativistic mechanics is given by

$$L = T - V, \tag{2.1}$$

where T is the kinetic and V the potential energy of the system. *The Euler-Lagrange equation of motion* is then given as

$$\frac{d}{dt}(\frac{\partial L}{\partial \dot{q}} - \frac{\partial L}{\partial q}) = 0 \tag{2.2}$$

where q is the coordinate describing the system, which is a function of time. $\dot{q}$ is the derivative of the coordinate with respect to time [16].

The term gauge symmetry refers to some invariance of physical laws under transformations. A global gauge symmetry requires that a physical process is unaffected by any translation in space-time. This means for example an asteroid hitting the earth 65 million years ago follows the same rules as any other asteroid hitting any other planet in the universe at any other time. Following Emmy Noether's theorem [17] each such global symmetry results in a conserved quantity. Momentum is the conserved quantity due to translational invariance. Other symmetries give rise to the conservation of e.g. charge, energy and angular momentum.

One fundamental principle used to build the SM is local gauge invariance. Here, transformations are made dependent on space-time. A priori a Lagrangian is not invariant under such transformations. To recover gauge invariance, gauge fields are introduced. These gauge fields or gauge bosons are the force carriers of the respective interaction.

The mathematically introduced gauge fields are massless. However, we experimentally know that the bosons of the weak interaction (i.e. W and Z boson) are massive, which again breaks the local gauge invariance [13]. The issue of having massive bosons while retaining gauge invariance was solved by the Higgs mechanism [18]. An additional complex scalar field (the Higgs boson) is introduced, which is spontaneously broken in the $SU(2)_L \otimes U(1)_Y$ electroweak symmetry. This results in an additional mass term for the weak bosons. Fermions acquire their masses by coupling them to the Higgs field, which is called Yukawa coupling [12].

2.3 Flavor Physics

Flavor Physics explores one of the most exciting sub-fields of particles physics. 'Flavor' refers to the different types of quarks (and leptons). In the Standard model there are six different flavors of quarks, namely u, d, c, s, b and t quark. Flavor physics processes are governed by weak interactions, which has the peculiarity of changing flavors. One of the most famous processes of this kind is the so-called beta decay of a neutron to a proton, where one d quark is transformed by the weak interaction into an u quark.

2.3.1 Discrete Symmetries

What makes weak interactions particularly interesting are its properties under certain transformations, known as discrete symmetries.

Parity

The first such symmetry is called parity. A parity transformation $\hat{P}$ flips the sign of spatial coordinates [13]. For example for a three vector

$$\hat{P}\begin{pmatrix} x \\ y \\ z \end{pmatrix} = \begin{pmatrix} -x \\ -y \\ -z \end{pmatrix}. \tag{2.3}$$

In 1956 T.D. Lee and C.N. Yang proposed that parity is violated in weak decays to solve the so-called τ-θ puzzle [19]. The puzzle concerns the τ^+- and θ^+- mesons having the same mass and lifetime, but the τ^+ decays into two pions which is P-even, while the θ^+ decays into three pions which is P-odd. If parity was conserved in weak decays they must be different particles. However, T.D. Lee and C.N. Yang suggested that they were the same particle[1] and weak interactions violate parity.

Just one year later, in 1957, C.S. Wu was able to experimentally prove that parity is indeed violated in weak decays, by observing the direction of emission of the created electron in the weak beta decay of ^{60}Co [20] (For details see [13]). Nowadays we know that parity is not only partially but maximally violated in weak decays. This means only left-handed (momentum and spin are aligned anti-parallel) fermions and right-handed (momentum and spin are aligned parallel) anti-fermions couple to the W boson. As consequence neutrinos, which only interact weakly, are all left-handed. A potential right-handed neutrino cannot be created as it does not couple weakly (i.e. it does not exist in the SM). Mass generation through Yukawa coupling requires a left- and right-handed component, hence neutrinos are massless in the Standard Model [12].

Charge Conjugation

A charge transformation $\hat{C}$ converts a particle in its antiparticle, and by this for example the electric charge [13]. Plainly, this means that under charge conjugation a particle is transformed into its anti-particle.

Time Reversal and CPT-Theorem

Time reversal $\hat{T}$ inverts the time coordinate. Physical processes that are invariant under $\hat{T}$ can go back in the past or in the same way in the future [13]. The CPT-Theorem states that any relativistic quantum field theory, such as the Standard Model, is invariant under a combined $\hat{C}$, $\hat{P}$ and $\hat{T}$ transformation [21]. As already mentioned $\hat{P}$ is maximally violated

[1] As parity is violated in weak decays the τ^+ and θ^+ mesons are the same particle and we nowadays call it K^+-meson

in weak interactions. To restore the combined symmetry of $\widehat{CPT}$, also $\widehat{CT}$ must be broken maximally. Furthermore, other symmetries are broken in weak interactions, one of which is $\widehat{CP}$, as explained in the following.

2.3.2 Charge-Parity Symmetry

After discovering parity is violated in weak interactions, physicists investigated the behavior of the combined transformation of charge and parity. Applying $\hat{C}$ on a left-handed neutrino yields a left-handed anti-neutrino, which does not exist in the SM. Consecutively applying $\hat{P}$ changes the handedness of the anti-neutrino, making it right handed, which again is allowed in the SM (see Fig. 2.2).

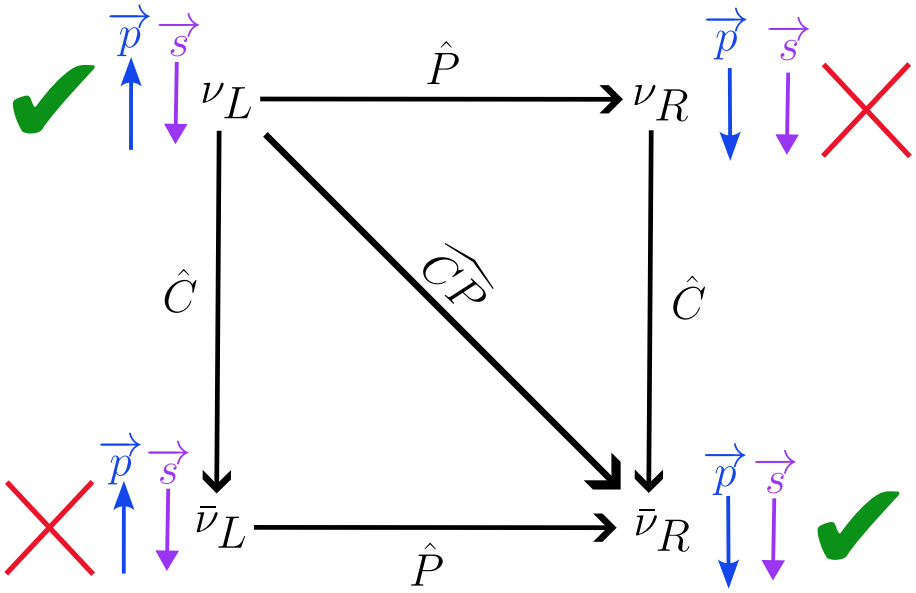

Figure 2.2: Illustration of a combined $\widehat{CP}$ transformation on a left-handed neutrino yielding a right-handed anti-neutrino.

2.3.3 Discovery of *CP*-Violation

In 1964 Christenson, Cronin, Fitch, and Turlay performed an experiment studying the behavior of *CP*-symmetry in the decay of neutral kaons [22]. The two neutral kaon states are $|K^0\rangle = |d\bar{s}\rangle$ and $|\overline{K}^0\rangle = |\bar{d}s\rangle$. One can construct the *CP*-eigenstates as follows

$$|K_1\rangle = \frac{1}{\sqrt{2}}(|K^0\rangle - |\overline{K}^0\rangle) \tag{2.4}$$

$$|K_2\rangle = \frac{1}{\sqrt{2}}(|K^0\rangle + |\overline{K}^0\rangle), \tag{2.5}$$

where $|K_1\rangle$ is *CP*-odd and $|K_2\rangle$ is *CP*-even. At the time of the experiment two neutral kaon states were know, which differed by their lifetime. The short lived $|K_S\rangle$ was observed

to decay into two pions, which is *CP*-even, and the long lived $|K_L\rangle$ was observed to decay into three pions, which is *CP*-odd. Therefore, they were linked to the *CP*-even and *CP*-odd state from above:

$$|K_L\rangle = |K_1\rangle \quad (\tau_L = 0.5 \cdot 10^{-7} s) \tag{2.6}$$
$$|K_S\rangle = |K_2\rangle \quad (\tau_S = 0.9 \cdot 10^{-10} s). \tag{2.7}$$

If *CP* is conserved in these decays, i.e. $|K_S\rangle$ and $|K_L\rangle$ are *CP*-eigenstates, the short lived neutral kaon *only* decays to two pions, while the long lived kaon *only* decays into three pions. In the experiment a neutral kaon beam, being a superposition of $|K_S\rangle$ and $|K_L\rangle$, was allowed to decay over a long distance before the actual experiment observing the decay products. Given the shorter lifetime all $|K_S\rangle$ have decayed eventually. At the end of the long decay path only $|K_L\rangle$ states should exist and only three pion decays should be observed. However, out of 22 700 observed events, 45 were two pion decays. Hence, $|K_S\rangle$ and $|K_L\rangle$ are not pure *CP*-eigenstates but a superposition as

$$|K_S\rangle = \frac{1}{\sqrt{1+|\epsilon|}}(K_1 + \epsilon K_2) \tag{2.8}$$
$$|K_L\rangle = \frac{1}{\sqrt{1+|\epsilon|}}(K_2 + \epsilon K_1). \tag{2.9}$$

$|\epsilon|$ determines the strength of *CP*-violation and is experimentally measured to be $|\epsilon| = (2.228 \pm 0.011) \times 10^{-3}$ [23], meaning about two in 1000 neutral kaon decays violate the *CP*-symmetry. (For more details, see the Nobel lectures [24] and [25]).

2.3.4 CKM-Matrix

As *CP*-violation was experimentally observed a theory was needed incorporating such processes. Within the framework of the SM a solution was proposed by Kobayashi and Maskawa [26], where the transition probabilities of quarks are encoded in the so-called Cabibbo-Kobayashi-Maskawa (CKM)-matrix, V_{CKM}. Algebraically, the CKM-matrix rotates between the mass eigenstates of strong interactions and the flavor eigenstates of the weak interaction. Plainly it describes how likely it is for a d-type quark to transform into an u-type quark (or vice versa).

The first to realize that strong and weak eigenstates are distinct was Nicola Cabibbo. He introduced an angle, today known as Cabibbo-angle θ_C, for quark transitions among u, d and s quarks, which were the only known quarks at the time [27].

To explain the strong suppression of flavor-changing-neutral-currents in the SM Glashow, Iliopoulos, and Maiani proposed the existence of the charm quark through the GIM-mechanism [28]

$$\begin{pmatrix} d' \\ s' \end{pmatrix}_{weak} = \begin{pmatrix} \cos\theta_C & \sin\theta_C \\ -\sin\theta_C & \cos\theta_C \end{pmatrix} \begin{pmatrix} d \\ s \end{pmatrix}_{mass} = \begin{pmatrix} V_{ud} & V_{us} \\ V_{cd} & V_{cs} \end{pmatrix} \begin{pmatrix} d \\ s \end{pmatrix}_{mass}. \tag{2.10}$$

This was then extended by Kobayashi and Maskawa for a third generation [26]

$$\begin{pmatrix} d' \\ s' \\ b' \end{pmatrix}_{weak} = \begin{pmatrix} V_{ud} & V_{us} & V_{ub} \\ V_{cd} & V_{cs} & V_{cb} \\ V_{td} & V_{ts} & V_{tb} \end{pmatrix} \begin{pmatrix} d \\ s \\ b \end{pmatrix}_{mass} = V_{\mathrm{CKM}} \begin{pmatrix} d \\ s \\ b \end{pmatrix}_{mass} . \tag{2.11}$$

A 3×3-matrix with complex entries contains 18 free parameters. Assuming only three generations of quarks the CKM-matrix is unitary

$$V^\dagger V = \mathbb{1}. \tag{2.12}$$

This yields the following conditions for the diagonal elements

$$\sum_{k=1}^{3} = |V_{ik}|^2 \stackrel{!}{=} 1 \quad (i = 1, 2, 3) \tag{2.13}$$

and

$$\sum_{k=1}^{3} V_{jk}^* V_{ik} \stackrel{!}{=} 0 \quad (i > j) \tag{2.14}$$

for the off-diagonal elements [13]. These are nine equations, i.e. removes nine of the 18 degrees of freedom. The three equations for the off-diagonal elements of the upper half of the CKM-matrix read explicitly

$$V_{ud}V_{us}^* + V_{cd}V_{cs}^* + V_{td}V_{ts}^* = 0, \tag{2.15}$$

$$V_{ud}V_{ub}^* + V_{cd}V_{cb}^* + V_{td}V_{tb}^* = 0, \tag{2.16}$$

$$V_{us}V_{ub}^* + V_{cs}V_{cb}^* + V_{ts}V_{tb}^* = 0. \tag{2.17}$$

These equations represent triangles, known as unitarity triangles. An illustration of Equation 2.16 is shown in Figure 2.3.

Its angles α, β and γ are given by

$$\alpha = \arg\left(-\frac{V_{td}V_{tb}^*}{V_{ud}V_{ub}^*}\right), \quad \beta = \arg\left(-\frac{V_{cd}V_{cb}^*}{V_{td}V_{tb}^*}\right), \quad \gamma = \arg\left(-\frac{V_{ud}V_{ub}^*}{V_{cd}V_{cb}^*}\right). \tag{2.18}$$

Typically, this triangle is normalized to $V_{cd}V_{cb}^*$ as shown in Figure 2.4. In literature this is often referred to as "the" unitarity triangle.

From the remaining nine free parameters of the CKM-matrix five are phases which have no physical meaning, and can be absorbed in the quark fields. This leaves four free parameters. Typically, three mixing angles θ_{12}, θ_{23} and θ_{13} and a phase factor δ are chosen such that V_{CKM} can be written as

$$V_{CKM} = \begin{pmatrix} c_{12}c_{13} & s_{12}c_{13} & s_{13}e^{-\mathrm{i}\delta} \\ -s_{12}c_{23} - c_{12}s_{23}s_{13}e^{\mathrm{i}\delta} & c_{12}c_{23} - s_{12}s_{23}s_{13}e^{\mathrm{i}\delta} & s_{23}c_{13} \\ s_{12}s_{23} - c_{12}s_{23}s_{13}e^{\mathrm{i}\delta} & -c_{12}s_{23} - s_{12}c_{23}s_{13} & c_{23}c_{13} \end{pmatrix} \tag{2.19}$$

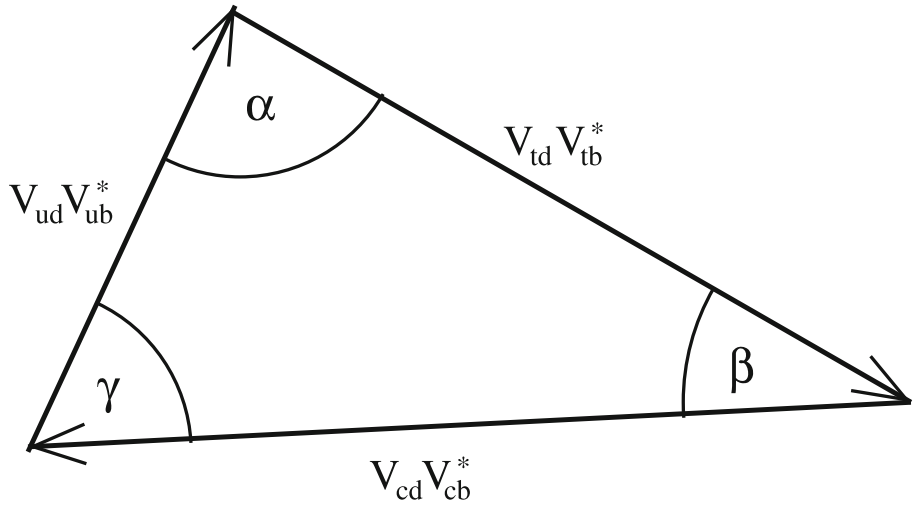

Figure 2.3: Illustration of the unitarity condition 2.16 as a triangle [29].

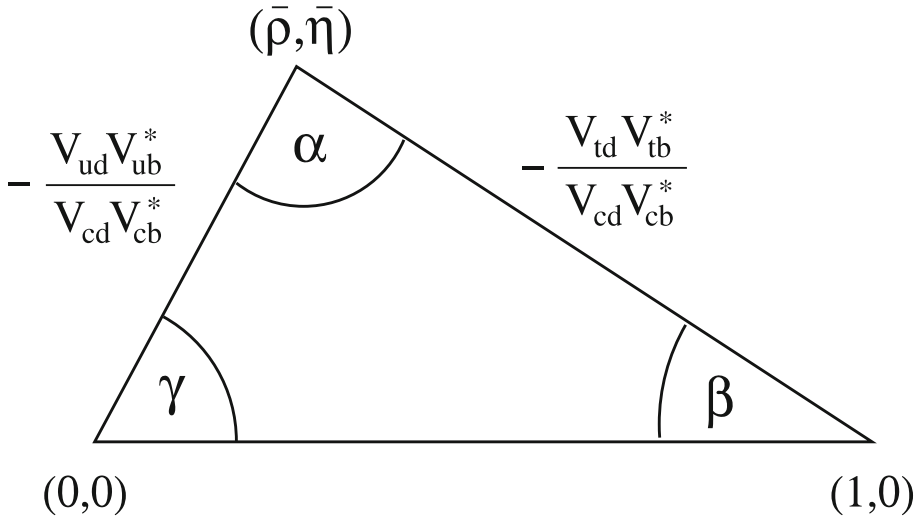

Figure 2.4: Illustration of "the" unitarity triangle normalized to $V_{cd}V_{cb}^*$ [29].

where $s_{ij} = \sin\theta_{ij}$ and $c_{ij} = \cos\theta_{ij}$ [29]. As will be shown in the next section, the irreducible phase δ is a necessary condition for *CP*-violation and requires, according to Kobayashi and Maskawa, at least 3 generations of quarks. On of the main goals of Flavor Physics is to measure the elements and angles of the unitarity triangle to over-constrain it. If the values obtained from experiments do not form a perfect triangle, it would be a definitive indication of new physics beyond the Standard Model.

Another widely used representation of the CKM-matrix is given by the Wolfenstein parametrization [30]. Here the elements are expanded in terms of $\lambda = |V_{us}| = \sin\theta_C = 0.22$

such that the CKM-matrix can be written as

$$V_{CKM} = \begin{pmatrix} 1-\frac{1}{2}\lambda^2 & \lambda & A\lambda^3(\rho - \mathrm{i}\eta) \\ -\lambda & 1-\frac{1}{2}\lambda^2 & A\lambda^2 \\ A\lambda^3(1-\rho-\mathrm{i}\eta) & -A\lambda^2 & 1 \end{pmatrix} + \mathcal{O}(\lambda^4) \tag{2.20}$$

with $s_{23} = A\lambda^2$ and $s_{13}e^{-\delta_{13}} = A\lambda^3(\rho - i\eta)$ [31]. The only components that possess a significant phase, represented by $i\eta$, are V_{ub} and V_{td}. These components describe the transitions from the third to the first generation of quarks, e.g. decays of B-mesons, suggesting large *CP*-violating effects in these decays [29].

2.3.5 Types of *CP*-Violation

Nowadays, we distinguish three types of *CP*-violation, which will be shortly introduced in the following.

Violation in Decays

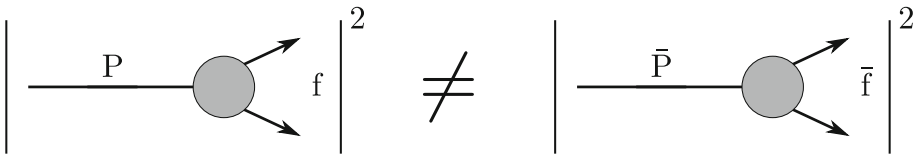

Figure 2.5: *CP*-violation in decays or direct *CP*-violation [32].

The first type of *CP*-violation is known as violation in decay, or direct *CP*-violation. This occurs when the following condition is met:

$$\left|\frac{\bar{\mathscr{A}_{\bar{f}}}}{\mathscr{A}_f}\right| \neq 1 \tag{2.21}$$

Here, $\mathscr{A}_f$ and $\bar{\mathscr{A}_{\bar{f}}}$ denote the decay amplitudes for $\mathrm{P} \to \mathrm{f}$ and its *CP*-conjugate $\bar{\mathrm{P}} \to \bar{\mathrm{f}}$, respectively. This means that the decay rate $\Gamma(\mathrm{P} \to \mathrm{f})$ of a particle (P) into a final state (f) differs from the decay rate $\Gamma(\bar{\mathrm{P}} \to \bar{\mathrm{f}})$ of the corresponding anti-particle ($\bar{\mathrm{P}}$) into the anti-final state ($\bar{\mathrm{f}}$).

We can now deduce conditions for direct *CP*-violation to emerge. We write the total amplitudes as a sum over contributing modes

$$\mathscr{A}_f = \sum_j |a_j| e^{i(\delta_j + \phi_j)}, \tag{2.22}$$

$$\text{and } \bar{\mathscr{A}_{\bar{f}}} = \sum_j |a_j| e^{i(\delta_j - \phi_j)} \tag{2.23}$$

where $|a_j|$ are the magnitudes of the different contributing modes and δ_j and ϕ_j are their corresponding strong and weak phases. The weak phase originates from the phase of the

CKM-matrix and flips sign under *CP*-transformation. The strong phase originates from strong force effects, like rescattering of intermediate states, which are in principle always present. The strong force is invariant under *CP*-transformation, i.e. the strong phase does not flip sign. The observable difference in the intensity is then

$$\begin{aligned}
|\mathscr{A}_f|^2 - |\bar{\mathscr{A}_{\bar{f}}}|^2 &= \mathscr{A}_f \cdot \mathscr{A}_f^* - \bar{\mathscr{A}_{\bar{f}}} \cdot \bar{\mathscr{A}_{\bar{f}}^*} \\
&= \sum_{j,k} |a_j||a_k| e^{i(\delta_j+\phi_j)} e^{-i(\delta_k+\phi_k)} - \sum_{j,k} |a_j||a_k| e^{i(\delta_j-\phi_j)} e^{-i(\delta_k-\phi_k)} \\
&= \sum_{j,k} |a_j||a_k| [e^{i(\delta_j+\phi_j)} e^{-i(\delta_k+\phi_k)} - e^{i(\delta_j-\phi_j)} e^{-i(\delta_k-\phi_k)}] \\
&= \sum_{j,k} |a_j||a_k| [e^{i(\delta_j-\delta_k)} e^{i(\phi_j-\phi_k)} - e^{i(\delta_j-\delta_k)} e^{i(-\phi_j+\phi_k)}] \\
&= \sum_{j,k} |a_j||a_k| e^{i(\delta_j-\delta_k)} [e^{i(\phi_j-\phi_k)} - e^{i(-\phi_j+\phi_k)}] \\
&= \sum_{j,k} |a_j||a_k| [\cos(\delta_j-\delta_k) + i\sin(\delta_j-\delta_k)][2i\sin(\phi_j-\phi_k)] \\
&= \sum_{j,k} |a_j||a_k| [2i\cos(\delta_j-\delta_k)\sin(\phi_j-\phi_k) - 2\sin(\delta_j-\delta_k)\sin(\phi_j-\phi_k)] \\
&= -2\sum_{j,k} |a_j||a_k| \sin(\delta_j-\delta_k)\sin(\phi_j-\phi_k).
\end{aligned} \tag{2.24}$$

A non-zero difference (i.e. direct *CP*-violation) hence requires at least two contributing amplitudes with distinct weak and strong phases. In practice, we typically measure a *CP*-asymmetry, defined as

$$\mathcal{A}^{CP} = \frac{\Gamma(\bar{\mathrm{P}} \to \bar{\mathrm{f}}) - \Gamma(\mathrm{P} \to \mathrm{f})}{\Gamma(\bar{\mathrm{P}} \to \bar{\mathrm{f}}) + \Gamma(\mathrm{P} \to \mathrm{f})}. \tag{2.25}$$

This is the type of *CP*-violation measured in this thesis.

CP-Violation in Mixing

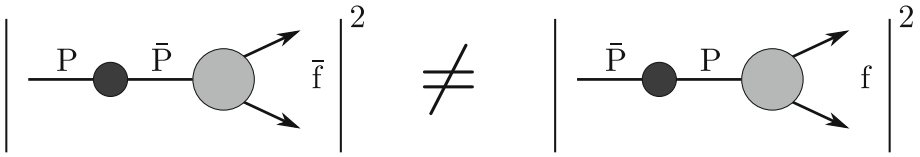

Figure 2.6: *CP*-violation in mixing or indirect *CP*-violation [32].

If the direct decays $\mathrm{P} \nrightarrow \bar{\mathrm{f}}$ and $\bar{\mathrm{P}} \nrightarrow \mathrm{f}$ of a neutral particle P are forbidden, but it can transform into its antiparticle via $\mathrm{P} \rightleftarrows \bar{\mathrm{P}}$ oscillations the processes $\mathrm{P} \to \bar{\mathrm{P}} \to \bar{\mathrm{f}}$ and $\bar{\mathrm{P}} \to \mathrm{P} \to \mathrm{f}$ become allowed. If the oscillation rates $\Gamma(\mathrm{P} \to \bar{\mathrm{P}}) \neq \Gamma(\bar{\mathrm{P}} \to \mathrm{P})$ differ, *CP*-violation in mixing occurs, which is typically very small.

CP-Violation in the Interference between Mixing and Decay

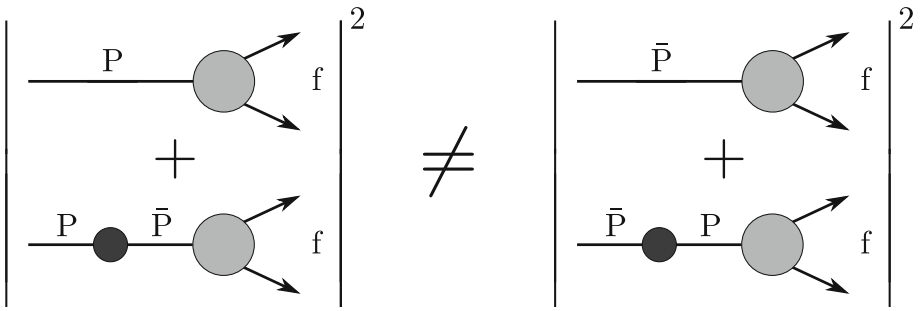

Figure 2.7: *CP*-violation in the interference between mixing and decay or mixing induced *CP*-violation [32].

CP-violation in the interplay between mixing and decay happens when a neutral particle is capable of transforming into its antiparticle, and both can decay into the same final state. The processes $\mathrm{P} \to \mathrm{f}$ and $\mathrm{P} \to \bar{\mathrm{P}} \to \mathrm{f}$ interfere and cause *CP*-violation. Experimentally, it can be measured as the time dependent rate

$$\mathcal{A}^{CP}(t) = \frac{\Gamma(\bar{\mathrm{P}}(t) \to \mathrm{f}) - \Gamma(\mathrm{P}(t) \to \mathrm{f})}{\Gamma(\bar{\mathrm{P}}(t) \to \mathrm{f}) + \Gamma(\mathrm{P}(t) \to \mathrm{f})}. \tag{2.26}$$

The principle of such a measurement is explained in the following.

2.3.6 Discovery of *CP*-violation in B-meson decays

The predicted large *CP*-violation in the B-meson system (see Eq. 2.20) was one of the main motivations for the construction of the so-called B-factories PEP-II with the *BABAR* experiment and KEKB with the Belle experiment. The idea is to produce a large sample of B-meson decays in the clean environment of e^+e^- collisions. To this end, electrons and positrons were collided at an energy matching the $\Upsilon(4S)$ resonance which decays almost always into a pair of B-mesons. The generated pair of neutral B-mesons is in an entangled P-wave and evolves coherently. Just like the neutral kaons, neutral B-mesons propagate with time into a superposition of B^0 ($d\,\bar{b}$) and $\overline{B}^0$ ($\bar{d}\,b$). The responsible Feynman diagrams are shown in Figure 2.8.

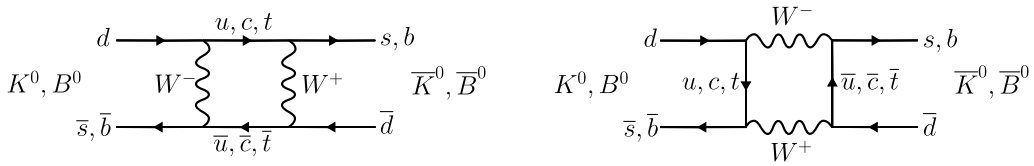

Figure 2.8: Feynman box diagrams for the flavor oscillation of the neutral K-mesons and B-mesons.

Therefore, after some time, both created B-mesons are in superposition of B^0 and $\overline{B}^0$. However, if one of them decays weakly, the wave function collapses and unambiguously determines the flavor of both B-mesons at that time. The difference in the decay time Δt can be used to measure time-dependent CP-violation (see Eq. 2.26). In the B-meson system Δt is of the order of a few pico seconds. However, this decay time difference cannot be measured directly. What we can measure precisely, though, are the decay positions of the B-mesons with a vertex detector and determine their spatial distance Δz. In B-factories the energies of the electron and positron beams are chosen asymmetrically, i.e. generally the e^- beam has higher energy than the e^+ beam, such that in the laboratory frame the produced B-mesons are boosted in the direction of the e^- beam. If they decay at different times they will be spatially separated along the direction of the e^- beam (i.e. the z-direction). From the spatial distance Δz between the vertices, we can then deduce the decay time difference Δt via

$$\Delta t = \frac{\Delta z}{\gamma \beta c} \tag{2.27}$$

where $\gamma = \frac{1}{\sqrt{1-\beta^2}}$ is the relativistic Lorentz factor, $\beta = \frac{v}{c}$ and c is the vacuum speed of light. Simply speaking, the decay time difference is translated into a spatial difference, which can be "easily" and precisely measured.

The golden channel to measure time-dependent CP-violation in the B-mesons system is $B^0 \to J/\psi\,[\mu^-\mu^+] K_S^0 [\pi^+\pi^-]$, due to its comparably simple event reconstruction (only four charged tracks) and relatively large branching fraction, yielding a large data sample with small backgrounds. Furthermore, it is dominated by tree transitions, making it theoretically clean.

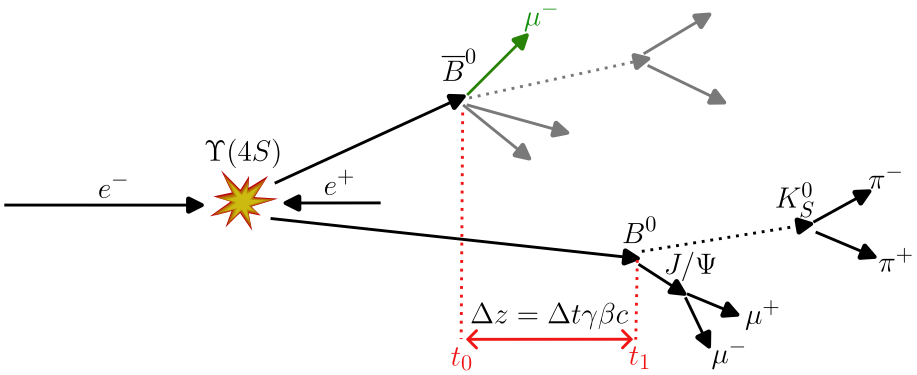

Figure 2.9: Principle of the time-dependent CP-violation measurement in $B \to J/\psi\, K_S^0$.

A sketch of the measurement principle is shown in Figure. 2.9. The $\overline{B}^0$ decay yields a negative muon, which tags the mother particle to be a $\overline{B}^0$. Its decay defines t_0. The B^0 decays into J/ψ and K_S^0 and defines t_1. The spatial difference Δz between the two decay vertices is measured and is related to Δt via Equation 2.27. Through this measurement, *BABAR* [33] and Belle [34] observed the predicted large CP-violation in the decay of

B-mesons, thereby confirming Kobayashi's and Maskawa's theory, which was then honored by the Nobel prize for physics in 2008.

2.4 Charmless Hadronic B-Meson Decays

B-meson decays into hadronic states without any charm-quark are referred to as *charmless hadronic B-meson decays*. In particular these are decays, where the final states are pions (u- and d-quark) and kaons (s- and u-/d-quark) or excited states of those. Hence, the b-quark of the B-meson must transform into an u-, d- or s-quark. The Feynman diagrams of the dominating contributions are shown in Figure 2.10.

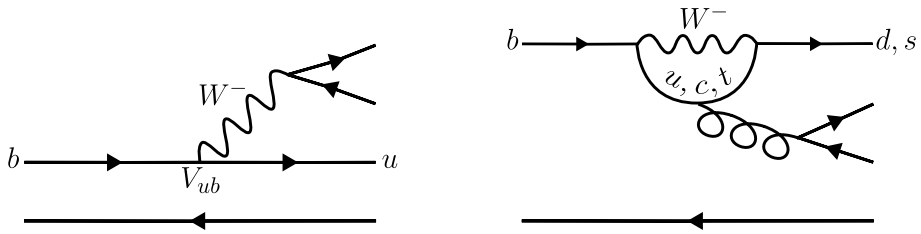

Figure 2.10: Feynman diagram of a $b \to u$ tree transition (left) and a $b \to d, s$ loop transition (right).

The tree diagram (Fig. 2.10 left) goes with strength V_{ub}, which is proportional to $\lambda^3 = 0.22^3$ as can be seen in the Wolfenstein representation of the CKM-martix. This means, that transitions from third to first generation are strongly suppressed, the so called CKM-suppression. Typically, loop diagrams (Fig. 2.10 right) are suppressed relative to tree diagrams, due to their many vertices, each contributing with coupling strengths smaller than one. However, due to the large CKM-suppression in the tree diagram, here the loop diagram is of similar strength. Potential heavy new physics particles can occur as virtual particles in these loops and may contribute significantly to the overall decay. This is one particularity rendering charmless hadronic B-meson decays interesting for the search of physics beyond the Standard Model. The CKM-suppression, however, results in small branching fractions of $\mathcal{O}(10^{-5})$ or less, making these decays experimentally challenging due to comparable large backgrounds.

2.4.1 The $K^{(*)}\pi$ Isospin Sum Rule

Theory predictions for charmless hadronic B-meson decays are limited by the calculations of complex hadronic matrix elements of QCD, making direct predictions of branching fractions or CP-violation parameters rather imprecise. However, internal symmetries, like isospin, can be used to relate different decay modes and cancel theory uncertainties. One such rule is proposed by Gronau [35] for $B^0 \to K^{+(*)}\pi^-$, $B^0 \to K^{0(*)}\pi^0$, $B^+ \to K^{+(*)}\pi^0$ and $B^+ \to K^{0(*)}\pi^+$ decays, which, if violated experimentally, would be evidence for new physics in $b \to sq\bar{q}$ transitions. The deduction and assumptions of the $K^{(*)}\pi$ isospin sum rule will be outlined following [35].

The dominating decay contributions are shown in Figure 2.11. They are

T , the color-favored tree diagram,
C , the color-suppressed tree diagram,
P , the QCD penguin diagram,
P_{EW} , the electro-weak penguin diagram,
P_{EW}^{C} , the color-suppressed electro-weak penguin diagram and
A , the electro-weak annihilation diagram.

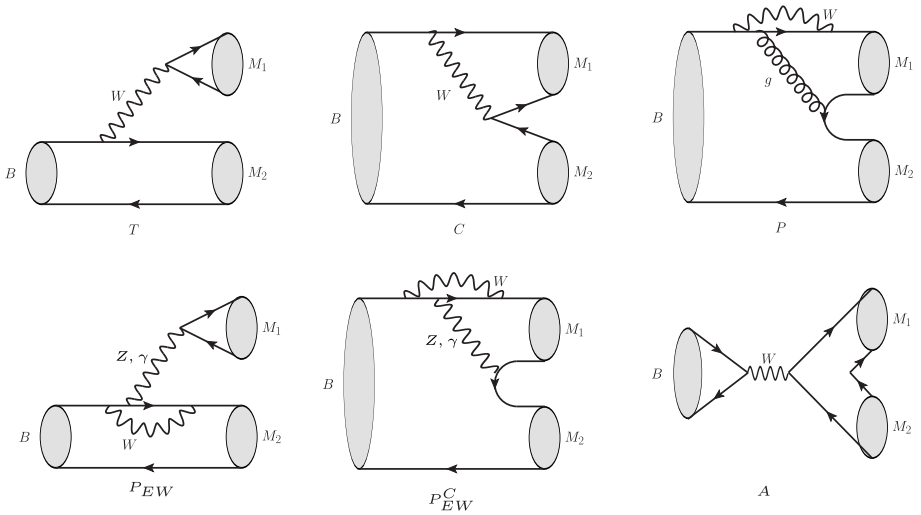

Figure 2.11: Feynman diagrams of the dominating decay modes in $B \to K^{(*)}\pi$[3](adapted by the author). M_1 and M_2 are the final state mesons, i.e. kaons and pions.

The QCD penguin diagram, P, can be expressed as

$$P = V_{ub}^* V_{us} P_u + V_{cb}^* V_{cs} P_c + V_{tb}^* V_{ts} P_t \tag{2.28}$$

i.e. its a sum over the different quarks (u, c and t) that can appear in the loop. We define

$$\begin{aligned} \lambda_u &\equiv V_{ub}^* V_{us} \\ \lambda_c &\equiv V_{cb}^* V_{cs} \\ \lambda_t &\equiv V_{tb}^* V_{ts} \end{aligned} \tag{2.29}$$

and exploit the unitarity condition from Equation 2.17, $\lambda_u + \lambda_c + \lambda_t \stackrel{!}{=} 0$, such that Eq. 2.28 becomes

$$P = \lambda_u P_{uc} + \lambda_t P_{tc} \tag{2.30}$$

with $P_{uc} \equiv P_u - P_c$ and $P_{tc} \equiv P_t - P_c$.

According to [36] and [37] they can be ordered by strength like

$$\begin{aligned} 1 &: |P_{tc}| \\ \mathcal{O}(\lambda) &: |T|\,,\ |P_{EW}| \\ \mathcal{O}(\lambda^2) &: |C|\,,\ |P_{uc}|\,,\ \left|P_{EW}^{C}\right|,\ |A| \end{aligned} \tag{2.31}$$

with $\lambda = 0.22$. (This is not an expansion in λ, but a phenomenological order that goes like λ.)

Depending on the quark content in a decay certain diagrams from above are allowed, while others are not. For example for $B^0 \to K^{+(*)}\pi^-$ T, P and P^C_{EW} are possible, while e.g. the annihilation mode A is not possible, since it would break charge conservation, as the W-boson is charged, while the B^0 is neutral. Considering all possible diagrams the amplitudes $\mathscr{A}$of the four $B \to K^{(*)}\pi$ decays can be written in terms of the corresponding diagram contributions to each decay like

$$-\mathscr{A}(K^{(*)+}\pi^-) = \lambda_u(P_{uc} + T) + \lambda_t(P_{tc} + \frac{2}{3}P^C_{EW}), \tag{2.32}$$

$$-\sqrt{2}\mathscr{A}(K^{(*)+}\pi^0) = \lambda_u(P_{uc} + T + C + A) + \lambda_t(P_{tc} + P_{EW} + \frac{2}{3}P^C_{EW}), \tag{2.33}$$

$$\sqrt{2}\mathscr{A}(K^{(*)0}\pi^0) = \lambda_u(P_{uc} - C) + \lambda_t(P_{tc} - P_{EW} - \frac{1}{3}P^C_{EW}), \tag{2.34}$$

$$\mathscr{A}(K^{(*)0}\pi^+) = \lambda_u(P_{uc} + A) + \lambda_t(P_{tc} - \frac{1}{3}P^C_{EW}). \tag{2.35}$$

Defining the difference in the decay rates as

$$\Delta(B \to f) \equiv \Gamma(\overline{B} \to \overline{f}) - \Gamma(B \to f) \tag{2.36}$$

one gets

$$\Delta(K^{(*)+}\pi^-) = \mathfrak{Im}[(P_{tc} + \frac{2}{3}P^C_{EW})(P_{uc} + T)^*] \cdot 4\mathfrak{Im}(\lambda_t\lambda_u^*), \tag{2.37}$$

$$2\Delta(K^{(*)+}\pi^0) = \mathfrak{Im}[(P_{tc} + P_{EW} + \frac{2}{3}P^C_{EW})(P_{uc} + T + C + A)^*] \cdot 4\mathfrak{Im}(\lambda_t\lambda_u^*), \tag{2.38}$$

$$2\Delta(K^{(*)0}\pi^0) = \mathfrak{Im}[(P_{tc} - P_{EW} - \frac{1}{3}P^C_{EW})(P_{uc} - C)^*] \cdot 4\mathfrak{Im}(\lambda_t\lambda_u^*), \tag{2.39}$$

$$\Delta(K^{(*)0}\pi^+) = \mathfrak{Im}[(P_{tc} - \frac{1}{3}P^C_{EW})(P_{uc} + A)^*] \cdot 4\mathfrak{Im}(\lambda_t\lambda_u^*). \tag{2.40}$$

We can now write down a combination of differences of all decay modes as

$$\begin{aligned}\delta_{K^{(*)}\pi} \equiv \Delta(K^{(*)+}\pi^-) + \Delta(K^{(*)0}\pi^+) - 2\Delta(K^{(*)+}\pi^0) - 2\Delta(K^{(*)0}\pi^0) = \\ = -\mathfrak{Im}[(P_{EW} + P^C_{EW})(T + C)^* + \\ +(P_{EW}C^* - P^C_{EW}T^*) + \\ +(P_{EW} + P^C_{EW})A^*] \cdot 4\mathfrak{Im}(\lambda_t\lambda_u^*)\end{aligned} \quad . \tag{2.41}$$

All dominant P_{tc} terms have vanished. $\delta_{K^{(*)}\pi}$ only contains sub-leading electro-weak contributions. The first two terms are suppressed in the limit of $SU(3)$ and the last term contains an interference between the sub-dominant amplitudes $P_{EW} + P^C_{EW}$ and A such that they are suppressed relative to leading terms like P_{tc} (for details see [35]).Therefore, we can safely assume $\delta_{K^{(*)}\pi} \approx 0$ within a few percent. This condition re-written in terms

of branching fractions $\mathcal{B}$ and direct *CP*-violation $\mathcal{A}^{CP}$ yields the so-called $K^{(*)}\pi$ *isospin sum rule*:

$$\begin{aligned}\mathcal{A}^{CP}(K^{(*)+}\pi^-) + \mathcal{A}^{CP}(K^{(*)0}\pi^+)\frac{\mathcal{B}(K^{(*)0}\pi^+)}{\mathcal{B}(K^{(*)+}\pi^-)}\frac{\tau_0}{\tau_+} \approx \\ \approx \mathcal{A}^{CP}(K^{(*)+}\pi^0)\frac{2\mathcal{B}(K^{(*)+}\pi^0)}{\mathcal{B}(K^{(*)+}\pi^-)}\frac{\tau_0}{\tau_+} + \mathcal{A}^{CP}(K^{(*)0}\pi^0)\frac{2\mathcal{B}(K^{(*)0}\pi^0)}{\mathcal{B}(K^{(*)+}\pi^-)}\end{aligned} \tag{2.42}$$

In literature, typically, all terms are brought to one side and the parameter $I_{K^{(*)}\pi}$ is introduced

$$\begin{aligned}I_{K^{(*)}\pi} = \mathcal{A}^{CP}(K^{(*)+}\pi^-) + \mathcal{A}^{CP}(K^{(*)0}\pi^+)\frac{\mathcal{B}(K^{(*)0}\pi^+)}{\mathcal{B}(K^{(*)+}\pi^-)}\frac{\tau_0}{\tau_+} - \\ - \mathcal{A}^{CP}(K^{(*)+}\pi^0)\frac{2\mathcal{B}(K^{(*)+}\pi^0)}{\mathcal{B}(K^{(*)+}\pi^-)}\frac{\tau_0}{\tau_+} - \mathcal{A}^{CP}(K^{(*)0}\pi^0)\frac{2\mathcal{B}(K^{(*)0}\pi^0)}{\mathcal{B}(K^{(*)+}\pi^-)}\end{aligned} \tag{2.43}$$

Belle II recently measured $I_{K\pi} = -0.03 \pm 0.13\,(\text{stat.}) \pm 0.04\,(\text{sys.})$ to be in agreement with the SM prediction of zero [4]. However, the measurement is dominated by the large statistical uncertainty, such that it remains to be shown whether the rule still holds for larger datasets.

Until now, $I_{K^*\pi}$ has not been measured. Two of the four decays, namely $B^0 \to K^{*+}\pi^-$ and $B^0 \to K^{*0}\pi^0$ contribute to the total amplitude of the $B^0 \to K^+\pi^-\pi^0$ decay, which is measured in this thesis, providing a first step towards a measurement of the $K^*\pi$ rule. The $B^0 \to K^+\pi^-\pi^0$ decay proceeds dominantly via resonances, like $B^0 \to K^{*+}[K^+\pi^0]\pi^-$ or $B^0 \to \rho^-[\pi^-\pi^0]K^+$. Here we introduce the notation of square brackets, meaning the particle in front of the square brackets decays into the particles inside the square brackets. Each of the resonances interferes with each other resonance, such that one cannot simply disentangle the contributions. One must describe the full $B^0 \to K^+\pi^-\pi^0$ amplitude to deduce single contributions, which can be done with a Dalitz plot analysis and is introduced in the following.

3 The Dalitz Plot Analysis Formalism

The goal of this analysis is to understand the contributing amplitudes of the $B^0 \to K^+\pi^-\pi^0$ decay, in particular the ones of the K^* resonances. In general a three-body decay $\mathrm{P} \to \mathrm{f_1 f_2 f_3}$ is described by a five dimensional phase space. We choose two invariant masses squared of the three two-body subsystems, i.e. (m^2_{12}, m^2_{13}) or (m^2_{12}, m^2_{23}) or (m^2_{13}, m^2_{23})[1] and the three Euler angles, describing the orientation of $\mathrm{f_1 f_2 f_3}$ in space. However, since the B-meson has spin zero the decay follows no specific direction and the distributions in the Euler angles is uniform. Hence, three-body dynamics of B-meson decays are fully encoded in two of the invariant mass squared combinations.

The idea of describing a three-body decay in a two-dimensional phase space, was originally developed by R.H. Dalitz for τ to three pion decays [5, 6]. Dalitz however, used the energies of the final state particles, while nowadays it is customary to use a pair of square invariant masses.

The differential decay rate for a particle P decaying to three mesons can be written as

$$\frac{d^2\Gamma}{dm^2_{12}dm^2_{23}} = \frac{m_P}{32(2\pi)^3}|\mathscr{A}(m^2_{12}, m^2_{23})|^2, \tag{3.1}$$

where m_P is the mass of the mother particle and $\mathscr{A}$ is the amplitude. The differential decay rate is only a function of (m^2_{12}, m^2_{23}) (or any other two combinations) [38]. The 2D-distribution of two invariant masses squared is called Dalitz plot. Figure 3.1 shows the kinematically allowed regions in the Dalitz plane for the $B^0 \to K^+\pi^-\pi^0$ decay.

The Dalitz plot variable m^2_{12} is kinematically limited by

$$m^2_{12,\,min} = (m_1 + m_2)^2, \tag{3.2}$$

where the the whole kinematic energy is carried by particle 3 and system 12 being at rest and

$$m^2_{12,\,max} = (m_P - m_3)^2, \tag{3.3}$$

where particle 3 is at rest and all kinematic energy carried away by system (12). For a given m^2_{12}, m^2_{23} is limited by

$$m^2_{23,\,min}(m_{12}) = (E^{12}_2(m_{12}) + E^{12}_3(m_{12}))^2 - (\sqrt{E^{12}_2(m_{12}) - m^2_2} + \sqrt{E^{12}_3(m_{12}) - m^2_3})^2 \text{ and} \tag{3.4}$$

$$m^2_{23,\,max}(m_{12}) = (E^{12}_2(m_{12}) + E^{12}_3(m_{12}))^2 - (\sqrt{E^{12}_2(m_{12}) - m^2_2} - \sqrt{E^{12}_3(m_{12}) - m^2_3})^2 \tag{3.5}$$

[1] The third invariant mass squared can be deduced with $m^2_P + m^2_1 + m^2_2 + m^2_3 = m^2_{12} + m^2_{13} + m^2_{23}$, where m_P, m_1, m_2 and m_3 are the masses of the particles P, $\mathrm{f_1}$, $\mathrm{f_2}$ and $\mathrm{f_3}$

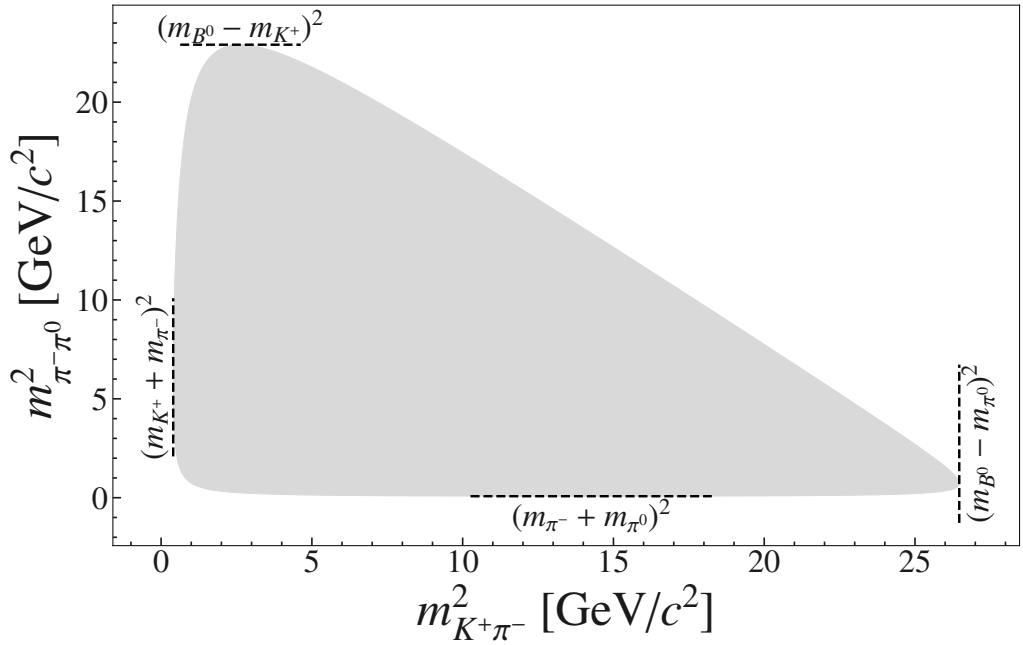

Figure 3.1: Dalitz plane of $B^0 \to K^+\pi^-\pi^0$ decays. The grey-shaded area illustrates the kinematically allowed region, which is constrained by the masses of the involved particles (dashed lines).

where

$$E_2^{12}(m_{12}) = \frac{m_{12}^2 + m_2^2 - m_1^2}{2m_{12}} \text{ and} \tag{3.6}$$

$$E_3^{12}(m_{12}) = \frac{m_P^2 - m_{12}^2 + m_3^2}{2m_{12}} \tag{3.7}$$

are the energies of particle 2 and 3 in the rest-frame of system (12).

3.1 Dalitz Plot Analysis of $B^0 \to K^+\pi^-\pi^0$

The $B^0 \to K^+\pi^-\pi^0$ decay was already analysed by the *BABAR* experiment [8]. Their Dalitz plot is shown in Figure 3.2.

One can see, that the distribution of events is not uniform. Most events cluster in narrow bands at defined two-body masses. This means, that the decay proceeds dominantly via two-body resonances. Therefore, we simplify the problem by modeling it as a sequence of two-body decays $P \to \xi[f_1 f_2] f_3$. I.e. the particle first decays into a resonance or isobar ξ and f_3, and subsequently ξ decays into f_1 and f_2[2]. All possible intermediate isobars contribute to the overall $B^0 \to K^+\pi^-\pi^0$ decay amplitude. Each resonance interferes with each other resonance. Therefore, we coherently sum all considered isobars or resonances, to

[2]Of course, isobars can also live in any other two-body sub-system.

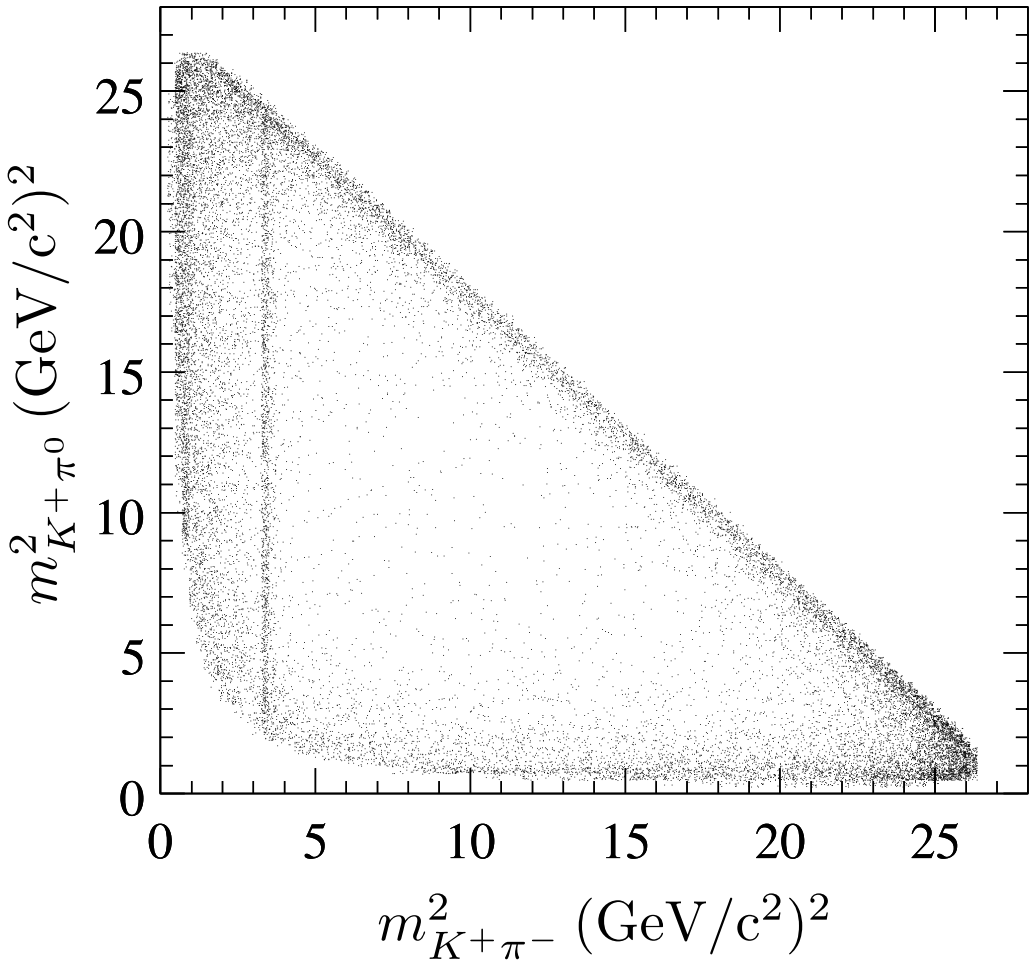

Figure 3.2: Dalitz plot of $B^0 \to K^+\pi^-\pi^0$ decays as measured by the *BABAR* experiment [8].

model the full decay amplitude. This is called the isobar formalism. For our $B^0 \to K^+\pi^-\pi^0$ decay we define the order $m^2_{12} \equiv m^2_{K^+\pi^-}$, $m^2_{13} \equiv m^2_{K^+\pi^0}$ and $m^2_{23} \equiv m^2_{\pi^-\pi^0}$ and we write the amplitude as

$$\mathscr{A}(m^2_{12}, m^2_{23}) = \sum_i c_i \psi_i(m^2_{12}, m^2_{23}) \tag{3.8}$$

where the sum runs over all included resonances described by functions $\psi_i(m^2_{12}, m^2_{23})$. The parameters c_i are complex valued and encode the the magnitude r_i and phase ϕ_i of the resonance. The magnitude describes the "strength" of a resonance and the phase difference between two resonances determines how they interfere (constructively or deconstructively). These are the values we want to measure in this analysis. As we also want to measure direct *CP*-violation we model the *CP*-conjugated $\overline{B}^0 \to K^-\pi^+\pi^0$ decay amplitude as

$$\overline{\mathscr{A}}(m^2_{12}, m^2_{23}) = \sum_i \overline{c}_i \psi_i(m^2_{12}, m^2_{23}). \tag{3.9}$$

The functions $\psi_i(m_{12}^2, m_{23}^2)$ are the same as the ones in Equation 3.8, because they model the underlying strong interactions between the hadrons, which are *CP*-invariant. The parameters c_i and $\bar{c}_i$ encode the weak interactions, i.e. they are *CP*-violating and hence different for $B^0 \to K^+\pi^-\pi^0$ and $\overline{B}^0 \to K^-\pi^+\pi^0$ decays.

We normalize the functions $\psi_i(m_{12}^2, m_{23}^2)$ over the Dalitz plane such that[3]

$$\iint_{DP} \left|\psi_i(m_{12}^2, m_{23}^2)\right|^2 dm_{12}^2 dm_{23}^2 = 1. \tag{3.10}$$

They can be decomposed into four parts [39]

$$\psi_i(m_{12}^2, m_{23}^2) = L_i(m_{12}^2) \times T_i(m_{12}^2, m_{23}^2) \times B_{res,i}(m_{12}^2) \times B_{B^0,i}(m_{12}^2), \tag{3.11}$$

which are discussed in the following.

3.1.1 Angular Dependence

The functions $T(m^2_{K^+\pi^-}, m^2_{\pi^-\pi^0})$ describe the angular dependence of the resonance. We are using the Zemach tensor formalism [40] which evaluates $T(m^2_{K^+\pi^-}, m^2_{\pi^-\pi^0})$ for a spin-J resonance in system (12) as [39]:

$$\begin{aligned}
J = 0: \quad & T(m_{12}^2, m_{23}^2) = 1, \\
J = 1: \quad & T(m_{12}^2, m_{23}^2) = -2\,|\vec{p}|\,|\vec{q}|\cos\theta_{12} = \\
& \qquad = m_{13}^2 - m_{23}^2 - \frac{(m_P^2 - m_3^2)(m_1^2 - m_2^2)}{m_{12}^2}, \\
J = 2: \quad & T(m_{12}^2, m_{23}^2) = \frac{4}{3}\left[3(|\vec{p}|^2\,|\vec{q}|^2\cos^2\theta_{12} - (|\vec{p}|\,|\vec{q}|)^2\right] = \\
& \qquad = \left[m_{23}^2 - m_{13}^2 + \frac{(m_P^2 - m_3^2)(m_1^2 - m_2^2)}{m_{12}^2}\right]^2 - \\
& \qquad - \frac{1}{3}\left[m_{12}^2 - 2m_P^2 - 2m_3^2 + \frac{(m_P^2 - m_3^2)^2}{m_{12}^2}\right] \times \\
& \qquad \times \left[m_{12}^2 - 2m_1^2 - 2m_2^2 + \frac{(m_1^2 - m_2^2)^2}{m_{12}^2}\right]
\end{aligned} \tag{3.12}$$

$\vec{p}$ is the momentum of the bachelor particle, i.e. 3 for a resonance in system (12), and $\vec{q}$ is the momentum of one of the daughters of the resonance called *spin analyzer*, both evaluated in the rest-frame of the resonance. θ_{12} is the angle between $\vec{p}$ and $\vec{q}$.[4] For resonances in

[3] Technically we evaluate the integrals via monte-carlo events generated uniformly in the Dalitz plane ($\{\tau_1, \tau_2, ..., \tau_N\}$, $\tau_k \in DP\ \forall k$), i.e. $\iint_{DP} |\psi_i(\tau)|^2\, d\tau \approx \frac{V}{N}\sum_k^N |\psi_i(\tau_k)|^2$. Than we require that $\frac{1}{N}\sum_k^N |\psi_i(\tau_k)|^2 = 1$, which is missing the phase space volume V. However, this V term can be dropped here without changing the normalization from Eq. 3.10, because in the later constructed likelihood the V term would drop again, as it is common to all waves.

[4] In literature this angle is often called the *helicity* angle θ_H. However the helicity angle is defined as the angle between the momentum of the mother particle and one of the daughters of the resonance, both evaluated in the resonance rest-frame. I.e. $\theta_H = 180° - \theta_{12}$.

$(K^+\ \pi^-)$ we choose the π^- as spin analyzer, for resonances in $(\pi^-\ \pi^0)$ the π^0 is the spin analyzer and for resonances in $(\pi^0\ K^+)$ the K^+ is the spin analyzer. The definition is also illustrated in Figure 3.3.

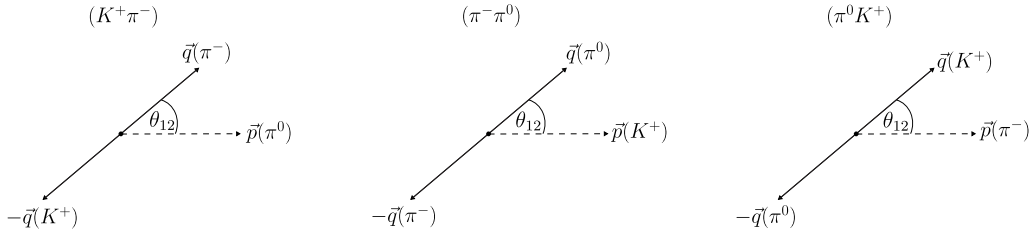

Figure 3.3: Definition of the angle θ_{12} depending on the isobar system.

3.1.2 Angular Momentum Barrier Factors

$B_{res}(m_{12}^2)$ and $B_{B^0}(m_{12}^2)$ are orbital angular momentum compensation factors. In the two-body decay of a spin-J resonance additional energy is needed to create the angular momentum $L = J$ between the decay products to conserve angular momentum. Consequently, for a spin-0 resonance $L = 0$ and $B = 1$. We are using the Blatt-Weisskopf parametrization (Blatt and Weisskopf, 1952) from [39] where resonances in (12) have the following factors:

$$\begin{aligned} J = 0: &\quad B(m_{12}^2) = 1, \\ J = 1: &\quad B(m_{12}^2) = \sqrt{\frac{1 + R^2\left|\vec{q}_0\right|^2}{1 + R^2\left|\vec{q}(m_{12}^2)\right|^2}}, \\ J = 2: &\quad B(m_{12}^2) = \sqrt{\frac{9 + 3R^2\left|\vec{q}_0\right|^2 + R^4\left|\vec{q}_0\right|^4}{9 + 3R^2\left|\vec{q}(m_{12}^2)\right|^2 + R^4\left|\vec{q}(m_{12}^2)\right|^4}}, \end{aligned} \tag{3.13}$$

where R is the meson radius of the resonance. For B_{B^0} we take $\left|\vec{q}(m_{12}^2)\right|$ to be the momentum of the bachelor particle in the resonance rest-frame. For B_{res} $\left|\vec{q}(m_{12}^2)\right|$ is the two-body breakup momentum, which for a decay $P \to a + b$, is given by

$$\left|\vec{q}\right|(m_P^2) = \frac{(m_P^2 - (m_a + m_b)^2)(m_P^2 - (m_a - m_b)^2)}{2m_P} \tag{3.14}$$

$|\vec{q}_0|$ is the momentum where m_{12} is the nominal resonance mass.

3.1.3 Mass dependent Lineshapes

The functions $L(m_{12}^2)$ describe the mass dependence of the resonance in its corresponding sub-system. We are using several different lineshapes for different resonances. Before introducing their parametrization we define m_0 and Γ_0 as the nominal mass and width of the resonance. J is the spin, $\left|\vec{q}(m_{12}^2)\right|$ is the two-body breakup momentum from Equation 3.14 and $|\vec{q}_0|$ is the breakup momentum at the m_0.

Relativistic Breit-Wigner Lineshape

We use the Breit-Wigner lineshape for the $K^*\pi$ isobar resonances. For a resonance in system (12) it is given by

$$L(m_{12}^2) = \frac{m_0\Gamma_0}{m_0^2 - m_{12}^2 - im_0\Gamma(m_{12})}, \tag{3.15}$$

$\Gamma(m_{12}^2)$ is the mass dependent width given by

$$\Gamma(m_{12}^2) = \Gamma_0 \frac{\left|\vec{q}(m_{12}^2)\right|^{2J+1}}{\left|\vec{q}_0\right|^{2J+1}} \frac{m_0}{m_{12}} \frac{B^2(m_{12}^2)}{B^2(m_0^2)} \tag{3.16}$$

with B being the barrier factors from Eq. 3.13. An example of a relativistic Breit-Wigner lineshape for the $K^*(892)^0$ in the $(K^+\pi^-)$ system is show in Figure 3.4 (top).

Gounaris-Sakurai Lineshape

To model the mass dependence of ρ-like resonances more advanced lineshapes are customary. One of such is the Gounaris-Sakurai lineshape [41]. For a resonance in (12) we are using the following parametrization

$$L(m_{12}^2) = \frac{m_0\Gamma_0}{m_0^2 - m_{12}^2 + f - im_{12}\Gamma(m_{12}^2)} \tag{3.17}$$

where $\Gamma(m_{12}^2)$ is the mass dependent width as in Equation 3.16. f is defined as

$$f = \frac{\Gamma_0 m_0^2}{\left|\vec{q}(m_{12}^2)\right|^3} \left[\left|\vec{q}(m_{12}^2)\right|^2 (h - h_0) + \left|\vec{q}_0\right|^2 H(m_0^2 - m_{12}^2) \right] \tag{3.18}$$

with

$$h = \frac{2}{\pi} \frac{\left|\vec{q}(m_{12}^2)\right|}{m_{12}} \log\left(\frac{m_{12} + 2\left|\vec{q}(m_{12}^2)\right|}{m_1 + m_2} \right), \tag{3.19}$$

$$h_0 = h(m_{12} = m_0) \quad \text{and} \tag{3.20}$$

$$H = h_0\left(\frac{1}{8\left|\vec{q}_0\right|^2} - \frac{1}{2m_0}\right) + \frac{1}{2\pi_0^2}. \tag{3.21}$$

The Gounaris-Sakurai lineshape for the $\rho(770)$ resonance in the $(\pi^-\pi^0)$ system is shown in Figure 3.4 (middle).

LASS Lineshape

S-wave resonances in $(K^+\pi^-)$ and $(K^+\pi^0)$ show several "wide" features which cannot be distinguished, since they overlap. Instead of describing them separately we use the so-called LASS lineshape [42] to model them all together. It is basically a resonant Breit-Wigner

contribution plus an effective-range non-resonant contribution. For a resonance in system (12) it is given as [39]

$$L(m_{12}^2) = \frac{m_{12}}{2\,|\vec{q}|}\left[\sin\delta_F e^{i\delta_F} + \sin\delta_R e^{i\delta_R} e^{i2\delta_F}\right], \tag{3.22}$$

with

$$\tan\delta_R = \frac{m_0\Gamma(m_{12}^2)}{m_0^2 - m_{12}^2}, \tag{3.23}$$

$$\cot\delta_F = \frac{1}{a\,|\vec{q}(m_{12}^2)|} + \frac{r\,|\vec{q}(m_{12}^2)|}{2}, \tag{3.24}$$

where a is a scattering length and r is an effective interaction length. The LASS lineshape for the $(K\pi)_0^{*+}$ s-wave is shown in Figure 3.4 (bottom).

3.1.4 The Amplitude Model

In our amplitude model we are including seven intermediate resonances and one non-resonant component, which are summarized in Table 3.1. This model was chosen in the *BABAR* analysis from 2011 [8] providing the current best measurement.

Table 3.1: Line shape parameters of our amplitude model. The LASS parameters are taken from [43]. All other parameters are taken from [15].

Resonance	Lineshape	Parameters
	Spin $J = 1$	
$\rho(770)^-$	GS	$m_0 = 775.26 \pm 0.23\,\mathrm{MeV}/c^2$
		$\Gamma_0 = 147.4 \pm 0.8\,\mathrm{MeV}$
$\rho(1450)^-$	GS	$m_0 = 1465 \pm 25\,\mathrm{MeV}/c^2$
		$\Gamma_0 = 400 \pm 60\,\mathrm{MeV}$
$\rho(1700)^-$	GS	$m_0 = 1720 \pm 20\,\mathrm{MeV}/c^2$
		$\Gamma_0 = 250 \pm 100\,\mathrm{MeV}$
$K^*(892)^+$	RBW	$m_0 = 891.67 \pm 0.26\,\mathrm{MeV}/c^2$
		$\Gamma_0 = 51.4 \pm 0.8\,\mathrm{MeV}$
		$R = 3.0 \pm 0.5(\,\mathrm{GeV})^{-1}$
$K^*(892)^0$	RBW	$m_0 = 895.55 \pm 0.20\,\mathrm{MeV}/c^2$
		$\Gamma_0 = 47.3 \pm 0.5\,\mathrm{MeV}$
		$R = 3.0 \pm 0.5(\,\mathrm{GeV})^{-1}$
	Spin $J = 0$	
$(K\pi)_0^{*+}$, $(K\pi)_0^{*0}$	LASS	$m_0 = 1435 \pm 5\,\mathrm{MeV}/c^2$
		$\Gamma_0 = 279 \pm 6\,\mathrm{MeV}$
		$a = 1.95 \pm 0.09(\,\mathrm{GeV}/c)^{-1}$
		$r = 1.76 \pm 0.36(\,\mathrm{GeV}/c)^{-1}$
non-resonant	Constant	

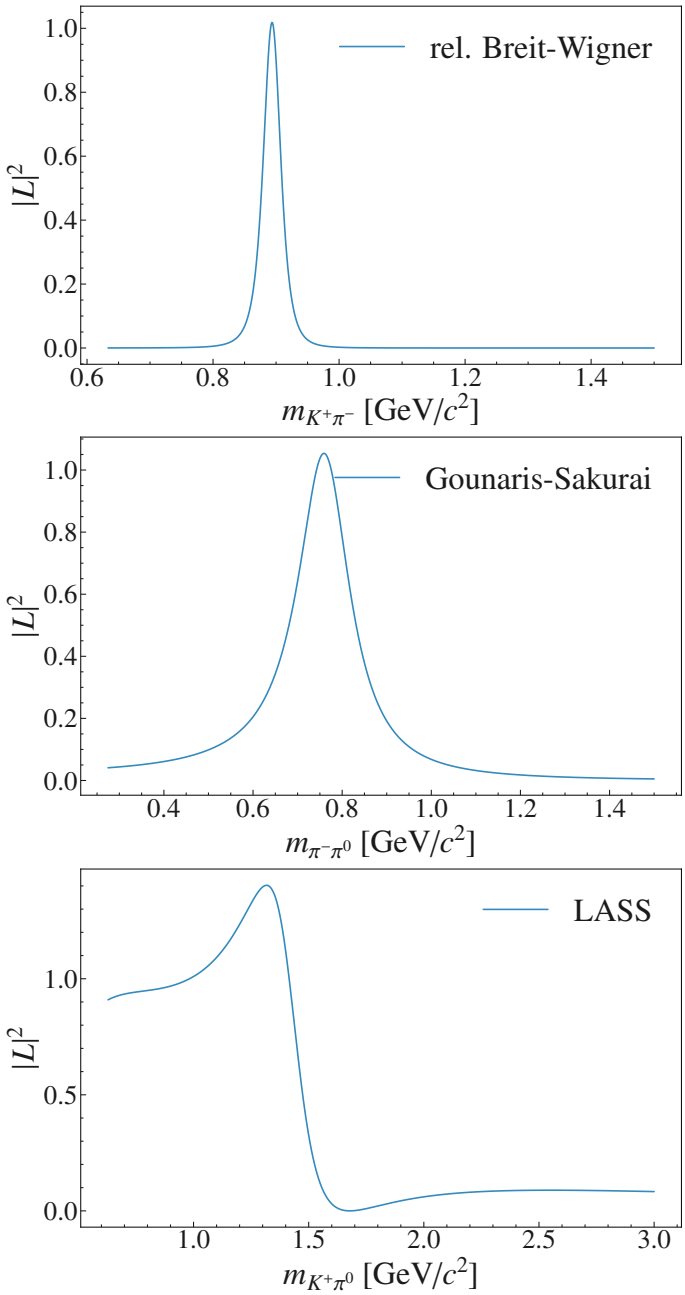

Figure 3.4: Plots of relativistic Breit-Wigner lineshape for the $K^*(892)^0$ resonance (top), Gounaris-Sakurai lineshape for the $\rho(770)^-$ resonance (middle) and LASS lineshape for the $(K\pi)_0^{*+}$ resonance (bottom).

All complex couplings c_i can be scaled by an arbitrary number as well as rotated by an arbitrary phase without changing the overall physics. In order to remove the scaling and phase ambiguity, one typically fixes the magnitude and phase of one resonance to 1 and 0,

respectively. All other resonances are then measured with respect to that wave. In this analysis we are fixing the $\rho(770)^+K^-$, i.e. $c_{\rho(770)^+} = 1e^{i0}$. Since the $B^0 \to K^+\pi^-\pi^0$ and $\overline{B}^0 \to K^-\pi^+\pi^0$ decay do not interfere, also the phase of the $\rho(770)^-$ resonance is fixed to zero, while its magnitude $r_{\rho(770)^-}$ is allowed to float, i.e. $c_{\rho(770)^-} = r_{\rho(770)^-}e^{i0}$, such that one can still measure direct $\mathcal{A}^{CP}$.

3.2 Fit Fractions, Branching Fractions and direct *CP*-Violation of the Resonances

The physics parameters we want to measure are mainly the $B \to \xi f_3$ branching fractions and direct *CP*-violation parameters $\mathcal{A}^{CP}$. Especially those of the $B^0 \to K^*\pi$ decays in order to measure the $K^*\pi$ isospin sum rule (see Eq. 2.42). For this we define the branching fraction of a resonance i as

$$\mathcal{B}_i = FF_i \times \frac{N_{sig}}{N_{B\overline{B}} \cdot \overline{\eta}} = FF_i \times \mathcal{B}_{\text{inclusive}}, \tag{3.25}$$

where N_{sig} and $N_{B\overline{B}}$ are the number of measured $B^0 \to K^+\pi^-\pi^0$ plus $\overline{B}^0 \to K^-\pi^+\pi^0$ decays and the total number of B decays, respectively. $\overline{\eta}$ is the efficiency/acceptance averaged over the Dalitz plot, which is given by

$$\overline{\eta} = \frac{\left|\sum_i (c_i + \overline{c}_i) \iint_{DP} \eta(m_{12}^2, m_{23}^2)\psi_i(m_{12}^2, m_{23}^2)\ dm_{12}^2 dm_{23}^2\right|}{\left|\sum_i (c_i + \overline{c}_i) \iint_{DP} \psi_i(m_{12}^2, m_{23}^2)\ dm_{12}^2 dm_{23}^2\right|} \tag{3.26}$$

with $\eta(m_{12}^2, m_{23}^2)$ being the Dalitz plot dependent efficiency/acceptance, which will be explained in 6.1.1. FF_i are the so-called *Fit-Fractions* given by

$$\begin{aligned} FF_i =& \frac{\iint_{DP} \left(\left|\overline{c}_i\overline{\psi}_i(m_{12}^2, m_{23}^2)\right|^2 + \left|c_i\psi_i(m_{12}^2, m_{23}^2)\right|^2\right)\ dm_{12}^2 dm_{23}^2}{\iint_{DP} \left(\left|\sum_k \overline{c}_k\overline{\psi}_k(m_{12}^2, m_{23}^2)\right|^2 + \left|\sum_k c_k\psi_k(m_{12}^2, m_{23}^2)\right|^2\right)\ dm_{12}^2 dm_{23}^2} = \\ \overset{(3.10)}{=}& \frac{\left|\overline{c}_i\right|^2 + \left|c_i\right|^2}{\iint_{DP} \left(\left|\sum_k \overline{c}_k\overline{\psi}_k(m_{12}^2, m_{23}^2)\right|^2 + \left|\sum_k c_k\psi_k(m_{12}^2, m_{23}^2)\right|^2\right)\ dm_{12}^2 dm_{23}^2}. \end{aligned} \tag{3.27}$$

Note, that the Fit-Fractions do not necessarily add up to one. A value above (below) one expresses constructive (destructive) interference.

The inclusive direct *CP*-violation is given by

$$\mathcal{A}^{CP}_{\text{inclusive}} = \frac{\iint_{DP} \left(\left|\overline{\mathscr{A}}(m_{12}^2, m_{23}^2)\right|^2 - \left|\mathscr{A}(m_{12}^2, m_{23}^2)\right|^2\right)\ dm_{12}^2 dm_{23}^2}{\iint_{DP} \left(\left|\overline{\mathscr{A}}(m_{12}^2, m_{23}^2)\right|^2 + \left|\mathscr{A}(m_{12}^2, m_{23}^2)\right|^2\right)\ dm_{12}^2 dm_{23}^2}, \tag{3.28}$$

and the direct *CP*-violation for a resonance is expressed by

$$\mathcal{A}^{CP}_i = \frac{\left|\overline{c}_i\right|^2 - \left|c_i\right|^2}{\left|\overline{c}_i\right|^2 + \left|c_i\right|^2}. \tag{3.29}$$

3.3 The Square Dalitz Plot

One peculiarity of the Dalitz plot in B-meson decays to light mesons is, that it is mainly populated at its edges, due to the resonances being much lighter than the B-meson. Since we want to use histograms to model our background components and the Dalitz plot dependent efficiency the "standard" Dalitz plot becomes cumbersome. One would need a very granular binning at the edges, where all the events lie. Additionally, the Dalitz plot populates this "triangular'ish" shape with round edges, such that simple rectangular bins cannot be used. To circumvent these problems we perform a coordinate transformation to the so-called *Square Dalitz plot* [44] which spreads out the events. The Square Dalitz plot is defined by the variables

$$m' \equiv \frac{1}{\pi} \cos^{-1}\left(2\frac{m_{12} - m_{12}^{min}}{m_{12}^{max} - m_{12}^{min}} - 1\right) \quad \text{and} \tag{3.30}$$

$$\theta' \equiv \frac{\theta_{12}}{\pi}. \tag{3.31}$$

where $m_{12}^{min} = m_1 + m_2$ and $m_{12}^{max} = m_P - m_3$ are the minimally and maximally allowed m_{12} values in a $\mathrm{P} \to \mathrm{f_1 f_2 f_3}$ decay. θ_{12} is the angle as defined in Fig. 3.3.[5] m' and θ' can take values between zero and one, defining the name "Square Dalitz" plot. The effect of the transformation is shown in Figure 3.5b. The events that were formerly clustered very tightly, are now spread out and occupy a larger region.

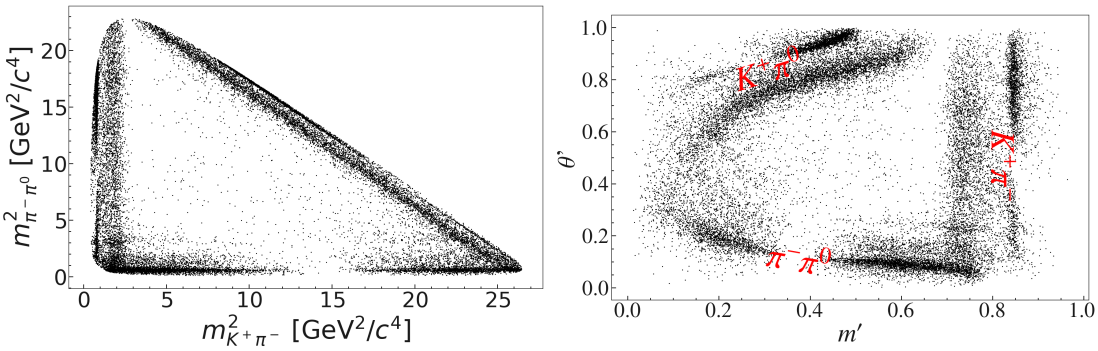

(a) "Standard" Dalitz plot.

(b) Square Dalitz plot.

Figure 3.5: Transformation from the "standard" Dalitz plot to the square Dalitz plot. The red labels indicate the region of resonances in that sub-system.

In order to ensure correct normalizations, in integrals of functions $F(m_{12}^2, m_{23}^2)$ over the Square Dalitz plot, one must include the determinant of the Jacobian of the transformation

$$\iint_{DP} F(m_{12}^2, m_{23}^2)\, dm_{12}^2 dm_{23}^2 = \iint_{SDP} |J(m', \theta')|\, F(m', \theta')\, dm' d\theta'. \tag{3.32}$$

[5] Taking subsystem (12) is an explicit choice. The transformation could also be done in system (13) or (23).

The determinant of the Jacobian is given by

$$\left|J(m', \theta')\right| = 4\,|\vec{p}|\,|\vec{q}|\,m_{12}\frac{\partial m_{12}}{\partial m'}\frac{\partial \cos\theta_{12}}{\partial \theta'} \tag{3.33}$$

with $|\vec{p}|$ and $|\vec{q}|$ defining the angle θ_{12}. The partial derivatives are

$$\frac{\partial m_{12}}{\partial m'} = -\frac{\pi}{2}\sin(\pi m')(m_{12}^{max} - m_{12}^{min}) \quad \text{and} \tag{3.34}$$

$$\frac{\partial \cos\theta_{12}}{\partial \theta'} = -\pi\sin(\pi\theta'). \tag{3.35}$$

4 The Belle II Experiment

The Belle II experiment, situated at the SuperKEKB electron-positron collider in Tsukuba, Japan, is the successor of the Belle experiment. It aims to explore the frontiers of the Standard Model with unprecedented precision. Belle II is designed to study charge-parity (CP) violation in the B-meson system, which was for the first time measured in the Belle and *BABAR* experiments, confirming Cabibbo's, Kobayashi's and Maskawa's theory of the Standard Model. While Belle and *BABAR* verified the the CKM theory, Belle II targets precision measurements of its parameters to potentially find significant differences between theory and measurements which indicate new physics. Such endeavors are pursued in measurements of all CKM angles trying to over-constrain the CKM triangle. Furthermore, the clean environment of e^+e^- collisions allows for studies of decays including one or several neutrinos. In addition to studies of the B-meson, at Belle II, τ lepton decay analysis and searches for dark matter candidates are performed. The $B^0 \to K^+\pi^-\pi^0$ decay studied in this thesis is a so-called rare charmless B-meson decay, i.e. a decay with a branching fraction of $\mathcal{O}(10^{-6})$. In such rare decays new physics might reveal itself in loop contributions. To reach high measurement precision Belle II aims to collect a B-meson dataset of $50\,\text{ab}^{-1}$, i.e. almost two orders of magnitude larger than the Belle dataset within the next decade. The B-mesons are produced by the SuperKEKB accelerator. It collides electrons and positrons at a center-of-mass energy of 10.58 GeV corresponding to the $\Upsilon(4S)$ resonance (third radial excitation of $b\bar{b}$ state). The $\Upsilon(4S)$ decays almost exclusively into a pair of B-mesons, i.e. B^+ ($u\ \bar{b}$) and B^- ($\bar{u}\ b$) or B^0 ($d\ \bar{b}$) and $\overline{B}^0$ ($\bar{d}\ b$). An example of such an event can be seen in Figure 4.1. One of the produced B-mesons decays into our signal decay $B^0 \to K^+\pi^-\pi^0$ and is referred to as signal B-meson. The other B-meson is called tag B-meson and can decay in any possible way.

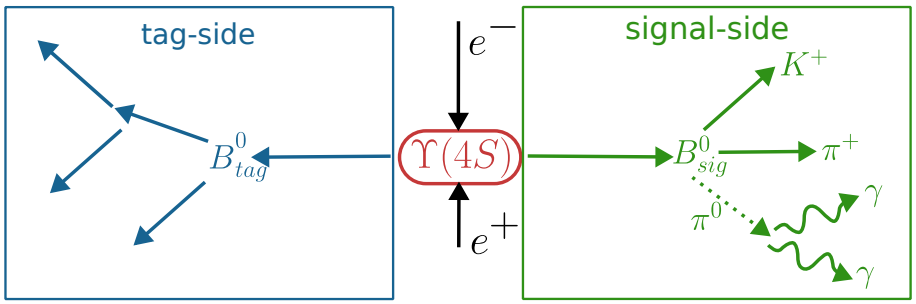

Figure 4.1: Schematic view of an e^+e^- collision creating an $\Upsilon(4S)$ resonance, which decays into two B-mesons. One of them decays via the signal decay $B^0 \to K^+\pi^-\pi^0$, hence called signal side. The other B-meson can decay in any possible way and is called tag B.

This chapter covers the accelerator and collider SuperKEKB with its new nanobeam scheme to achieve world record luminosities (i.e. collisions per time and area) and hence produce a large dataset of B-mesons. The second part briefly describes the setup of the Belle II detector and its sub-detectors. The informations are mainly taken from the "Belle II Technical Design Report" [45], which provides a detailed description of the experimental setup.

4.1 SuperKEKB Accelerator

The SuperKEKB accelerator is an energy asymmetric e^+e^- collider with a target luminosity of $6 \times 10^{35}\,\mathrm{cm}^{-2}\,\mathrm{s}^{-1}$ which is about 30 times higher than its predecessor KEKB [46]. It consists of a linear accelerator (linac) and two storage rings, one for the electrons, high-energy ring (HER), and one for the positrons, low-energy ring (LER), of a circumference of 3 km. An illustration of the SuperKEKB accelerator is shown in Figure 4.2. The electrons are produced in a pre-injector via a photocatode RF gun, accelerated to 7 GeV in the linac and injected into the HER. A second pre-injector provides electrons to irradiate a tungsten target in the middle of the linac to produce the positrons. In a damping ring the energy spread as well as the emittance (area occupied by the beam) of the positrons are lowered. In the second half of the linac they are then accelerated to 4 GeV before injection into the LER. The electrons and positrons are injected in their respective rings in small bunches, i.e. "packages" of particles. In total more than 2000 bunches circulate through each ring [45]. Both rings intersect at one point, where the electron and positron bunches cross and collide, called the interaction point (IP), around which the Belle II detector is constructed.

One important parameter which characterizes the performance of a particle collider is the luminosity $\mathcal{L}$, which describes the amount of collisions per time and area. The number of events per time for a given process is then

$$\frac{dN}{dt} = \mathcal{L} \cdot \sigma, \tag{4.1}$$

where σ is the cross-section of that process. The luminosity has the following proportionality

$$\mathcal{L} \propto \frac{I_\pm}{\beta_y^*}, \tag{4.2}$$

with $I_\pm$ being the positron/electron beam currents and β_y^* the vertical beta function at the interaction point. β_y^* describes the size of the beam bunches in the vertical plane. A simple way of increasing the luminosity is a rise in beam currents, however this renders the bunches more instable due to intra-beam interactions (i.e. stronger electromagnetic repulsion). For SuperKEKB the beam currents are doubled compared to KEKB yielding a factor two in luminosity. The revolutionary increase in luminosity is achieved by implementing the so-called nano beam scheme proposed by P. Raimondi [48]. The basic idea is to squeeze the particle bunches at the interaction point to nano meter scale. Compared to KEKB, SuperKEKB is designed to decrease β_y^* by a factor of 20. With the doubling of the beam currents the luminosity will be increased by a factor of 40[1]. Currently, SuperKEKB sets

[1] Due to technical challenges the current goal, as of spring 2024, is to achieve a factor of 30.

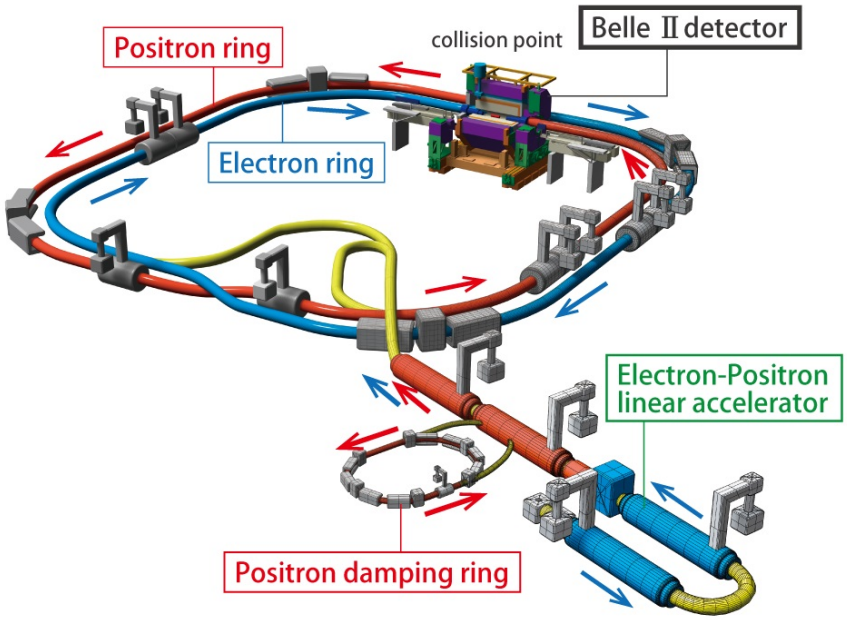

Figure 4.2: Illustration of the SuperKEKB accelerator [47]. Electrons (blue) and positrons (red) are produced and accelerated in the linear accelerator. Afterwards they are injected into storage rings with one collision point which is encapsulated by the Belle II detector.

the world record instantaneous luminosity at $4.71 \times 10^{34}\,\mathrm{cm}^{-2}\,\mathrm{s}^{-1}$ [46]. To cope with the high luminosity delivered by the SuperKEKB collider the Belle II detector is a heavily upgraded version of Belle.

4.2 Belle II Detector

Broken down, a particle spectrometer, such as Belle II, at collider experiments has to fulfill three purposes:

- reconstruct the momenta and origins (vertices) of particles,
- reconstruct the energies of particles and
- identify the particle species.

The Belle II detector is an almost 4π particle spectrometer consisting of several sub-detectors, each measuring one or more of the aforementioned properties. An illustration of Belle II and its sub-detectors is shown in Figure 4.3. It is build cylindrically around the interaction point (IP). Its innermost systems are so-called trackers, which reconstruct the trajectories of charged particles and allow for the precise extraction of their origins (verticies) and momenta. The trackers are surrounded by a precise calorimeter and particle ID detectors for the determination of the particles energies and species. The overall shape

of Belle II is a cylinder. We define the central region as barrel region. The left and right side are called backward and forward endcaps.

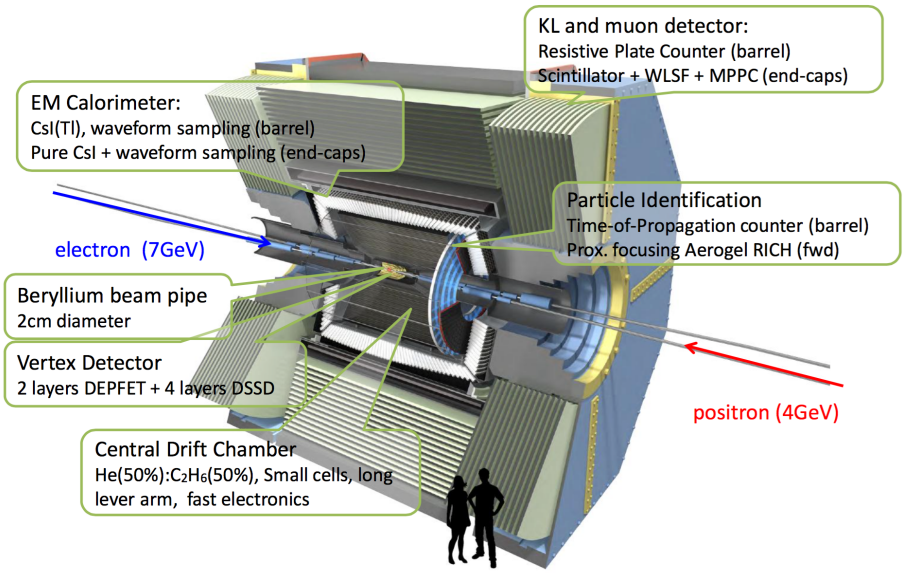

Figure 4.3: The Belle II detector and its sub-systems [49].

The following will explain the sub-detectors and their working principles from the innermost to the outermost system. The descriptions are mainly based on the Belle II technical design report [45], which explains Belle II and its sub-detectors in detail.

4.2.1 Vertex Detector

The innermost detector is the Vertex Detector (VXD) sitting directly on the beam pipe. Its purpose is to precisely determine the origins (vertices) of the final state particles. The VXD itself consists out of two sub-detectors. Two layers of DEpleted P-channel Field Effect Transistor (DEPFET) pixels in the Pixel Vertex Detector (PXD) and four layers of double-sided silicon-strip detectors in the Silicon Vertex Detector (SVD).

Pixel Vertex Detector

The PXD is one of the main upgrades of Belle II. Given the design goal of a 40 times higher instantaneous luminosity and hence increased beam backgrounds a strip-only vertex detector as in Belle would have too high occupancy[2]. This would lead to ambiguities in the reconstruction of verticies (i.e. multiple particles can pass the same strips, such that they cannot be distinguished). Making the sensors more granular by using pixels instead of strips resolves this issue. Further requirements to the detector are radiation hardness as

[2]The occupancy is the percentage of active detector elements (e.g. strips or pixels) at the same time.

well as a small material budget to reduce the effect of multiple scattering for particle with low momenta, which deteriorates the resolution.

The pixels of the PXD are based on DEPFET technology. The cross section of one pixel is shown in Fig. 4.4.

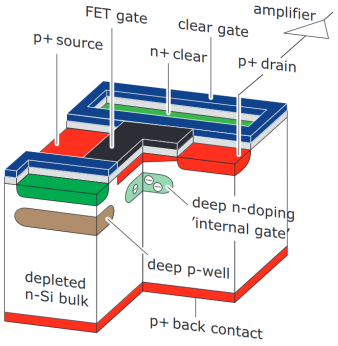

Figure 4.4: Cross section of a DEPFET pixel [45].

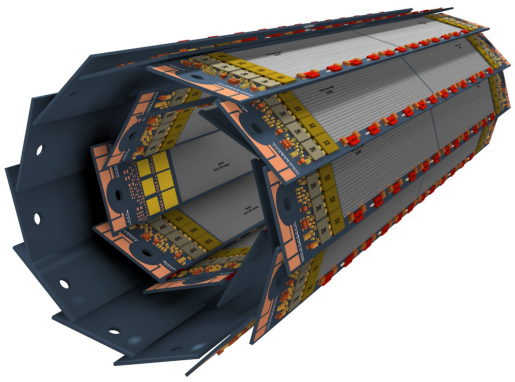

Figure 4.5: Layout of the PXD [49].

A p-channel MOSFET is placed on top of a fully depleted silicon bulk. Charged particles passing the silicon bulk create electron-hole pairs. The holes drift to the p^+ back contact and the electrons are accumulated in an 'internal gate'. These electrons modulate the transistor current which serves as the signal (for details see [45]). Such DEPFET pixels can be made as thin as 50 µm to minimize the impact of multiple scattering.

In total, the PXD contains 7 680 000 pixels distributed over 20 ladders arranged in two layers (see Fig. 4.5). The two layers are cylindrically arranged in a windmill structure around the beam-pipe at radii of 14 mm and 22 mm [45]. During the recording of the dataset, analyzed in this thesis, only the inner layer and two ladders of the outer layer of the PXD were installed. In a shutdown in 2023, the PXD was replaced with a new fully equipped detector.

Silicon Vertex Detector

The SVD makes up the outer four layers of the VXD reaching from 38 mm to 140 mm using double-sided silicon-strip detectors. Its purpose is to extrapolate Central Drift Chamber (CDC) tracks to the PXD as well as to reconstruct low transversal momentum tracks which do not reach the CDC (e.g. D^* daughters) [45].

4.2.2 Central Drift Chamber

The main tracking detector is the CDC, which is a cylindrical chamber filled with a 50% helium and 50% ethan gas mixture. It is permeated by 14336 sense and 42240 field wires between which a high voltage is applied. A charged particle traversing the gas creates free electrons which drift towards the sense wires, where they are detected. These wires are arranged in nine superlayers which alternate in their orientation relative to the beam-axis.

Wires in an axial layer are parallel to the beamline and wires in a stereo layer are slightly skewed with respect to the beamline. This setup allows for a 3D track reconstruction. In order to measure the momenta of charged particles, Belle II contains a superconducting magnet providing a 1.5 T magnetic field. A charged particle passing the field moves on a helical trajectory due to Lorentz force. The radius of the helical path is then proportional to the particles momentum. On its path through the CDC it leaves hits in the different layers. An algorithm connects the hits, belonging to one track and fits its trajectory which determines the particles three momentum and its vertex. Additionally, the CDC provides particle identification information using the energy loss per distance (dE/dx) in the gas mixture. Finally, it provides the trigger signal for charged particles, i.e. decides whether an event should be recorded or not [45].

4.2.3 Time-Of-Propagation Counters

The tracking detectors are surrounded by the particle identification (PID) detectors. Time-Of-Propagation (TOP) is the PID system in the barrel region. It consists of 16 quartz bars arranged around the CDC (see Fig.4.6). Charged particles passing the bars create Cherenkov photons. The opening angle (θ_C) of the Cherenkov light cone depends on the velocity of the particle. With the momentum determined in the tracking systems, the velocity allows for the deduction of the particles mass, which identifies it. The Cherenkov photons travel the quartz bars via total reflection until they reach photo-multiplier tubes (PMTs) at one end of the bars. Different Cherenkov angles result in different propagation times of the photons in the bar. Since the time of the e^+e^- collision is precisely known, the propagation time is known, from a measurement of the time of the PMT signal, and can be used to deduce the Cherenkov angle.

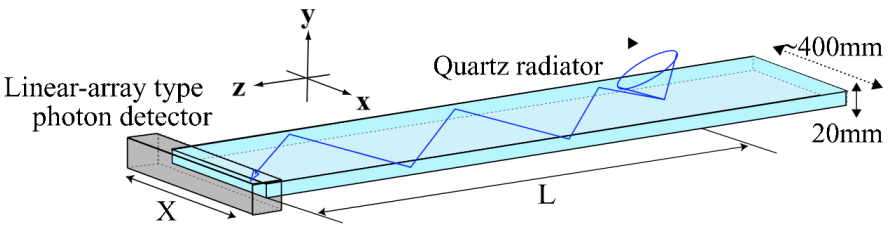

Figure 4.6: Illustration of one TOP quartz counter [45].

The working principle of a TOP counter is shown in Fig. 4.7. Given the Cherenkov photons of kaons and pions have different Cherenkov angles, the propagation time in the quartz bar is different and allows for their discrimination [45].

4.2.4 Aerogel Ring-Imaging Cherenkov Detector

The Aerogel Ring-Imaging CHerenkov (ARICH) detector is the PID system in the forward endcap. Its purpose is kaon pion separation as well as discrimination of low momentum pions, muons and electrons. The ARICH consists of two layers of silica aerogel. Charged

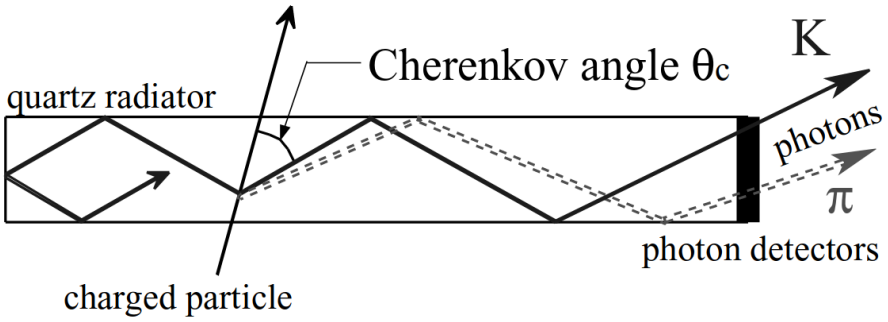

Figure 4.7: Working principle of the TOP counters. Different particle types create Cherenkov photons with different Cherenkov angles allowing for PID [45].

particles radiate Cherenkov photons while traversing them. After propagation through a 20 cm expansion volume to allow the formation of rings they are detected by an array of Hybrid Avalanche Photo-Detectors (HAPDs). The radius of the ring determines the Cherenkov angle. The photo detectors can detect single photons with high efficiency and spatial resolution [45].

4.2.5 Electromagnetic Calorimeter

Photons are reconstructed in the Electromagnetic CaLorimeter (ECL) which encloses TOP and ARICH. It consists of 6624 CsI(Tl) crystals in the barrel region and 2112 CsI crystals in the two endcaps. Electrons and photons deposit their energy in electromagnetic showers via Bremsstrahlung and pair production. Scintillation light is created and read out with photodiodes. In order to achieve high resolution the ECL is required to detect photons with high efficiency and precisely determine their energy and position over a large kinematic range. Furthermore, it provides information for electron identification and trigger signals [45].

4.2.6 K_L^0 and μ Detector

The outermost sub-detector is the K_L^0 and μ detector (KLM). It consists of alternating iron plates and and active detector elements. The iron plates serve as a dense interaction material for muons and K_L^0 mesons. While muons create electromagnetic showers, K_L^0 mesons interact hadronically (i.e. strong), creating a distinct shower shape. As active detector elements, Belle only used glass electrode resistive plate chambers (RPCs), but they become inefficient at the expected background rates of Belle II. Hence, scintillators with silicon photomultipliers (SiPMs) are used in the endcaps as well as in the first two layers of the barrel region. RPCs consist of two parallel sheets of float glass, serving as electrodes, which are separated by a small gas volume. Charged particles, originating from the electromagnetic or hadronic showers, ionize the gas mixture. The freed electrons and ions are accelerated towards one of the glass electrodes, where the current is read out by read out strips. As muons are charged particles, they also created a track in the CDC.

CDC tracks are extrapolated to the KLM, where they can be associated with a muon shower [45, 50].

4.2.7 Trigger

e^+e^- collisions at the $\Upsilon(4S)$ resonance can result in a variety of physics processes, which are summarized in Table 4.1. Recording all those events would result in huge data rates and data storage requirements. As the Belle II physics program mainly concerns B-meson (and τ) decays an online decision logic, called trigger, is employed to only record the events of interest. It must achieve a high efficiency for those events with a limited maximum trigger rate of 30 kHz at Belle II. The trigger logic combines informations from the CDC, ECL, TOP and KLM to decide whether an event should be stored or not. E.g. a $\Upsilon(4S)$ event is recorded if there are more than two tracks in the CDC and more than three isolated clusters with an energy deposit larger than 1 GeV in the ECL [45].

Table 4.1: List of physics processes in e^+e^- collisions at the $\Upsilon(4S)$ resonance for the original SuperKEKB design luminosity of $L = 8 \times 10^{35}\,\mathrm{cm}^{-2}\,\mathrm{s}^{-1}$ [45].

Physics process	Cross section [nb]	Rate [Hz]
$e^+e^- \to \Upsilon(4S) \to B\overline{B}$	1.2	960
$e^+e^- \to u\overline{u}$, $d\overline{d}$, $c\overline{c}$, $s\overline{s}$,	2.8	2200
$e^+e^- \to \mu^+\mu^-$	0.8	640
$e^+e^- \to \tau^+\tau^-$	0.8	640
$e^+e^- \to e^+e^-$ ($\theta_{\mathrm{lab}} \geq 17°$) (Bhabha scattering)	44	$350^{(a)}$
$e^+e^- \to \gamma\gamma$ ($\theta_{\mathrm{lab}} \geq 17°$)	2.4	$19^{(a)}$
2γ processes ($\theta_{\mathrm{lab}} \geq 17°$ and $p_t \geq 0.1\,\mathrm{GeV}/c$)	~ 80	~ 15000

$^{(a)}$ rate is scaled down by a factor of 100

5 Data Processing

5.1 Data Samples

The measurement is performed on a dataset collected with the Belle II detector between 2019 and 2022 before the first long shutdown to install a new fully equipped PXD. It corresponds to an integrated luminosity of $362 \pm 2\,\text{fb}^{-1}$ containing $(387 \pm 6) \times 10^6$ $B\overline{B}$ pairs. We refer to this dataset as long shutdown 1 (LS1) dataset.

The analysis is developed in a "blind" way, i.e. on simulated data only, to avoid the introduction of a conscious or unconscious bias towards "correct" results. Once the analysis is fully implemented and verified it is "frozen" and run on real data to extract the physics parameters of interest. To account for possible differences between real data and simulated data we use so-called control channels, i.e. decay modes that are kinematically similar to our signal decay of interest.

For simulated data we use a dataset of $1448 \pm 2\,\text{fb}^{-1}$ of integrated luminosity, corresponding to a size of four times the real data. This so-called *generic simulated data*, models the physics processes of $e^+e^- \to B^0\overline{B}^0, B^+B^-, u\overline{u}, d\overline{d}, c\overline{c}, s\overline{s}$ as well as beam backgrounds in their adequate proportions. For simulations we use a series of software packages to model the physics processes:

- `KKMC` to produce continuum ($u\overline{u}$, $d\overline{d}$, $c\overline{c}$, $s\overline{s}$) background [51],
- `PYTHIA8` to simulate hadronization [52],
- `EVTGEN` to simulate decays [53],
- `PHOTOS` to simulate final state radiation [54],
- and `GEANT4` to model the detector response [55].

To develop a selection optimized for our signal channel of interest, we simulate 10M inclusive $B^0 \to K^+\pi^-\pi^0$ decays. Inclusive means, that no intermediate resonances are considered, hence they are distributed uniformly in the Dalitz plane. This makes sure that the efficiency stays flat over the Dalitz plane and we don't introduce a bias towards a region with a resonance with large amplitude.

Additionally, we utilize 2M simulated $B^- \to D^0[K^-\pi^+\pi^0]\pi^-$ decays to extract correction factors between real data and simulated data (see 8.1).

5.1.1 Generation of simulated Signal Events

In order to validate the analysis we need simulated $B^0 \to K^+\pi^-\pi^0$ decays that are generated according to our amplitude model (i.e. the *BABAR* model[1]). The procedure in Belle II

[1]The couplings are taken from the *BABAR* analysis [8], while for the resonance parameters we are using the most up-to-date values as listed in Tab. 3.1

to simulate certain events doesn't easily allow the implementation of custom amplitudes. Hence, we simulate a decay of $B^0 \to K^+\pi^-\pi^0$ via three "dummy" resonances (one in $(K^+\pi^-)$, one in $(K^+\pi^0)$ and one in $(\pi^-\pi^0)$), which are populating the edges of the Dalitz plane, and a small non-resonant component. I.e. we simulate events in the region of the Dalitz plane where we expect the contributions from the real resonances (importance sampling). The corresponding Dalitz plot in $m^2_{K^+\pi^-}$ and $m^2_{\pi^-\pi^0}$ is shown in Figure 5.1a. We then calculate weights

$$w = \frac{|\mathscr{A}_{BABAR}|^2}{|\mathscr{A}_{\text{dummy}}|^2} \tag{5.1}$$

i.e. de-weight the dummy model and re-weight our actual signal model. These weights are then used to perform accept/reject, such that we get a sample distributed according to the *BABAR* amplitude model. We use the dummy resonance model instead of a phase space only model to increase the inherently small efficiency of the accept/reject procedure (here:4%). This way of generating signal events gives us full control over the generated amplitude. The selected sub-sample is shown in Figure 5.1b.

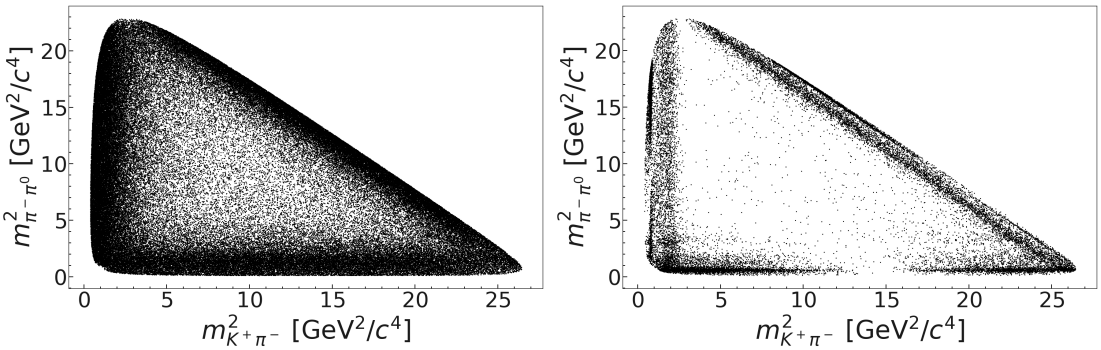

(a) Dalitz plot for three "dummy" resonances and a non-resonant contribution.

(b) Dalitz plot according to the *BABAR* measurement.

5.2 Overview of the Reconstruction and Selection Procedure

The following explains the reconstruction, selection and background suppression of B-meson candidates. The goal is to select $B^0 \to K^+\pi^-\pi^0$ decays with a high efficiency while at the same time achieving a high background rejection. The data are processed with the Belle II Analysis Software Framework (`basf2`) [56]. `basf2` reconstructs decays on a candidate based selection. This is done by filling lists of final state particles, i.e. kaons, pions and photons, from tracks in the CDC and clusters in the ECL. The four momenta of the final state particles are then subsequently combined to form B-meson candidates.
In the reconstruction we apply a loose baseline selection based on so-called "standard-lists", suggested by the Belle II performance groups. This ensures a high signal efficiency during the reconstruction. Due to the loose requirements in the standard-lists the dataset at this stage is mainly comprised of background events. To purify the sample, i.e. improve the signal

to background ratio, we impose a set of requirements optimized for the $B^0 \to K^+\pi^-\pi^0$ channel to reject background events. The main background contributor are so-called continuum events, where the e^+e^- collision produced light quark pairs ($u\bar{u}$, $d\bar{d}$, $c\bar{c}$ and $s\bar{s}$), which have a three times larger production cross-section than a pair of $b\bar{b}$ at the Belle II collision energy. In order to suppress continuum events we utilize multivariate analysis techniques (gradient boosted decision tree (GBDT)) trained on simulated data.
Since the reconstruction is candidate based it is possible two have multiple candidates in one collision event. For example you can have two tracks fulfilling the kaon requirements and hence having two candidates for the B-meson. We constrain the data set to one candidate per event by applying a single candidate selection.
For this analysis we reconstruct the following two decay modes (charge-conjugate processes are implied everywhere, except stated otherwise):

- $B^0 \to K^+\pi^-\pi^0[\gamma\gamma]$

as our signal mode of interest and the control channel

- $B^- \to D^0[K^-\pi^+\pi^0[\gamma\gamma]]\pi^-$

to evaluate the systematic uncertainty of the continuum suppression efficiency (see section 5.5) and determine correction factors for data-simulation differences (see Section 8.1).

The following sections explains the above summarized procedure in detail, starting with the reconstruction and baseline selection using the Belle II standard-lists.

5.3 Reconstruction and baseline Selection

5.3.1 HLT Hadron Skim

In Belle II we employ a variety of pre-selected datasets, known as skims, that are optimized for different decay modes of interest. These skims are designed to reduce individual computing times. The rationale behind this approach is that at the SuperKEKB collision energy of 10.58 GeV, several processes occur. The most prevalent of these is Bhabha scattering, where electron and positron particles do not collide but merely scatter off each other. Additionally, the reaction $e^+e^- \to \tau^+\tau^-$ occurs with almost the same rate as $e^+e^- \to \Upsilon(4S)$. The High-Level Trigger (HLT) hadron skim is specifically optimized for analyses studying hadronic B-meson decays. It requires that events have at least three 'good' tracks. A 'good' track is defined as having a minimum transversal momentum of 0.2 GeV/c and originating within 4 cm along the z-axis and 2 cm in the transversal direction from the interaction point. This criterion rejects $e^+e^- \to \tau^+\tau^-$ events, which typically have a low multiplicity (i.e., a small number of tracks). Furthermore, a set of requirements is imposed on electron tracks to reject Bhabha events. On the HLT hadron skim we apply the following additional requirements.

5.3.2 Charged Tracks

Charged tracks are required to have a polar angle within the CDC acceptance [17°, 150°] and have at least 20 hits. They are required to have a distance of closest approach to the interaction point of less than 0.5 cm in transversal direction and less than 2 cm along the

z-axis. Finally, we assign them a kaon or/and pion hypothesis if their respective kaon/pion particle ID is larger than 0.1.

5.3.3 Neutral Pions

Neutral pions a are formed from a pair of photons. Each photon must have an energy $> 30\,\mathrm{MeV/c^2}$ deposited in more than one ECL crystal and a timing within 200 ns of the event. The corresponding polar angle of the cluster has to be within [0.2976 rad, 2.6180 rad]. The diphoton mass has to be within $105\,\mathrm{MeV}/c^2 < m_{\gamma\gamma} < 170\,\mathrm{MeV}/c^2$.

5.3.4 D^0 Reconstruction

The D^0 mesons are reconstructed from a charged kaon, a charged pion and a neutral pion, requiring their invariant mass to be within $[1.82\,\mathrm{GeV}/c^2, 1.9\,\mathrm{GeV}/c^2]$, which corresponds to 3σ of the detector resolution to suppress against random combinations of a charged kaon, a charged pion and a neutral pion.

5.3.5 Signal B Reconstruction

The signal B-candidate is reconstructed from its respective decay products, fitting them to a common vertex via the `TreeFit` algorithm [57]. To improve the resolution of the reconstructed momenta, we require the B-meson to point back to the interaction point (i.e. impose a so-called IP-constraint) and constrain $m_{\gamma\gamma}$ to the nominal π^0 mass in the vertex fit.

In order to improve the resolution of the Dalitz plot and force it within its kinematic boundaries, we perform a second vertex fit where we also constrain the mass of the B^0. The second fit is exclusively used for the determination of the Dalitz variables $m_{K^+\pi^-}$, $m_{K^+\pi^0}$ and $m_{\pi^-\pi^0}$.

To characterize the kinematics of the B-candidate we introduce two variables.The energy difference between the reconstructed energy of the B-meson and the beam energy, evaluated in the center-of-mass system

$$\Delta E = E^*_B - E^*_{beam}, \tag{5.2}$$

and the so called beam-constrained mass, which represents the reconstructed mass of the B-candidate but with the reconstructed energy replaced by the beam energy, which is precisely know

$$M_{\mathrm{bc}} = \sqrt{E^{*2}_{beam} - |\vec{p}^{\,*}_B|^2}. \tag{5.3}$$

Plots of the typical distributions of signal and background components in ΔE and M_{bc} are shown in Figure 5.2. Correctly reconstructed B-decays peak at zero in ΔE and at the B-mass in M_{bc}. Mis-reconstructed B-decays, e.g. where a pion was mis-identified as a kaon, are shifted away from zero in ΔE. Events where $e^+e^- \to q\bar{q}$ with $q\bar{q}$ being light quarks (u, d, c, s) are flat in ΔE and M_{bc}, with a drop-off at half of the beam energy in M_{bc}. We require $-0.4 < \Delta E < 0.4\,\mathrm{GeV}$ and $5.2\,\mathrm{GeV}/c^2 < M_{\mathrm{bc}}$.

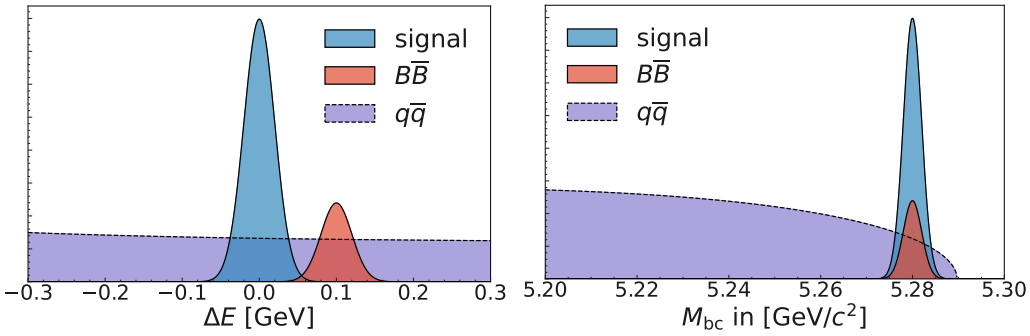

Figure 5.2: Exemplary plots of the typical distributions of signal and backgrounds in ΔE (left) and M_{bc} (right).

5.3.6 Tag B Reconstruction

To calculate variables describing the shape of the events, we also reconstruct the accompanying tag B-meson. These variables are used for background suppression (see Section 5.5). The tag B is reconstructed from all remaining particles in the event, applying soft selection criteria to suppress beam-induced backgrounds. We fit them to a common vertex via the `KFitter` algorithm.

5.4 Optimization of the Selection

The above reconstruction describes loose requirements using the standard-lists as suggested by the Belle II performance groups. This makes sure the efficiency to reconstruct a signal event is high. On the other hand many background events are also reconstructed. Hence, we aim to further tune the selection, specifically for the $B^0 \to K^+\pi^-\pi^0$ channel to purify the data (i.e. reject background events and retain signal events). We perform an optimization in a signal enhanced window defined as $-0.15 < \Delta E < 0.1\,\mathrm{GeV}$ and $5.265\,\mathrm{GeV}/c^2 < M_{\mathrm{bc}}$, where we expect the best sensitivity. In order to not bias the selection in certain regions of the Dalitz plane we use a simulated $B^0 \to K^+\pi^-\pi^0$ sample which was generated flatly in the Dalitz plane. We are using the `Differential Evolution` algorithm [58] implemented in the `SciPy` framework [59]. `Differential Evolution` is a general optimization algorithm. The function that is optimized is the significance of a signal over some background

$$\frac{S}{\sqrt{S+B}} \tag{5.4}$$

where S and B are the number of signal and background events.
In the optimization we are including the invariant mass of the two photons forming the π^0 as well as the helicity angle of the π^0, which is the angle between the momentum difference of the two photons in the rest-frame of the π^0 and the momentum of the π^0 in the lab-frame. Optimizing those suppresses fake π^0's, i.e. random combinations of two photons.
Furthermore, the binary kaon ID is included to suppress mis-identified pions, i.e. from the

decay $B^0 \to \pi^+\pi^-\pi^0$.
Finally, we optimize the M_{bc} window in order to suppress against random combinations of a kaon, pion and a neutral pion.
The boundaries and the best values after the optimization are listed in Tab. 5.1

Table 5.1: Boundaries of the variables used in the optimization of the selection. The right column lists the best values found by the `Differential Evolution` algorithm.

boundary	best value
lower bound of the $m_{\gamma\gamma}$ invariant mass between [0.105 GeV/c^2, 0.135 GeV/c^2]	0.122 GeV/c^2
upper bound of the $m_{\gamma\gamma}$ invariant mass between [0.137 GeV/c^2, 0.170 GeV/c^2]	0.145 GeV/c^2
upper bound of the cosine of the helicity angle of the π^0 between [0.9, 1.0]	0.96
lower bound of the binary kaon ID between [0, 1]	0.96
lower bound of M_{bc} between [5.26 GeV/c^2, 5.279 GeV/c^2]	5.276 GeV/c^2
lower bound of M_{bc} between [5.281 GeV/c^2, 5.3 GeV/c^2]	5.283 GeV/c^2

After the baseline selection the significance is 2.58 After the above described optimized selection the significance is 5.51, i.e. we are able to double the signal significance.

5.5 Continuum Suppression

After the above described selection the dominant background consists of so-called continuum events. These are events where the e^+e^- collision creates light quark pairs ($u\overline{u}$, $d\overline{d}$, $c\overline{c}$ and $s\overline{s}$), which hadronize and can result in the same final state particles as our signal B-meson decay. The cross-section of continuum production is about three times larger than the one for B-meson pair production.
Since the collision energy is just above the production threshold of a B-meson pair, the B-mesons are almost at rest in the center-of-mass system and decay with an approximately isotropic topology (see Fig. 5.3). The lighter continuum $q\overline{q}$ pairs have leftover energy and the final state particles are boosted in the direction of the "mother quark", resulting in a jet-like decay topology.

Combining several topological variables describing the shape of the events in multivariate analysis techniques allows the suppression of continuum events. We are training a GBDT via the `LightGBM` framework [60] on the following 17 variables (internal `basf2` variable names):

- `DeltaZ` - spatial distance between signal and tag-side B-meson vertices along beam direction,
- `DeltaZErr` - uncertainty on `DeltaZ`,
- `dcosTheta` - polar angle of the signal B-meson vertex with respect to the IP,
- `dphi` - azimuthal angle of the signal B-meson vertex with respect to the IP,
- `FBDT_qrCombined` - combined flavor (q) times dilution factor (r),
- 4 `CLEO` cones,
- 4 `Kakuno-Super-Fox-Wolfram` moments,

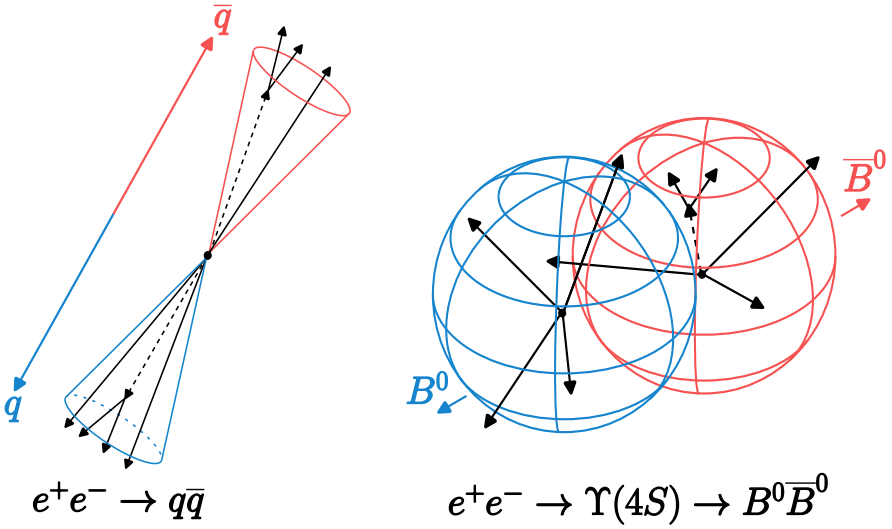

Figure 5.3: Decay topology for continuum events (left) and $B\overline{B}$ events (right).

- `qpSlowPion` - charge of the tag-side track with highest probability of being a slow pion from the decay of a primary D^* multiplied by the respective probability,
- `qpKaonPion` - charge of the tag-side track with the highest probability of being a kaon from the decay of a D coming from a $D^* \to X\pi D$ decay multiplied by the respective probability,
- `qpLambda` - flavor of the tag-side candidate reconstructed from a proton and pion with the highest probability of being a Λ multiplied by its respective probability,
- `qpFSC` - charge of the tag-side track with highest probability of being a slow pion from the decay of a D^*, correlated with high momentum primary particles, multiplied by the respective probability.

A comparison of the signal and $q\overline{q}$ distributions for the most important input variable, `DeltaZ`, is shown in Figure 5.4. Such plots for all input variables are shown in the Appendix A.2

The selected variables were chosen such that the linear correlation coefficient between them and ΔE and the Dalitz variables $m_{K^+\pi^-}$, $m_{K^+\pi^0}$ and $m_{\pi^-\pi^0}$ are below 3% (arbitrary choice) to make sure the output of the GBDT doesn't deform ΔE and the Dalitz plot. This is important since otherwise background events could mimic the shape of signal events, which would result in reduced sensitivity in the final fit.
Furthermore, we ensure a good modeling by comparing their distributions between simulated data and real data in the $B^- \to D^0[K^-\pi^+\pi^0]\pi^-$ control channel.
The output of the GBDT can be seen in Figure 5.5 Continuum events peak at zero while signal B-meson events peak at one.

The corresponding receiver operating characteristic (ROC) curve is shown in Figure 5.6. We achieve an area under curve (AUC) of 0.934. To verify the GBDT doesn't affect the background shape of the ΔE distribution we plot them with different requirements imposed

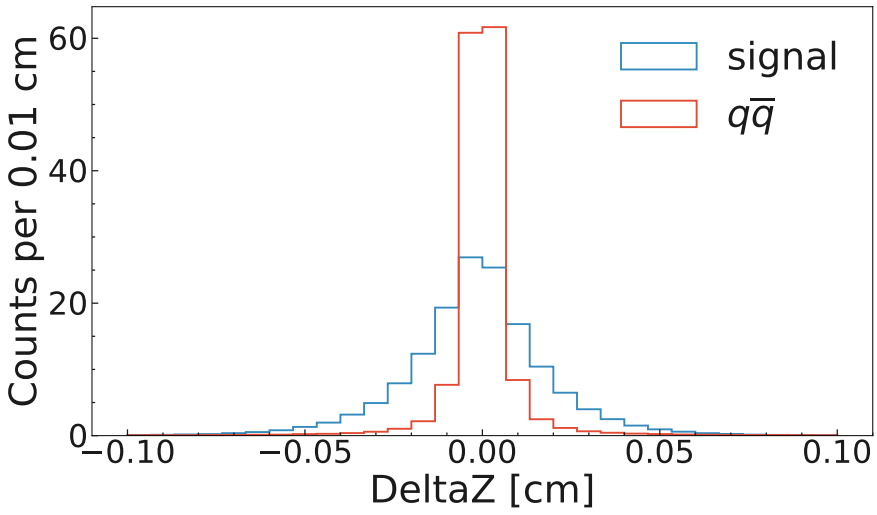

Figure 5.4: Comparison of the `DeltaZ` signal and $q\bar{q}$ distributions.

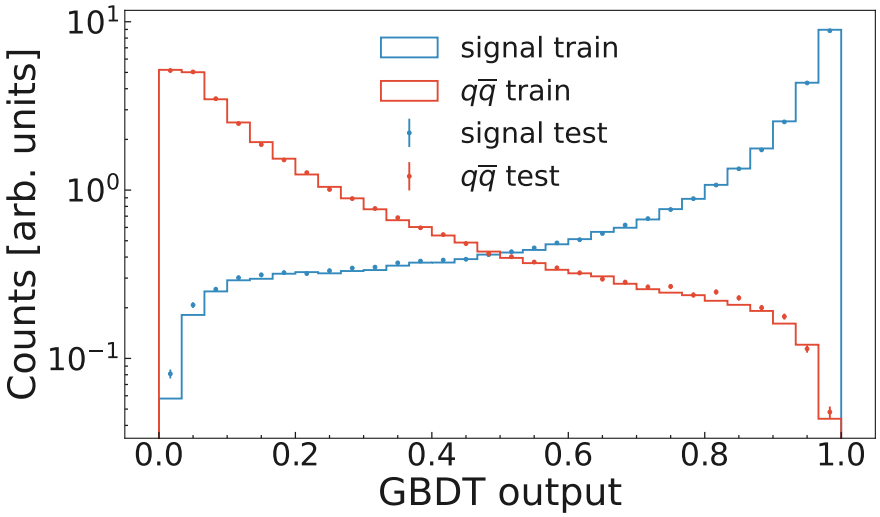

Figure 5.5: Output of the GBDT.

on the GBDT output (see Figure 5.7). All distributions overlay within their uncertainties, indicating no effects.

We impose a cut on the GBDT output to be larger 0.7, such that $\approx 95\%$ of the remaining continuum is rejected while we retain $\approx 75\%$ of the signal events.
Since we include the GBDT output in the final fit we perform a transformation of the raw output to obtain simple shapes, used as models in the fit. We are using the rarity transform as described in [61] and introduce the naming C'. Signal events are uniformly

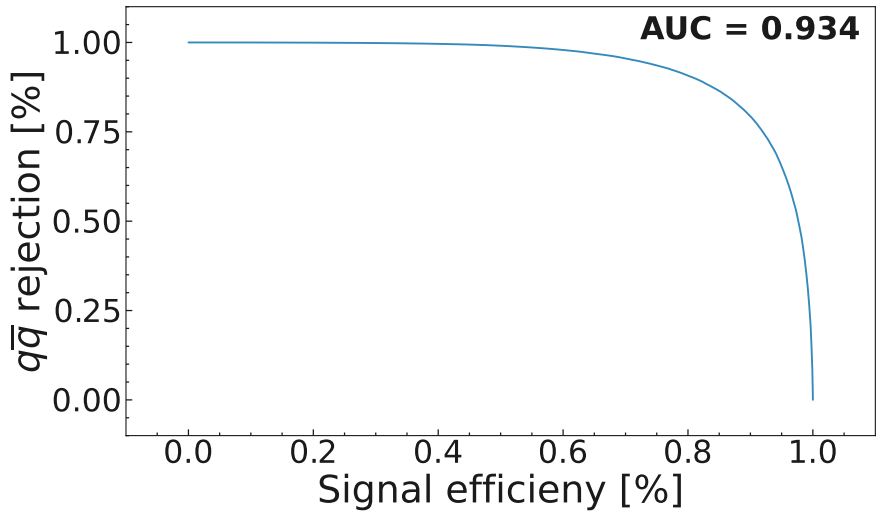

Figure 5.6: ROC curve of the GBDT output.

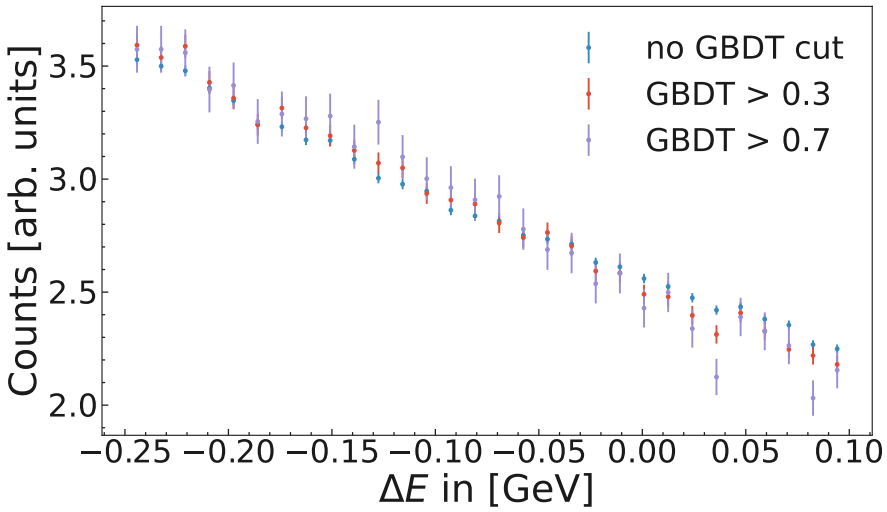

Figure 5.7: ΔE distribution of continuum events with different cuts on the GBDT output.

distributed between 0 and 1 in C' while continuum events obey an exponential distribution (see Fig. 5.8).

5.6 Single Candidate Selection

After the final selection including the continuum suppression each event contains on average 1.21 candidates in generic simulated data and 1.20 in real data. For simulated

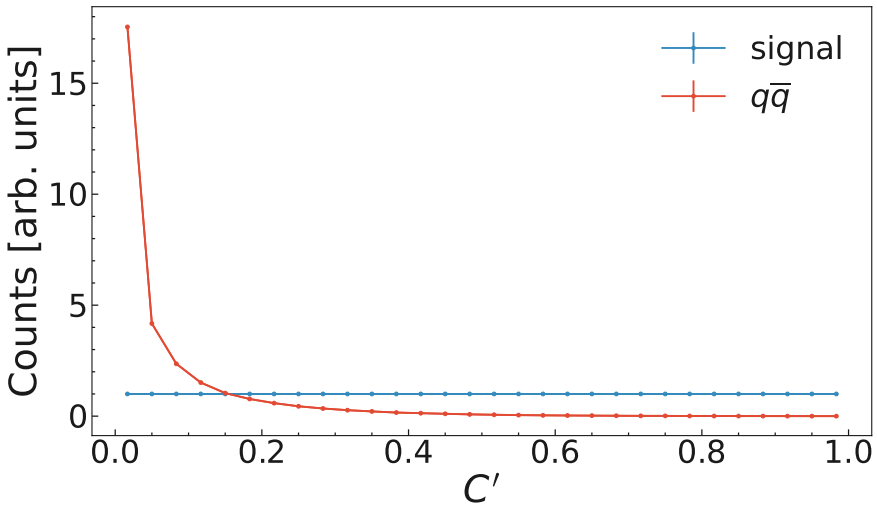

Figure 5.8: Rarity transform of the GBDT output. Signal events are flat while continuum events follow an exponential shape.

$B^0 \to K^+\pi^-\pi^0$ events the multiplicity is 1.08. We select a single candidate per event via the following method:

1. If the B-meson candidates differ by a π^0 we select the one with the smallest photon asymmetry defined as $A_\gamma = \frac{|E_\gamma^1 - E_\gamma^2|}{E_\gamma^1 + E_\gamma^2}$.
2. If there are still multiple candidates we select the one with the best B-meson vertex fit.

In signal events with multiple candidates we select the correct candidate in 62% of the cases. A random single candidate selection yields an efficiency of 38%.

5.7 Final Sample Composition

We summarize the full selection as described above in Table 5.2. The efficiencies for $B^0 \to K^+\pi^-\pi^0$ events evenly distributed in the Dalitz plane after each selection step are summarized in Table 5.3. The final data sample contains $B^0 \to K^+\pi^-\pi^0$ decays, non-interfering $B^0 \to \overline{D}^0[K^+\pi^-]\pi^0$ and $B^0 \to D^-[\pi^-\pi^0]K^+$ decays, $e^+e^- \to q\overline{q}$ continuum events and other generic $B\overline{B}$ decays. Their distributions in ΔE and C' are shown in Figure 5.9.

5.7.1 $B\overline{B}$ Components

The $B\overline{B}$ background component can be further decomposed into several decay modes. The largest components are summarized in Table 5.4.

Table 5.2: Summary of the selection requirements of the $B^0 \to K^+\pi^-\pi^0$ channel.

charged tracks
$17° < \theta < 150°$
nCDCHits > 20
dr $< 0.5\,\text{cm}$
abs(dz) $< 2\,\text{cm}$
$\mathcal{L}_K > 0.1$ for kaons
$\mathcal{L}_{K/\pi} > 0.96$ for kaons
$\mathcal{L}_\pi > 0.1$ for pions
photons
E $> 30\,\text{MeV}/c^2$
clusterNHits > 1.5
abs(clusterTiming) $< 200\,\text{ns}$
$0.2967 <$ clusterTheta < 2.6180
π^0
$0.122 < m_{\gamma\gamma} < 0.145\,\text{GeV}/c^2$
cos(HelicityAngle) < 0.96
$\mathbf{B^0}$
$5.276 < M_{\text{bc}} < 5.283\,\text{GeV}/c^2$
$-0.25 < \Delta E < 0.1\,\text{GeV}$
Continuum suppression GBDT > 0.7

Table 5.3: Summary of cumulative efficiencies for correctly reconstructed $B^0 \to K^+\pi^-\pi^0$ decays, generated evenly in the Dalitz plane, after each step of the selection.

	$\varepsilon(B^0 \to K^+\pi^-\pi^0)$
Reconstruction and baseline selection	40.7%
π^0 selection	35.0%
binary kaon ID	27.8%
M_{bc} and ΔE selection	20.0%
Continuum suppression GBDT	14.5%
Single candidate selection	14.3%

In the following we group the $B\overline{B}$ background components into a $B \to$ *charm* and a $B \to$ *charmless* component, where the former refers to decays with $\overset{(-)}{b} \to \overset{(-)}{c}$ transitions (i.e. $B \to D^{(*)}$...) and the latter refers to decays without any $\overset{(-)}{c}$ quark.

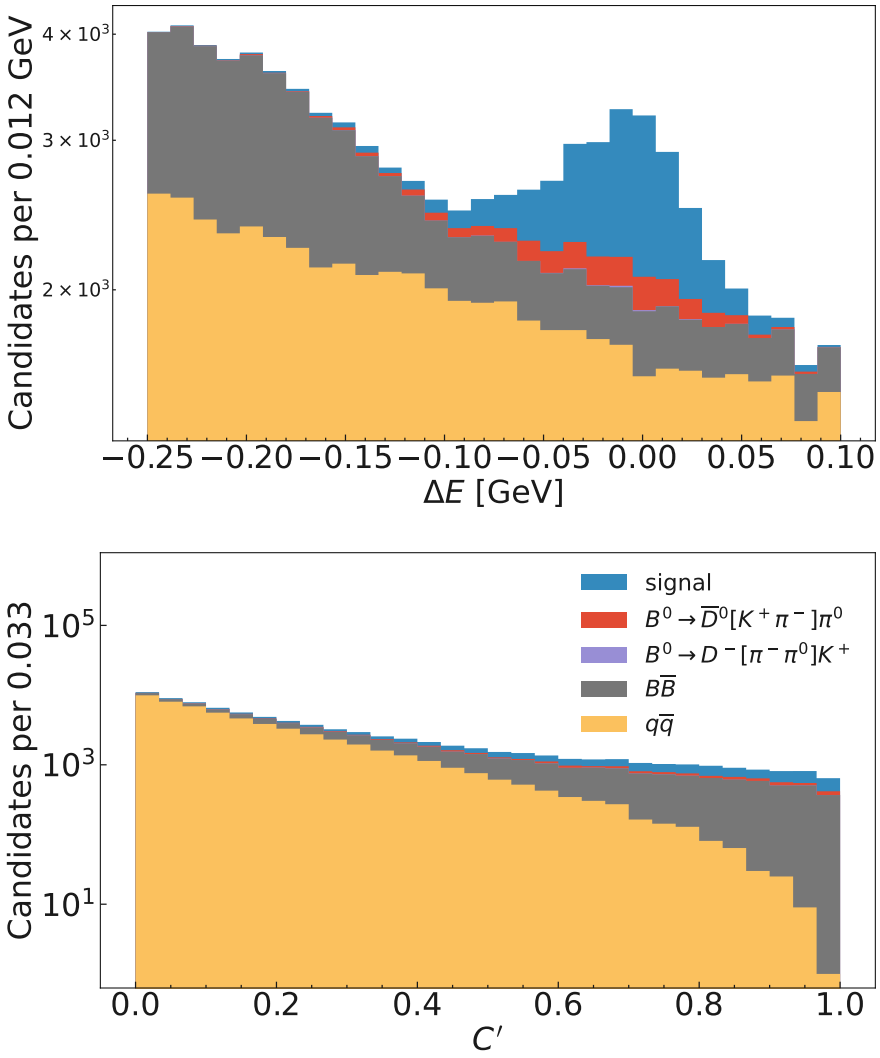

Figure 5.9: Final sample composition in ΔE (top) and C' (bottom).

Table 5.4: Breakdown of the $B\overline{B}$ background decay modes in $362\,\mathrm{fb}^{-1}$ of simulated data.

channel	# events
$B^- \to D^0[K^-\pi^+]\rho^-[\pi^0\pi^-]$	1724
$\overline{B}^0 \to D^{*0}[D^0[K^-\pi^+]\pi^0]\pi^0$	146
$B^- \to D^0[K^-\pi^+\pi^0]\pi^-$	60
$B^0 \to X_{sd}[K^+\pi^-]\gamma$	40
$B^0 \to \pi^+\pi^-\pi^0$	36
$B^- \to \rho^0[\pi^+\pi^-]K^-$	39
$B^- \to D^0[K^0_S[\pi^+\pi^-]K^+K^-]\pi^-$	26
$B^+ \to \rho^+[\pi^+\pi^0]K^+\pi^-$	25
others	2129
total	4225

6 The Fit Model

We perform an extended maximum likelihood fit to the unbinned distributions of m', θ', ΔE and C', simultaneously to the $B^0 \to K^+\pi^-\pi^0$ and $\overline{B}^0 \to K^-\pi^+\pi^0$ sample, to extract the resonance couplings, yields and CP-violating asymmetries. If not stated otherwise the used PDFs are products of the Dalitz plot PDF, the PDF in ΔE and the PDF in C'. I.e. $\mathcal{P}(m', \theta', \Delta E, C') = \mathcal{P}(m', \theta') \cdot \mathcal{P}(\Delta E) \cdot \mathcal{P}(C')$

The fit is performed using the `zfit` framework [62]. This chapter describes the parametrization of the signal and background components.

6.1 The Signal Model

6.1.1 Signal Dalitz PDF

The physics intensity distribution in the Dalitz plot variables, i.e. without detector effects, is described by the absolute squared of the amplitude as described in Sec. 3.1. The signal Dalitz PDF accounting for detector effects is then given as

$$\mathcal{P}_{\text{sig}}(m', \theta') = \frac{1}{N} \cdot \eta(m'_{gen}, \theta'_{gen}) \cdot |J(m'_{gen}, \theta'_{gen})| \cdot |\mathscr{A}(m'_{gen}, \theta'_{gen})|^2 \circledast R(m', \theta'; m'_{gen}, \theta'_{gen}), \tag{6.1}$$

where

- m' and θ' are the reconstructed quantities, while m'_{gen} and θ'_{gen} are the generated or produced Dalitz plane positions.
- $\frac{1}{N}$ is the normalization of the PDF, i.e.

$$\begin{aligned} N = \int_0^1 \int_0^1 \eta(m'_{gen}, \theta'_{gen}) \cdot |J(m'_{gen}, \theta'_{gen})| \cdot |\mathscr{A}(m'_{gen}, \theta'_{gen})|^2 \circledast \\ \circledast R(m', \theta'; m'_{gen}, \theta'_{gen}) \; dm' d\theta'. \end{aligned} \tag{6.2}$$

- $\eta(m'_{gen}, \theta'_{gen})$ is the so-called acceptance, which models differences of acceptance and efficiency in the Dalitz plane.
- $|J(m'_{gen}, \theta'_{gen})|$ is the determinant of the Jacobian of the transformation from the standard to square Dalitz plot variables (see Eq. 3.33).
- $|\mathscr{A}(m'_{gen}, \theta'_{gen})|^2$ is the amplitude model.
- $R(m', \theta'; m'_{gen}, \theta'_{gen})$ is the resolution function to model detector resolution effects, i.e. events being reconstructed with different kinematics than they were produced.

We observe, that resolution effects can be neglected for correctly reconstructed signal events (see Fig. 6.2), which we call truth-matched (TM) events. Signal events with some error during reconstruction are called self-cross-feed (SCF) events. These are predominately

events where the neutral pion or a photon from the tag B-meson is wrongly used in the reconstruction of the signal B-meson. For SCF events the resolution cannot be neglected. Therefore, we split the signal PDF into a part describing the TM events and one part describing the SCF events

$$\mathcal{P}_{sig}(m', \theta', \Delta E, C') = (1 - \overline{f}_{\mathrm{SCF}}) \cdot \mathcal{P}_{\mathrm{TM}}(m', \theta', \Delta E, C') + \overline{f}_{\mathrm{SCF}} \cdot \mathcal{P}_{\mathrm{SCF}}(m', \theta', \Delta E, C'). \quad (6.3)$$

$\overline{f}_{\mathrm{SCF}}$ is the self-cross-feed fraction averaged over the Dalitz plane which is given by[1]

$$\overline{f}_{\mathrm{SCF}} = \frac{\int_0^1 \int_0^1 f_{\mathrm{SCF}}(m', \theta') \cdot \eta(m', \theta') \cdot |J(m', \theta')| \cdot |\mathscr{A}(m', \theta')|^2 \; dm' d\theta'}{\int_0^1 \int_0^1 \eta(m', \theta') \cdot |J(m', \theta')| \cdot |\mathscr{A}(m', \theta')|^2 \; dm' d\theta'} \quad (6.4)$$

where $f_{\mathrm{SCF}}(m', \theta')$ is the Dalitz plane dependent self-cross-feed fraction.

For TM events we assume the resolution to be a Dirac delta function and the TM Dalitz plot PDF becomes

$$\mathcal{P}_{\mathrm{TM}}(m', \theta') = (1 - f_{\mathrm{SCF}}(m', \theta')) \cdot \eta(m', \theta') \cdot |J(m', \theta')| \cdot \frac{|\mathscr{A}(m', \theta')|^2}{N_{\mathrm{TM}}} \quad (6.5)$$

with the normalization

$$N_{\mathrm{TM}} = \int_0^1 \int_0^1 (1 - f_{\mathrm{SCF}}(m', \theta')) \cdot \eta(m', \theta') \cdot |J(m', \theta')| \cdot |\mathscr{A}(m', \theta')|^2 \; dm' d\theta' \quad (6.6)$$

The Dalitz plot SCF PDF is given as

$$\mathcal{P}_{\mathrm{SCF}}(m', \theta') = f_{\mathrm{SCF}}(m'_{gen}, \theta'_{gen}) \cdot \eta(m'_{gen}, \theta'_{gen}) \cdot |J(m'_{gen}, \theta'_{gen})| \cdot \frac{|\mathscr{A}(m'_{gen}, \theta'_{gen})|^2}{N_{\mathrm{SCF}}} \circledast \\ \circledast \, R_{\mathrm{SCF}}(m', \theta'; m'_{gen}, \theta'_{gen}) \quad (6.7)$$

and the normalization is

$$N_{\mathrm{SCF}} = \int_0^1 \int_0^1 f_{\mathrm{SCF}}(m'_{gen}, \theta'_{gen}) \cdot \eta(m'_{gen}, \theta'_{gen}) \cdot |J(m'_{gen}, \theta'_{gen})| \cdot |\mathscr{A}(m'_{gen}, \theta'_{gen})|^2 \circledast \\ \circledast \, R_{\mathrm{SCF}}(m', \theta'; m'_{gen}, \theta'_{gen}) \; dm' d\theta'. \quad (6.8)$$

Determination of Acceptance and Self-Cross-Feed Fraction

The acceptance and Dalitz plane dependent SCF fraction are extracted from simulated events that are uniformly distributed in the Dalitz plane. The acceptance[2] is defined as

$$\eta(m'_{gen}, \theta'_{gen}) = \frac{\text{reconstructed events}(m'_{gen}, \theta'_{gen})}{\text{generated events}(m'_{gen}, \theta'_{gen})} \quad (6.9)$$

[1] Strictly speaking the integrals run also over ΔE and C', however since their shapes are not a physics model, but extracted from simulated data, $f_{\mathrm{SCF}}(\Delta E)$ and $f_{\mathrm{SCF}}(C')$ are implicitly encoded in the PDFs, which are normalized over the definition range and drop out.

[2] The Belle II simulation does not store the four momenta before final state radiation (i.e. PHOTOS). Therefore we cannot simply correct this effect. However, the effects are minor and we deem them negligible.

and the SCF fraction as

$$f_{\mathrm{SCF}}(m'_{gen}, \theta'_{gen}) = \frac{\text{SCF events}(m'_{gen}, \theta'_{gen})}{\text{TM events}(m'_{gen}, \theta'_{gen}) + \text{SCF events}(m'_{gen}, \theta'_{gen})}. \tag{6.10}$$

They are both implemented as a spline-interpolation of a two dimensional histogram in the square Dalitz plane and are show in Figure 6.1. At low values of m' the acceptance as

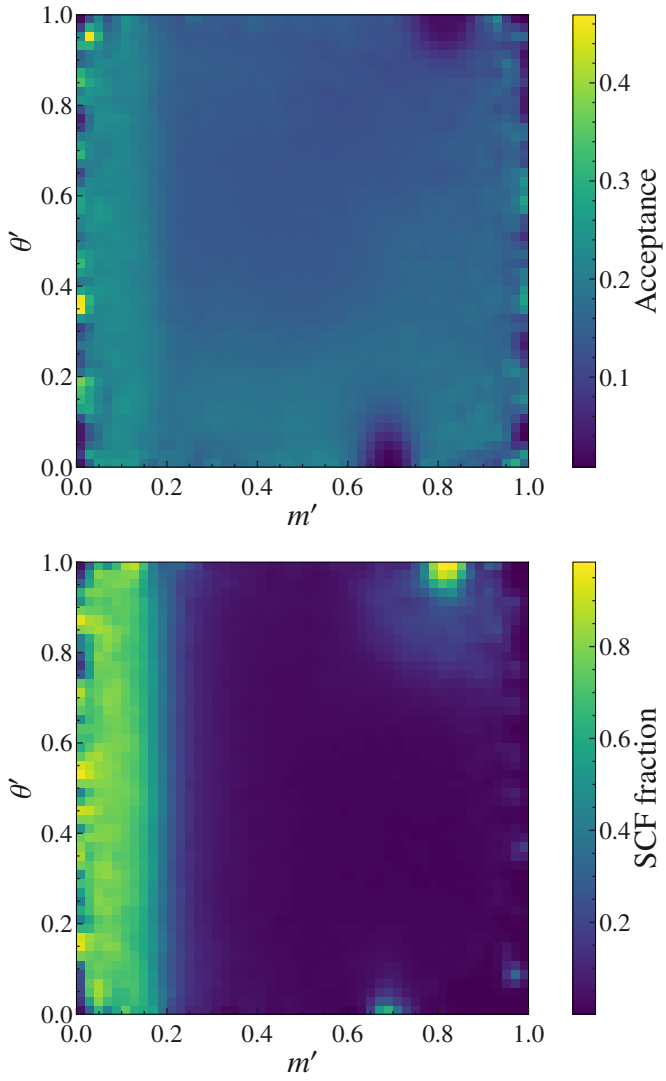

Figure 6.1: Square Dalitz plot dependent acceptance (top) and SCF fraction (bottom).

well as the SCF fraction rise. These are events with low-momentum neutral pions, where a neutral pion from the tag B-meson is wrongly used in the reconstruction of the signal B-meson.

The two half circles at the bottom and top at $m' = 0.7$ and $m' = 0.8$ correspond to low-momentum K^+ and π^-, i.e. where the whole kinematic energy is carried away in the

other two-body system and they do not reach the CDC to be reconstructed. These events can only be reconstructed if a wrong K^+ or π^- is used from the tag-B-meson. Therefore, the SCF fraction peaks.

Resolution Function

To evaluate the effects of detector resolution we compare, in simulated events, the generated Dalitz plane positions with the reconstructed ones. Figure 6.2 shows the resolution for TM

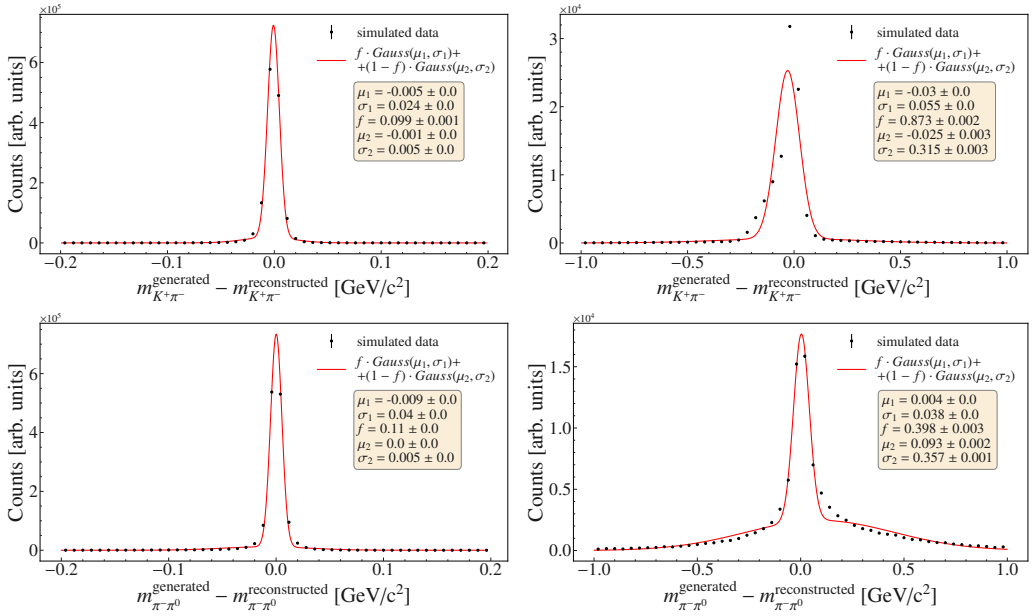

Figure 6.2: Detector resolution for TM events (left) and SCF events (right) for $m_{K^+\pi^-}$ (top) and $m_{\pi^-\pi^0}$ (bottom). A fit of two Gaussian functions is overlaid.

and SCF events in $m_{K^+\pi^-}$ and $m_{\pi^-\pi^0}$. Each distribution is fitted with the sum of two gaussians. For the TM events the fits are dominated by the second gaussian with widths of $\sim 5\,\text{MeV}$. Since the narrowest resonance in our amplitude model has a natural width of 50 MeV we can safely neglect resolution effects. I.e. we assume the resolution to be a Dirac delta function.

However, for SCF events the resolution needs to be taken into account. We implement $R_{\text{SCF}}(m', \theta'; m'_{gen}, \theta'_{gen})$ as a four-dimensional histogram taken from a large sample of simulated data. The resolution function is normalized such that

$$\int_0^1 \int_0^1 R_{\text{SCF}}(m', \theta'; m'_{gen}, \theta'_{gen})\, dm' d\theta' = 1 \quad \forall (m'_{gen}, \theta'_{gen}). \tag{6.11}$$

To avoid the computationally demanding convolution in the minimization, we pre-calculate the SCF PDF on the same grid as the resolution histogram, such the the convolution becomes a sum over the bins.

6.1.2 Normalization of the Signal PDF

After the convolution the SCF PDF is a two dimensional histogram in m' and θ'. Therefore, the integral in Equation 6.8 becomes a sum over the bins

$$N_{\mathrm{SCF}} = \sum_{m'} \sum_{\theta'} f_{\mathrm{SCF}}(m'_{gen}, \theta'_{gen}) \cdot \eta(m'_{gen}, \theta'_{gen}) \cdot |J(m'_{gen}, \theta'_{gen})| \cdot |\mathscr{A}(m'_{gen}, \theta'_{gen})|^2 \circledast \\ \circledast R_{\mathrm{SCF}}(m', \theta'; m'_{gen}, \theta'_{gen}) \tag{6.12}$$

For computational reasons, we pre-calculate the normalization of the TM PDF as given in Equation 6.6. For this we write the absolute square of the amplitude as

$$|\mathscr{A}(m', \theta')|^2 = \sum_{i,j} c_i c_j^* \psi_i(m', \theta') \psi_j^*(m', \theta'). \tag{6.13}$$

Since the couplings c_i and c_j^* are independent of the Dalitz plane position they can be extracted from the integrals. Therefore, the normalization becomes

$$N_{\mathrm{TM}} = \sum_{i,j} c_i c_j^* \int_0^1 \int_0^1 (1 - f_{\mathrm{SCF}}(m', \theta')) \cdot \eta(m', \theta') \cdot |J(m', \theta')| \cdot \\ \cdot \psi_i(m', \theta') \psi_j^*(m', \theta') \; dm' d\theta'. \tag{6.14}$$

The integrals do not contain any parameter that we want to fit and are therefore constant. They can be pre-calculated in order to speed up the minimization process. If the amplitude model includes N resonances, this results in $\frac{N(N+1)}{2}$ integrals. We evaluate the integrals via Monte-Carlo integration over a large number of events distributed uniformly in (m', θ'). (I.e. we evaluate the function

$$(1 - f_{\mathrm{SCF}}(m', \theta')) \cdot \eta(m', \theta') \cdot |J(m', \theta')| \cdot \psi_i(m', \theta') \psi_j^*(m', \theta') \tag{6.15}$$

at many (m', θ') points. An estimate for the integral is then given as the average of all function values times the area of the integral range, which is one for the square Dalitz plane.)

6.1.3 The Signal ΔE PDF

The ΔE distribution of TM events is strongly dependent on the position in the Dalitz plane (see Fig. 6.3) This dependency stems from the kinematics of the neutral pion. At low m' the π^0 has low momentum. Hence, it only contributes a small part to ΔE and the resolution is mainly given by the track resolution of the charged kaon and pion. For higher momentum π^0s the ΔE resolution is dominated by the worse π^0 resolution, which results in a broadening of the distribution.

In order to treat this dependency, we fit the ΔE distribution in 14 slices of m' with a double-sided Crystal Ball function

$$f(x; \mu, \sigma, \alpha_L, n_L, \alpha_R, n_R) = \begin{cases} A_L \cdot (B_L - \frac{x-\mu}{\sigma})^{-n_L}, & \text{for } \frac{x-\mu}{\sigma} < -\alpha_L \\ exp(-\frac{(x-\mu)^2}{2\sigma^2}), & \text{for } -\alpha_L \leq \frac{x-\mu}{\sigma} \leq \alpha_R \\ A_R \cdot (B_R - \frac{x-\mu}{\sigma})^{-n_R}, & \text{for } \frac{x-\mu}{\sigma} > \alpha_R \end{cases} \tag{6.16}$$

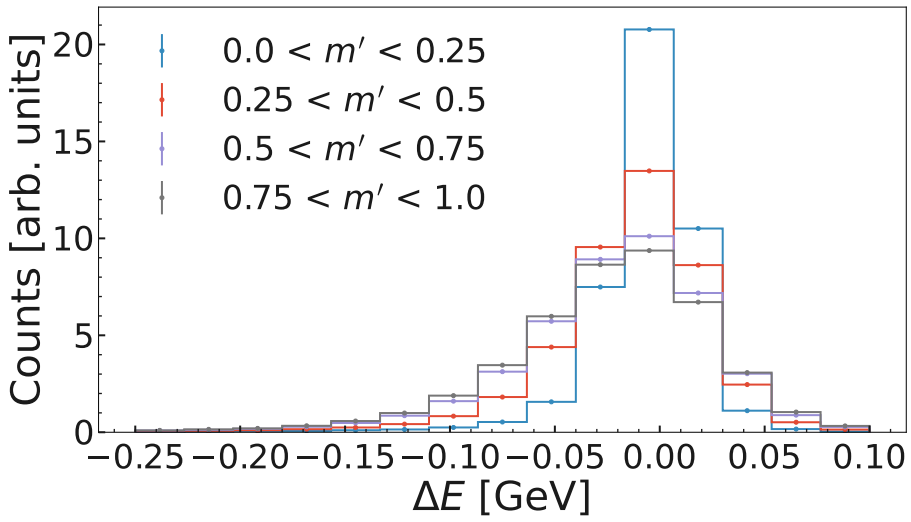

Figure 6.3: ΔE distribution of TM events in slices of the square Dalitz plane position m'. A strong dependency can be seen.

with

$$A_{L/R} = \left(\frac{n_{L/R}}{|\alpha_{L/R}|}\right)^{n_{L/R}} \cdot exp(-\frac{|\alpha_{L/R}|^2}{2})$$
$$B_{L/R} = \frac{n_{L/R}}{|\alpha_{L/R}|} - |\alpha_{L/R}|.$$

The fit results for three exemplary slices of m' are shown in Fig. 6.4. The ΔE PDF is implemented as a conditional PDF. This means if an event falls into the first bin of m' the ΔE PDF uses the shape determined in the first bin. The two-dimensional ΔE-m' conditional PDF can be seen in Fig. 6.5
No large dependencies between Dalitz plane position and ΔE are observed for the SCF events. We model the ΔE distribution for the SCF events with the sum of a double-sided Crystal Ball function and a first order Chebyshev polynomial. The fit shape is shown in Figure 6.6.

6.1.4 The Signal C' PDF

The TM and SCF C' distributions are modeled respectively with a flat line (by construction) and a third order Chebyshev polynomial and can be seen in Figure 6.7

6.2 The charmed Resonances Model

The two modes $B^0 \to \overline{D}^0[K^+\pi^-]\pi^0$ and $B^0 \to D^-[\pi^-\pi^0]K^+$ end in the same final state as the signal channel but do not interfere due to longer lifetimes of the D-mesons.

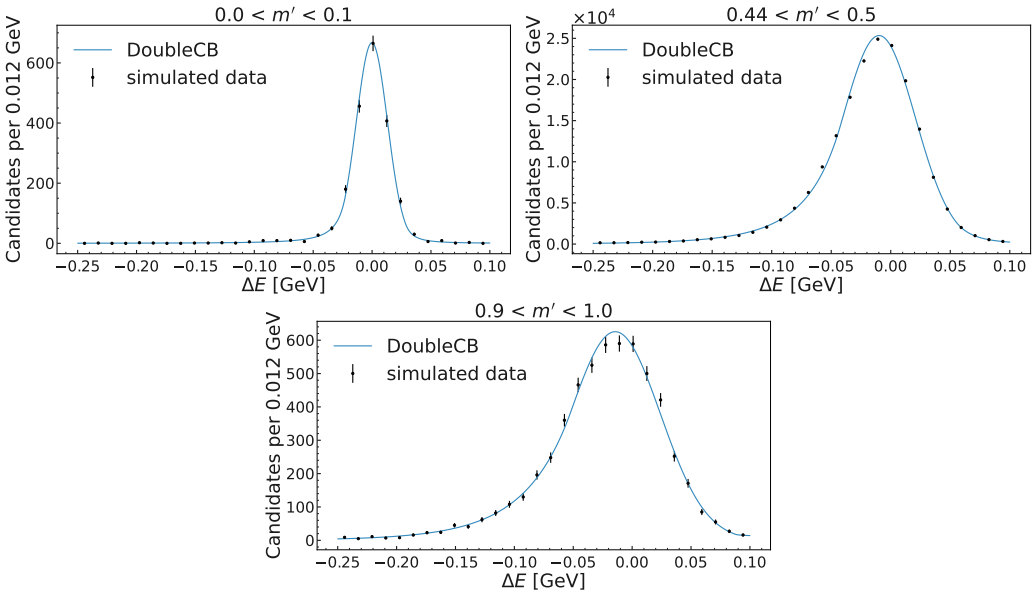

Figure 6.4: ΔE distribution in three slices of m'. The fitted double-sided Crystal Ball function is overlaid.

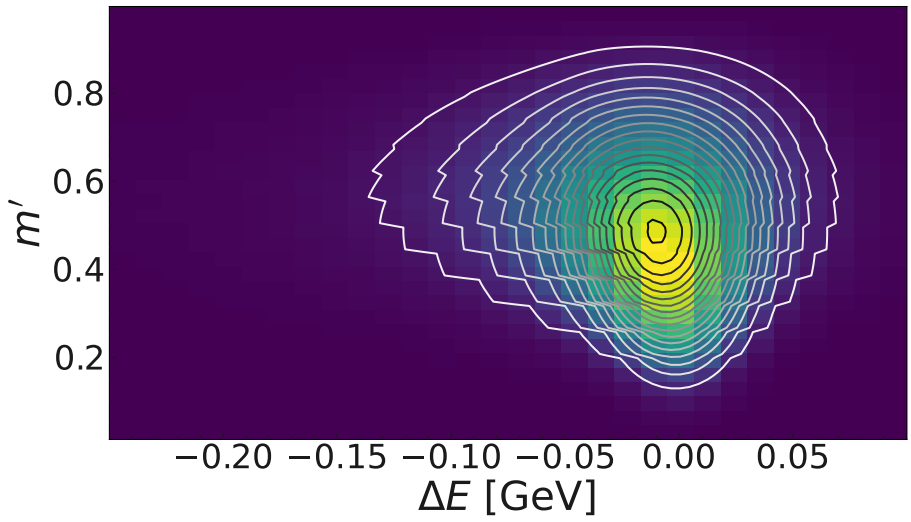

Figure 6.5: ΔE-m' histogram for TM events. The conditional ΔE-m' PDF is overlaid as the contour lines.

6.2.1 Charmed Resonance Dalitz PDF

The charmed resonances are also modeled according to Eq. 3.11. However, since they do not interfere with the charmless resonances their amplitudes are added incoherently, i.e. we add the intensities. As line shapes we are using double-sided Crystal Ball functions. The corresponding $m_{K^+\pi^-}$ and $m_{\pi^-\pi^0}$ distributions are show in Figure 6.8.

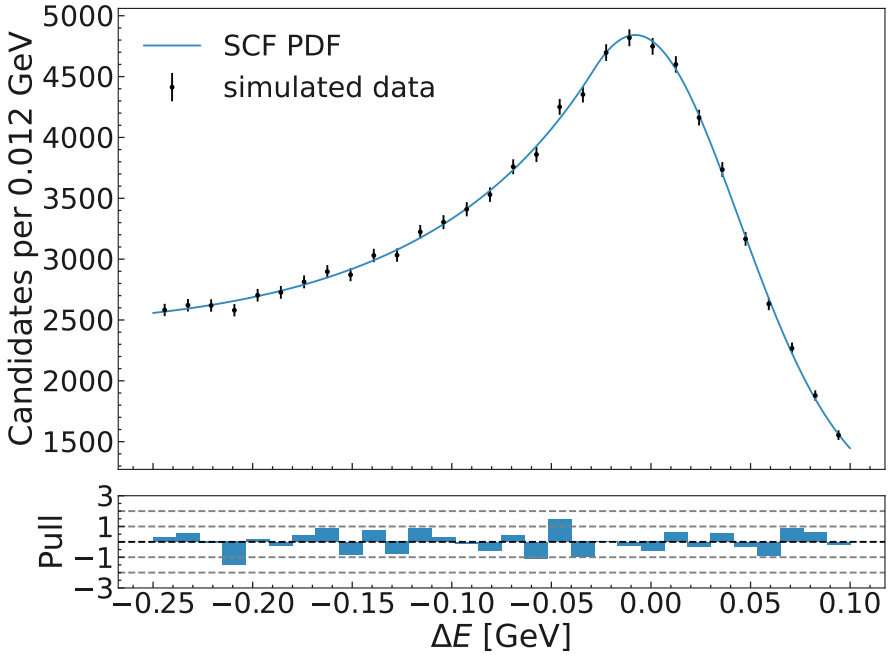

Figure 6.6: SCF ΔE distribution. A fit of double-sided Crystal Ball function and a first order Chebyshev polynomial is overlaid.

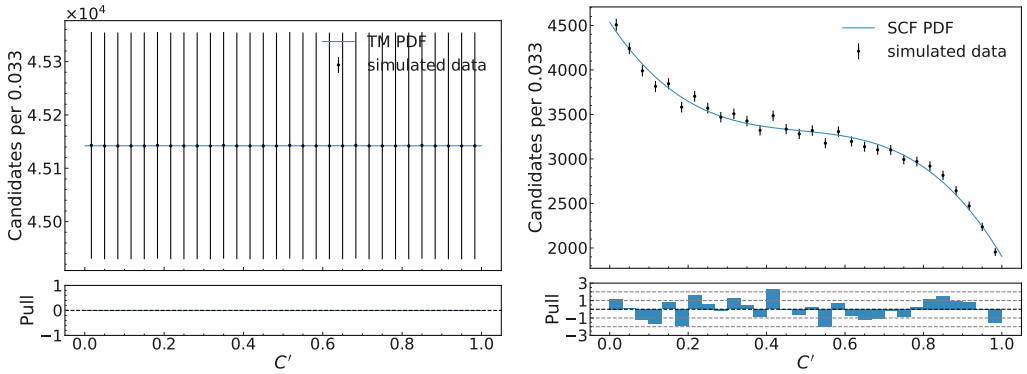

Figure 6.7: TM (left) and SCF (right) C' distributions. The fit shapes are overlaid.

6.2.2 Charmed Resonance ΔE PDF

The ΔE distributions are modeled with a double-sided Crystal Ball function and are shown in Figure 6.9.

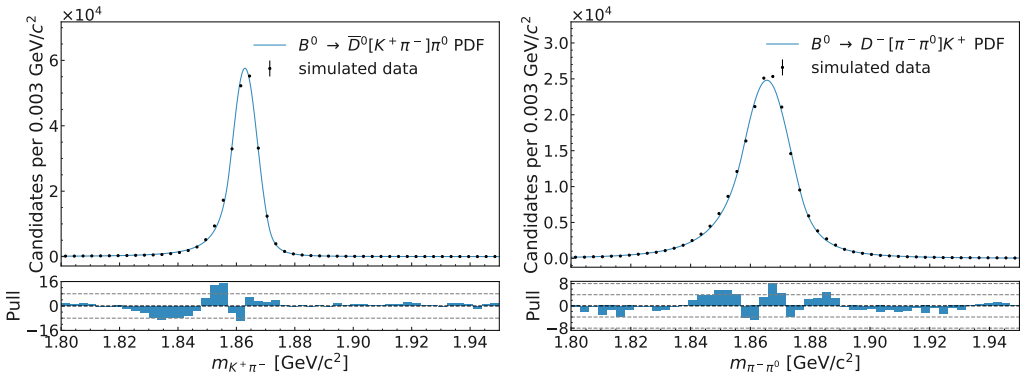

Figure 6.8: $m_{K^+\pi^-}$ distribution of $B^0 \to \overline{D}^0[K^+\pi^-]\pi^0$ (left) and $m_{\pi^-\pi^0}$ distribution of $B^0 \to D^-[\pi^-\pi^0]K^+$ (right). The mass-dependency is modeled with a double-sided Crystal Ball function and overlaid as the blue line.

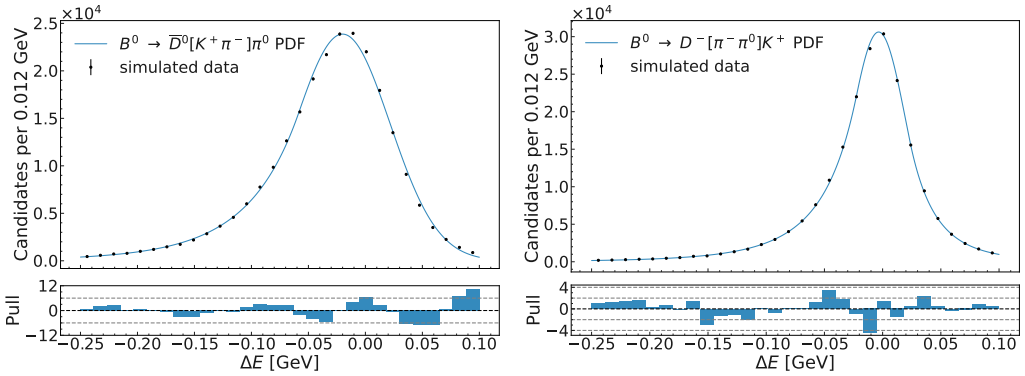

Figure 6.9: ΔE distributions of $B^0 \to \overline{D}^0[K^+\pi^-]\pi^0$ (left) and $B^0 \to D^-[\pi^-\pi^0]K^+$ (right). The fits of a double-sided Crystal Ball function are overlaid.

6.2.3 Charmed Resonance C' PDF

The C' PDF is described by a second order Chebyshev polynomial and can be seen in Figure 6.10.

6.3 The Continuum Model

The largest background component originates from continuum events. These events can also form charmless resonances like $K^*(892)$ or $\rho(770)^-$ and therefore a dedicated model for the Dalitz plot distributions is required.

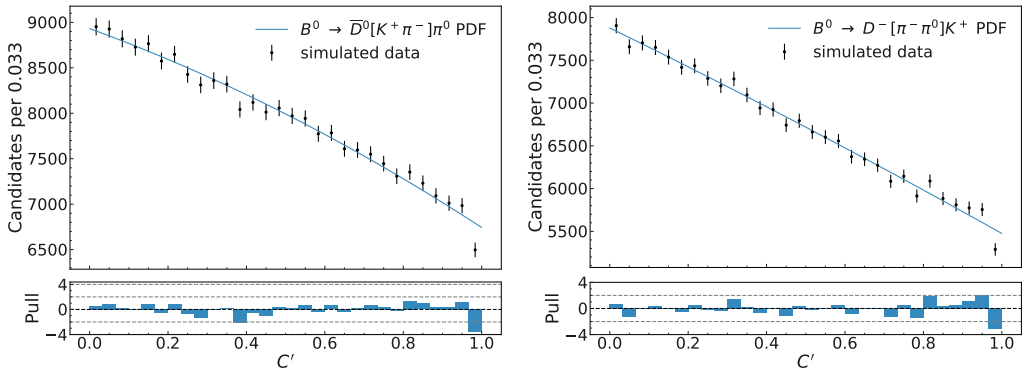

Figure 6.10: C' distributions of $B^0 \to \overline{D}^0[K^+\pi^-]\pi^0$ (left) and $B^0 \to D^-[\pi^-\pi^0]K^+$ (right). The fits of a second oder Chebyshev polynomial are overlaid.

6.3.1 Continuum Dalitz PDF

Since it is known that our simulations of continuum background are poor, the continuum model is extracted from real data. We extract the continuum shape from a data M_{bc} sideband defined as $5.24\,\mathrm{GeV}/c^2 < M_{\mathrm{bc}} < 5.27\,\mathrm{GeV}/c^2$. The sideband range is chosen, because $B\overline{B}$ events peak at the B-meson mass ($\sim 5.28\,\mathrm{GeV}/c^2$) in M_{bc}, i.e. we remove $B\overline{B}$ events and are left with a continuum dominated sample. The composition of this sideband in simulated data is shown in Figure 6.11. A small pollution from $B\overline{B}$ remains. To get

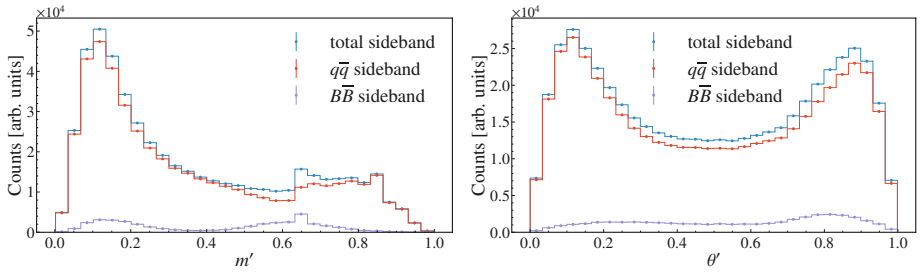

Figure 6.11: Sample composition of generically simulated events in the $5.24 < M_{\mathrm{bc}} < 5.27\,\mathrm{GeV}/c^2$ sideband in m' (left) and θ' (right).

a pure continuum sample we subtract $B\overline{B}$ component as predicted in simulations. The comparison of the continuum distributions of the M_{bc} sideband and M_{bc} signal region in m' and θ' after the $B\overline{B}$ subtraction can be seen in Figure 6.12. The discrepancies stem from the different kinematics in the sideband and signal region. Hence, we reweight the sideband to match the signal region, simply by dividing the histograms.

The continuum Dalitz shape is then implemented as a spline-interpolation of the resulting 2D-histogram. Projections in m' and θ' are shown in Figure 6.13.

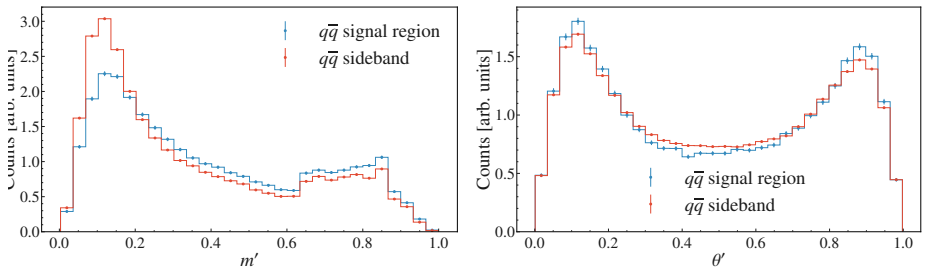

Figure 6.12: Comparison of M_{bc} sidband and signal region distributions of continuum events in m' (left) and θ' (right).

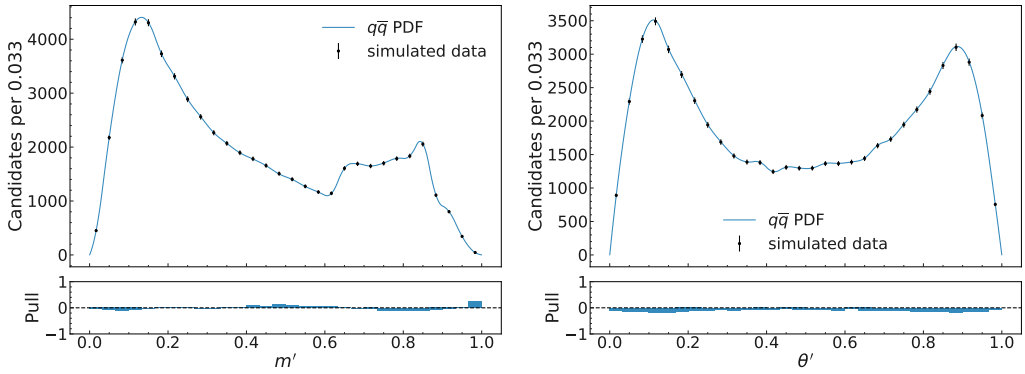

Figure 6.13: Continuum m' (left) and θ' (right) distributions extracted from an M_{bc} sideband. The remaining $B\overline{B}$ component was subtracted. Following, it was reweighted to match the signal region.

6.3.2 Continuum ΔE and C' PDFs

The continuum shapes in ΔE and C' are described with an exponential function

$$f(x;c) = exp(c \cdot x) \tag{6.17}$$

and are shown in Figure 6.14

6.4 The $B\overline{B}$ Model

As summarized in Table 5.4 multiple other $B\overline{B}$ decays can be wrongly reconstructed and end in our final dataset, due to random combinations of tracks and clusters from signal and tag side. We group them in two classes. The first contains $b \to c$ transitions referred to as $B \to$ charm background. The second group does not contain any c quark in the final state particles and is hence named $B \to$ charmless background.

The largest contribution in the $B \to$ charm component are partially reconstructed $B^- \to D^0[K^-\pi^+]\rho^-[\pi^-\pi^0]$ decays, where the π^- from the ρ^- is not reconstructed. Hence,

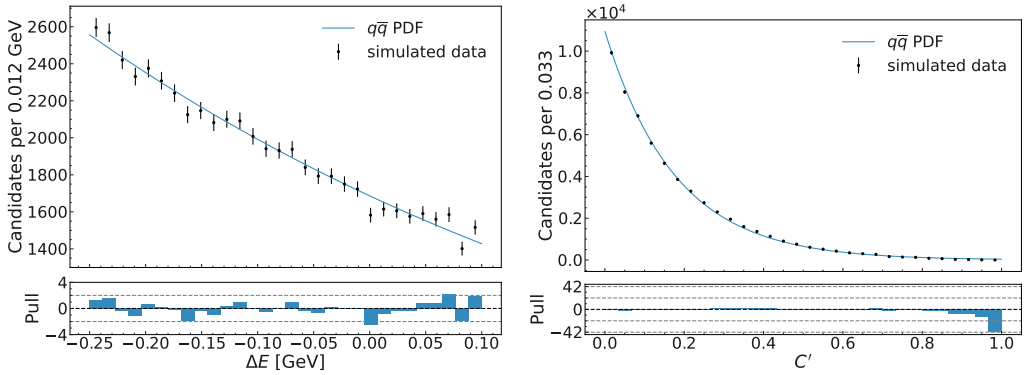

Figure 6.14: Continuum ΔE (left) and C' (right) distributions. Fits of exponential functions are overlaid.

we further split the $B \to$ charm background into a $B^- \to D^0[K^-\pi^+]\rho^-[\pi^-\pi^0]$ component and the rest, which we refer to as $B \to$ charm (w/o $B^- \to D^0\rho^-$).

6.4.1 $B\overline{B}$ Dalitz PDF

Like the non-interfering charm resonances the $B^- \to D^0\rho^-$ decay peaks at the D^0-mass in $m_{K^+\pi^-}$ and is similarly modeled with a double-sided Crystal Ball function as lineshape, which can be seen in Figure 6.15.

The $B \to$ charm (w/o $B^- \to D^0\rho^-$) and $B \to$ charmless Dalitz models are extracted as 2D-histograms from generically simulated events and implemented as spline-interpolations. They can be seen in Figure 6.16 and Figure 6.17

6.4.2 $B\overline{B}$ ΔE PDF

The ΔE distributions exhibit complex shapes which are difficult to model with analytical functions. Therefore, they are modeled with a so-called kernel density estimation (KDE). This is a way of modeling arbitrary shapes by a superposition of gaussian functions for each data point [63]. The shapes are extracted from simulated data and are shown in Figure 6.18.

6.4.3 $B\overline{B}$ C' PDF

The C' distributions of the $B\overline{B}$ backgrounds are modeled with a first oder Chebyshev polynomial and are shown in Figure 6.19

6.5 Summary of the Fit Model

All used fit shapes are summarized in Table 6.1.

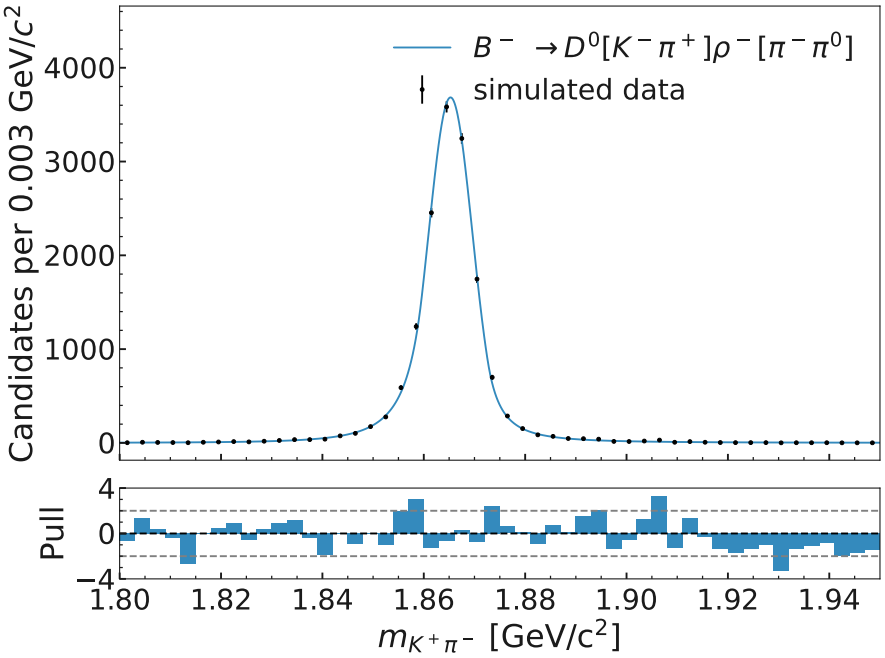

Figure 6.15: $B^- \to D^0[K^-\pi^+]\rho^-[\pi^0\pi^-]$ $m_{K^+\pi^-}$ distribution. A fit of a double-sided Crystal Ball function is overlaid.

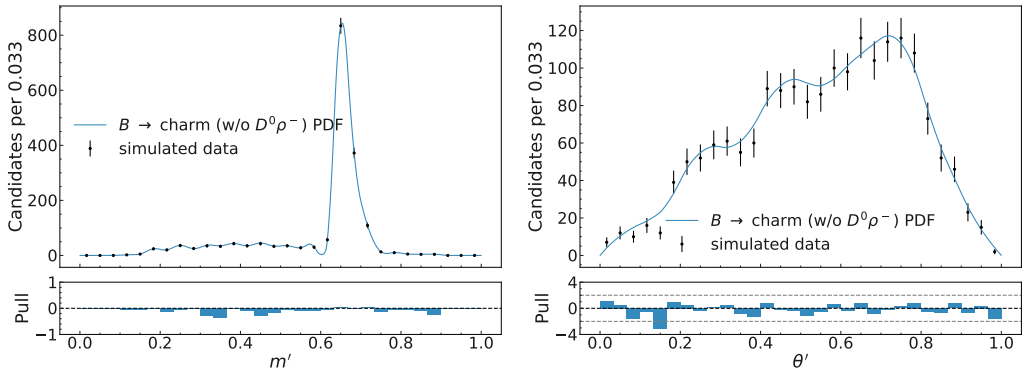

Figure 6.16: $B \to$ charm (w/o $B^- \to D^0\rho^-$) m' (left) and θ' (right) distributions. A spline-interpolation is overlaid.

[1]double-sided Crystal Ball function
[2]Chebyshev polynomial
[3]Histogram
[4]Exponential function
[5]Kernel density estimation

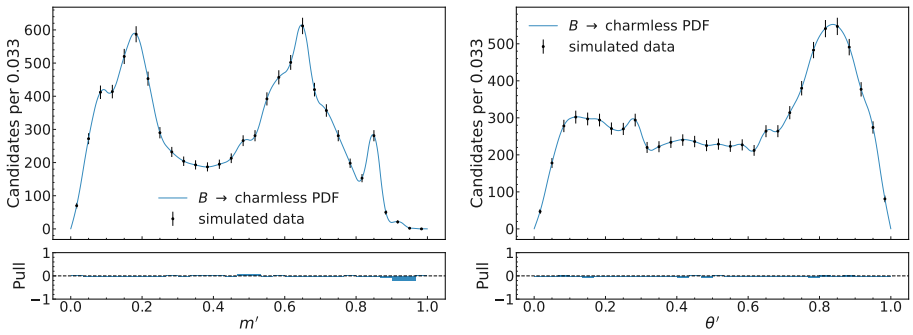

Figure 6.17: $B \to$ charmless m' (left) and θ' (right) distributions. A spline-interpolation is overlaid.

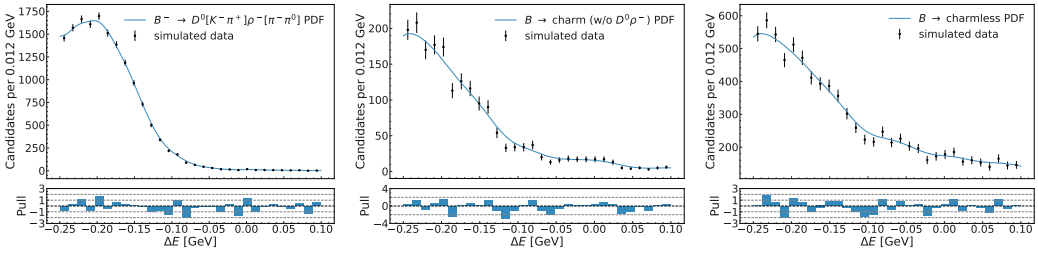

Figure 6.18: ΔE distributions of $B^- \to D^0[K^-\pi^+]\rho^-[\pi^0\pi^-]$ (left), $B \to$ charm (w/o $B^- \to D^0\rho^-$) (middle) and $B \to$ charmless (right) decays. The respective fit projections of the KDE are overlaid.

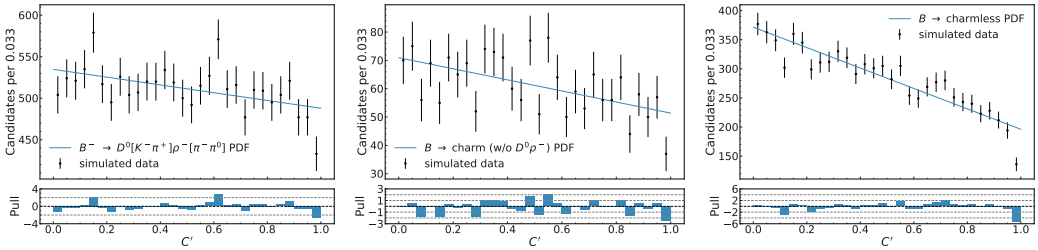

Figure 6.19: C' distributions of $B^- \to D^0[K^-\pi^+]\rho^-[\pi^0\pi^-]$ (left), $B \to$ charm (w/o $B^- \to D^0\rho^-$) (middle) and $B \to$ charmless (right) decays. Fit projections of first oder Chebyshev polynomials are overlaid.

The likelihood we use is

$$\mathcal{L} = \prod_i^N \frac{\hat{\mathcal{I}}_i}{\hat{N}} \tag{6.18}$$

where the product runs over all recorded events N. $\hat{\mathcal{I}}_i$ is the expected intensity of event i and $\hat{N}$ the expected number of events. I.e. the likelihood is given by the product over all recorded events of the expected intensity density. Since the expected number of events $\hat{N}$

Table 6.1: Summary of the used fit shapes for each component.

Component	Dalitz Plot	ΔE	C'
TM	Amplitude Model	Correlated ds CB[1]	flat line
SCF	Amplitude Model	CB + 1. Cheby[2]	3. Cheby
$B^0 \to \overline{D}^0[K^+\pi^-]\pi^0$	incoherent ds CB	ds CB	2. Cheby
$B^0 \to D^-[\pi^-\pi^0]K^+$	incoherent ds CB	ds CB	2. Cheby
continuum	Hist[3]	Exp[4]	Exp
$B^- \to D^0[K^-\pi^+]\rho^-[\pi^-\pi^0]$	incoherent ds CB	KDE[5]	1. Cheby
$B \to$ charm (w/o $B^- \to D^0\rho^-$)	Hist	KDE	1. Cheby
$B \to$ charmless	Hist	KDE	1. Cheby

is not know, we perform an extended maximum likelihood fit, i.e. we add a Poisson term and the extended likelihood function reads

$$\mathcal{L}_{ext} = \frac{\hat{N}^N \cdot e^{-\hat{N}}}{N!} \prod_i^N \frac{\hat{\mathcal{I}}_i}{\hat{N}}. \tag{6.19}$$

Since $\prod_i^N \frac{1}{\hat{N}} = \frac{1}{\hat{N}^N}$ it cancels with the $\hat{N}^N$ part from the Poisson term. $\frac{1}{N!}$ is a constant, hence does not impact the minimization and is dropped. The extended maximum likelihood function then becomes

$$\mathcal{L}_{ext} = e^{-\hat{N}} \prod_i^N \hat{\mathcal{I}}_i. \tag{6.20}$$

The expected intensity is the expected number of events differential in the phase space, i.e.

$$\hat{\mathcal{I}} = \frac{d\hat{N}}{dm' d\theta' d\Delta E dC'} \tag{6.21}$$

We perform the fit simultaneously to the $B^0 \to K^+\pi^-\pi^0$ and $\overline{B}^0 \to K^-\pi^+\pi^0$ sample. The expected $B^0 \to K^+\pi^-\pi^0$ and $\overline{B}^0 \to K^-\pi^+\pi^0$ intensities are annotated with a superscript $+$ or $-$, respectively, as given by the charge of the kaon. The expected $B^0 \to K^+\pi^-\pi^0$

intensity for an event i reads as follows

$$\begin{aligned}
\hat{\mathcal{I}}_i^+ =& \mathcal{B}_{\text{inclusive}} \cdot \overline{\eta} \cdot \frac{N_{B\overline{B}}}{2}(1 - \mathcal{A}^{CP}_{\text{inclusive}})[(1 - \overline{f}_{\text{SCF}})\mathcal{P}^+_{\text{TM},i} + \overline{f}_{\text{SCF}}\mathcal{P}^+_{\text{SCF},i}]+ \\
&+\frac{N_{B^0 \to \overline{D}^0[K^+\pi^-]\pi^0}}{2}(1 - \mathcal{A}^{CP}_{B^0 \to \overline{D}^0[K^+\pi^-]\pi^0})\mathcal{P}_{B^0 \to \overline{D}^0[K^+\pi^-]\pi^0,i}+ \\
&+\frac{N_{B^0 \to D^-[\pi^-\pi^0]K^+}}{2}(1 - \mathcal{A}^{CP}_{B^0 \to D^-[\pi^-\pi^0]K^+})\mathcal{P}_{B^0 \to D^-[\pi^-\pi^0]K^+,i}+ \\
&+\frac{N_{q\overline{q}}}{2}(1 - \mathcal{A}^{CP}_{q\overline{q}})\mathcal{P}_{q\overline{q},i}+ \\
&+\frac{N_{\text{charm}}}{2}(1 - \mathcal{A}^{CP}_{\text{charm}})[f^+_{B^+ \to \overline{D}^0\rho^+}\mathcal{P}_{B^+ \to \overline{D}^0\rho^+,i}+ \\
&\qquad + (1 - f^+_{B^+ \to \overline{D}^0\rho^+})\mathcal{P}_{B \to \text{charm (w/o } B^+ \to \overline{D}^0\rho^+),i}]+ \\
&+\frac{N_{\text{charmless}}}{2}(1 - \mathcal{A}^{CP}_{\text{charmless}})\mathcal{P}_{B \to \text{charmless},i}.
\end{aligned} \tag{6.22}$$

Accordingly the expected $\overline{B}^0 \to K^-\pi^+\pi^0$ intensity for an event i is given as

$$\begin{aligned}
\hat{\mathcal{I}}_i^- =& \mathcal{B}_{\text{inclusive}} \cdot \overline{\eta} \cdot \frac{N_{B\overline{B}}}{2}(1 + \mathcal{A}^{CP}_{\text{inclusive}})[(1 - \overline{f}_{\text{SCF}})\mathcal{P}^-_{\text{TM},i} + \overline{f}_{\text{SCF}}\mathcal{P}^-_{\text{SCF},i}]+ \\
&+\frac{N_{\overline{B}^0 \to D^0[K^-\pi^+]\pi^0}}{2}(1 + \mathcal{A}^{CP}_{B^0 \to \overline{D}^0[K^+\pi^-]\pi^0})\mathcal{P}_{\overline{B}^0 \to D^0[K^-\pi^+]\pi^0,i}+ \\
&+\frac{N_{\overline{B}^0 \to D^+[\pi^+\pi^0]K^-}}{2}(1 + \mathcal{A}^{CP}_{B^0 \to D^-[\pi^-\pi^0]K^+})\mathcal{P}_{\overline{B}^0 \to D^+[\pi^+\pi^0]K^-,i}+ \\
&+\frac{N_{q\overline{q}}}{2}(1 + \mathcal{A}^{CP}_{q\overline{q}})\mathcal{P}_{q\overline{q},i}+ \\
&+\frac{N_{\text{charm}}}{2}(1 + \mathcal{A}^{CP}_{\text{charm}})[f^-_{B^- \to D^0\rho^-}\mathcal{P}_{B^- \to D^0\rho^-,i}+ \\
&\qquad + (1 - f^-_{B^- \to D^0\rho^-})\mathcal{P}_{B \to \text{charm (w/o } B^- \to D^0\rho^-),i}]+ \\
&+\frac{N_{\text{charmless}}}{2}(1 + \mathcal{A}^{CP}_{\text{charmless}})\mathcal{P}_{B \to \text{charmless},i},
\end{aligned} \tag{6.23}$$

where

- $\mathcal{B}_{\text{inclusive}}$ is the inclusive branching fraction,
- $\overline{\eta}$ is the acceptance or efficiency averaged over the Dalitz plane (see Eq. 3.26),
- $N_{B\overline{B}}$ is the total number of B decays,
- $\mathcal{A}^{CP}_{\text{inclusive}}$ is the inclusive *CP*-violating charge asymmetry (see Eq. 3.28),
- $\overline{f}_{\text{SCF}}$ is the self-cross-feed fraction averaged over the Dalitz plane (see Eq. 6.4),
- $f^+_{B^+ \to \overline{D}^0\rho^+}$ is the fraction of $B^+ \to \overline{D}^0\rho^+$ in $B \to$ charm in the + sample and vice versa for $f^-_{B^- \to D^0\rho^-}$,
- N_k is the yield of background component k

- $\mathcal{A}_k^{CP}$ is the *CP*-violating charge asymmetry of background component k
- and $\mathcal{P}_{k,i}$ is the PDF of component k evaluated at event i.

The extended likelihoods for the $B^0 \to K^+\pi^-\pi^0$ and $\overline{B}^0 \to K^-\pi^+\pi^0$ channel are given by

$$\mathcal{L}_{ext}^{+} = e^{-\hat{N}^+} \times \prod_i^{N^+} \hat{\mathcal{I}}_i^+ \tag{6.24}$$

and

$$\mathcal{L}_{ext}^{-} = e^{-\hat{N}^-} \times \prod_i^{N^-} \hat{\mathcal{I}}_i^- \tag{6.25}$$

Instead of maximizing the above likelihoods one typically minimizes the negative log-likelihood, i.e. $NLL^+ := -log({\mathcal{L}^+}_{ext})$ and $NLL^- := -log({\mathcal{L}^-}_{ext})$. Taking the logarithm has the advantage, that the product over the events becomes a sum over the events. Since most of the optimization algorithms are minimizers we take the negative of the log-likelihood. The function that is finally minimized is the sum of both likelihoods

$$NLL = NLL^+ + NLL^-. \tag{6.26}$$

In total the minimizer determines 44 floating parameters. They are summarized in Table 6.2.

Table 6.2: Summary of floating parameters in the final fit.

15 real parts of the amplitude couplings
14 imaginary parts of the amplitude couplings
$\mathcal{B}_{\text{inclusive}}$
$N_{B^0 \to \overline{D}^0[K^+\pi^-]\pi^0}$ and $\mathcal{A}^{CP}_{B^0 \to \overline{D}^0[K^+\pi^-]\pi^0}$
$N_{B^0 \to D^-[\pi^-\pi^0]K^+}$ and $\mathcal{A}^{CP}_{B^0 \to D^-[\pi^-\pi^0]K^+}$
$N_{q\overline{q}}$ and $\mathcal{A}^{CP}_{q\overline{q}}$
N_{charm} and $\mathcal{A}^{CP}_{\text{charm}}$
$f^+_{B^+ \to \overline{D}^0\rho^+}$ and $f^-_{B^- \to D^0\rho^-}$
$N_{\text{charmless}}$ and $\mathcal{A}^{CP}_{\text{charmless}}$
$q\overline{q}$ shape in ΔE and $q\overline{q}$ shape in C'

The most intuitive way of parameterizing the complex amplitude couplings c_i is in terms of a magnitude r_i and a phase ϕ_i, i.e. $c_i = r_i e^{i\phi_i}$. $r_i \in [0, \infty)$ and $\phi_i \in [0, 2\pi]$. Using this parametrization, a minimizing algorithm trying to find the best values of r_i and ϕ_i might run into problems if the best value of ϕ_i is close to the borders, because it doesn't necessarily understand ϕ_i is defined on a circle (i.e. $2\pi = 0$ or $360° = 0°$). Therefore, we parametrize $c_i = a_i + i \cdot b_i$ in terms of a real and imaginary part a_i and b_i, with a_i, $b_i \in (-\infty, \infty)$.

In order to improve the stability of the fit, we additionally constrain some floating parameters. We are using so-called Gaussian constraints. This means we add

$$\frac{(x - x_{\text{true}})^2}{2 \cdot \Delta x_{\text{true}}} \tag{6.27}$$

to the negative log-likelihood. x is the fit parameter, x_{true} is the "true" value as extracted from simulated data and Δx_{true} is the uncertainty on the "true" value, e.g. $\sqrt{x_{\text{true}}}$ for a yield. The idea is to constrain the value within its uncertainties and give the minimizing algorithm an additional handle. Such constraints are added for the yields of the charmed resonances, i.e. $N_{B^0 \to \overline{D}^0[K^+\pi^-]\pi^0}$ and $N_{B^0 \to D^-[\pi^-\pi^0]K^+}$ as they are small and signal like, and for the fractions $f^+_{B^+ \to \overline{D}^0\rho^+}$ and $f^-_{B^- \to D^0\rho^-}$.

7 Fit Validation

We perform several studies on simulated data to test the performance of the afore described fitting setup. The goal is to identify possible problems of the fitting procedure.

7.1 Fit on Simulated Data corresponding to $362\,\mathrm{fb}^{-1}$

Firstly, we run the fit on a sample of generic simulated data corresponding to the size of the real data sample. The signal component is modeled as described in Sec. 5.1.1, i.e. according to the *BABAR* model. This allows the comparison between the fit result and and the "true" values from our simulation. Fit projections in ΔE, C' and the square Dalitz variables are shown in Figures 7.1 and 7.2.

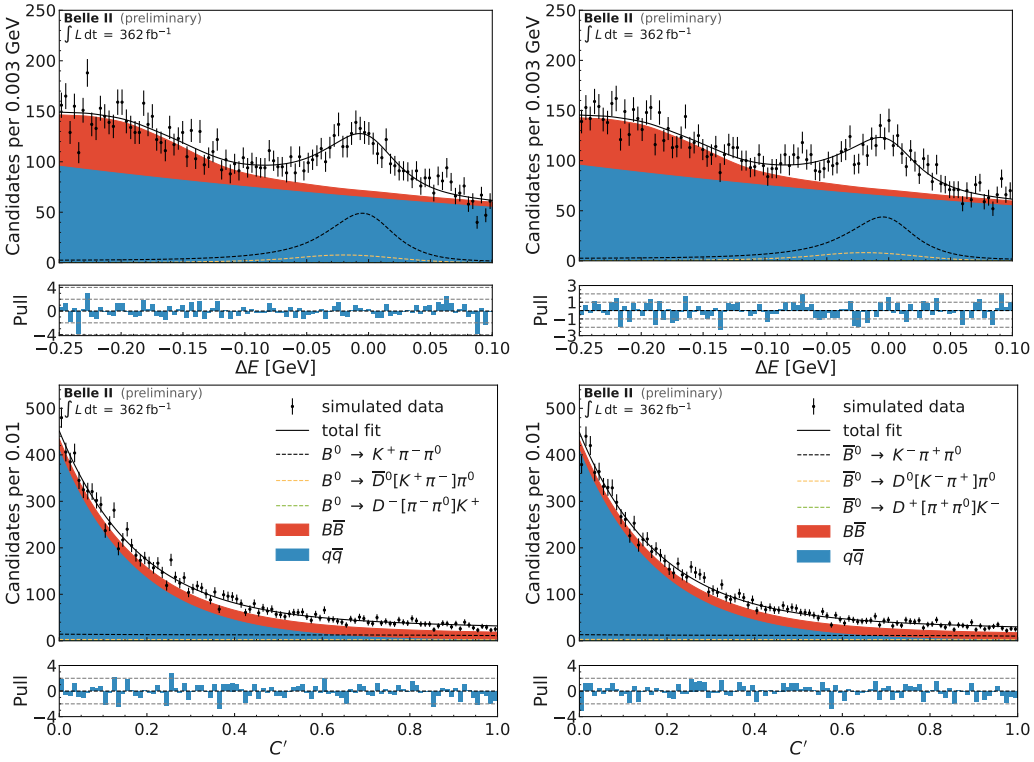

Figure 7.1: Distributions of ΔE (top) and C' (bottom) for $B^0 \to K^+\pi^-\pi^0$ (left) and $\overline{B}^0 \to K^-\pi^+\pi^0$ (right) decays in $362\,\mathrm{fb}^{-1}$ of simulated data. Fit projections are overlaid.

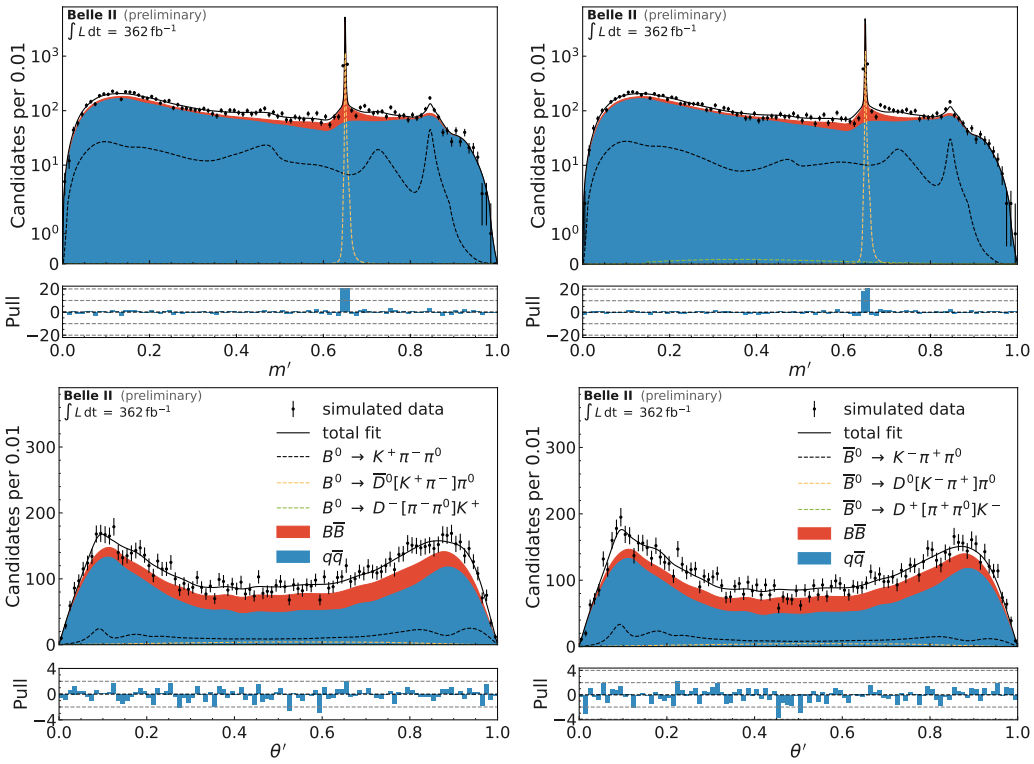

Figure 7.2: Distributions of m' (top) and θ' (bottom) for $B^0 \to K^+\pi^-\pi^0$ (left) and $\overline{B}^0 \to K^-\pi^+\pi^0$ (right) decays in $362\,\text{fb}^{-1}$ of simulated data. Fit projections are overlaid.

The ΔE distributions show a clean signal peak around zero. Underlying is the large flat continuum contribution. At lower ΔE values also a significant $B\overline{B}$ contribution can be seen, stemming from partially reconstructed events.

The m' distribution is dominated by the narrow $B^0 \to \overline{D}^0[K^+\pi^-]\pi^0$ events. In m' and θ' the signal component (black dashed line) nicely shows the complex intensity distribution.

Overall the the fit model describes the data well, as can be seen in the pull plots, where the pull is evaluated as

$$\text{pull} = \frac{\text{value data histogram} - \text{value fit model}}{\sqrt{\text{value data histogram}}} \tag{7.1}$$

The results of the fit are summarized in Table 7.1. We list the "fit" values with their uncertainties as determined by minimizing the negative log-likelihood. Additionally, we show the "true" values as given in our simulated data. In the last column we calculate the pull

$$\text{pull} = \frac{\text{fit value} - \text{true value}}{\text{fit uncertainty}} \tag{7.2}$$

which is the difference between fit value and true value normalized by the fit uncertainty.

Table 7.1: Summary of the fit results to one sample of simulated data corresponding to 362 fb^{-1}. A comparison to the "true" values as well the pull (normalized deviation from "true" value) is shown.

Wave	Parameter	Fit value			"True" value	Pull [σ]
$K^*(892)^+$	$\mathcal{B}$ [10^{-6}]	13.36	$\pm$	1.43	12.40	0.67
	$\mathcal{A}^{CP}$	-0.427	$\pm$	0.093	-0.308	-1.27
$K^*(892)^0$	$\mathcal{B}$ [10^{-6}]	4.06	$\pm$	0.49	5.05	-2.01
	$\mathcal{A}^{CP}$	-0.111	$\pm$	0.109	-0.149	0.35
$\rho(770)^-$	$\mathcal{B}$ [10^{-6}]	11.02	$\pm$	0.97	9.96	1.10
	$\mathcal{A}^{CP}$	0.140	$\pm$	0.076	0.196	-0.73
$(K\pi)_0^{*+}$	$\mathcal{B}$ [10^{-6}]	45.35	$\pm$	4.85	51.07	-1.18
	$\mathcal{A}^{CP}$	-0.074	$\pm$	0.104	0.075	-1.44
$(K\pi)_0^{*0}$	$\mathcal{B}$ [10^{-6}]	11.93	$\pm$	1.84	12.82	-0.48
	$\mathcal{A}^{CP}$	-0.385	$\pm$	0.132	-0.153	-1.76
$\rho(1450)^-$	$\mathcal{B}$ [10^{-6}]	4.60	$\pm$	1.03	3.54	1.02
	$\mathcal{A}^{CP}$	0.116	$\pm$	0.236	-0.091	0.88
$\rho(1700)^-$	$\mathcal{B}$ [10^{-6}]	1.91	$\pm$	0.74	0.96	1.29
	$\mathcal{A}^{CP}$	-0.126	$\pm$	0.386	-0.345	0.57
non-resonant	$\mathcal{B}$ [10^{-6}]	7.50	$\pm$	3.13	4.16	1.07
	$\mathcal{A}^{CP}$	-0.570	$\pm$	0.268	0.102	-2.51
	$\mathcal{B}_{\text{inclusive}}$ [10^{-6}]	35.74	$\pm$	1.51	35.23	0.34
	$\mathcal{A}^{CP}_{\text{inclusive}}$	-0.101	$\pm$	0.054	0.016	-2.17
	$\mathcal{A}^{CP}_{B^0 \to \overline{D}^0[K^+\pi^-]\pi^0}$	0.031	$\pm$	0.049	0.00	0.63
	$N_{B^0 \to \overline{D}^0[K^+\pi^-]\pi^0}$	520	$\pm$	17	496	1.41
	$\mathcal{A}^{CP}_{B^0 \to D^-[\pi^-\pi^0]K^+}$	1.145	$\pm$	1.4	-0.200	0.96
	$N_{B^0 \to D^-[\pi^-\pi^0]K^+}$	7	$\pm$	3	10	-1.00
	$\mathcal{A}^{CP}_{q\bar{q}}$	-0.001	$\pm$	0.010	-0.001	0.00
	$N_{q\bar{q}}$	14653	$\pm$	160	14533	0.75
	$\mathcal{A}^{CP}_{\text{charm}}$	-0.047	$\pm$	0.025	-0.027	-0.80
	N_{charm}	2130	$\pm$	54	2091	0.72
	$\mathcal{A}^{CP}_{\text{charmless}}$	-0.020	$\pm$	0.053	-0.048	0.53
	$N_{\text{charmless}}$	1890	$\pm$	120	2129	-1.99

Note: As we reconstruct the resonances only from specific sub-decays, e.g. $K^*(892)^0 \to K^+\pi^-$ but not from $K^*(892)^0 \to K^0\pi^0$, we rescaled the resonance branching fractions with the appropriate sub-branching fraction to get the correct "full" branching fraction. The scales are given by their weak isospin configurations and can be read off from Clebsch-Gordon tables, e.g. [64]. The scaling factors are: $K^*(892)^+ : 3/1$, $K^*(892)^0 : 3/2$, $\rho(770)^- : 1$, $(K\pi)_0^{*+} : 3/1$, $(K\pi)_0^{*0} : 3/2$, $\rho(1450)^- : 1$, $\rho(1700)^- : 1$, non-resonant : 1.

All fit values coincide with their "true" values within less then 3σ, which means we can reasonably well extract our physics parameters of interest. Whether some of the differences are systematic of just a statistical fluctuation is evaluated in 7.3.

7.2 Multiple Solutions

Given the high dimensionality of the fit, the negative log-likelihood may exhibit multiple local minima. Depending on the starting parameters the minimizing algorithm can end in such a local minimum. We want to evaluate how often the fit finds the global, i.e. the "best", minimum. Therefore, we perform 100 fit attempts where we randomize the real and complex parameters of the couplings between ± 1. A histogram of the determined minima is shown in Figure 7.3.

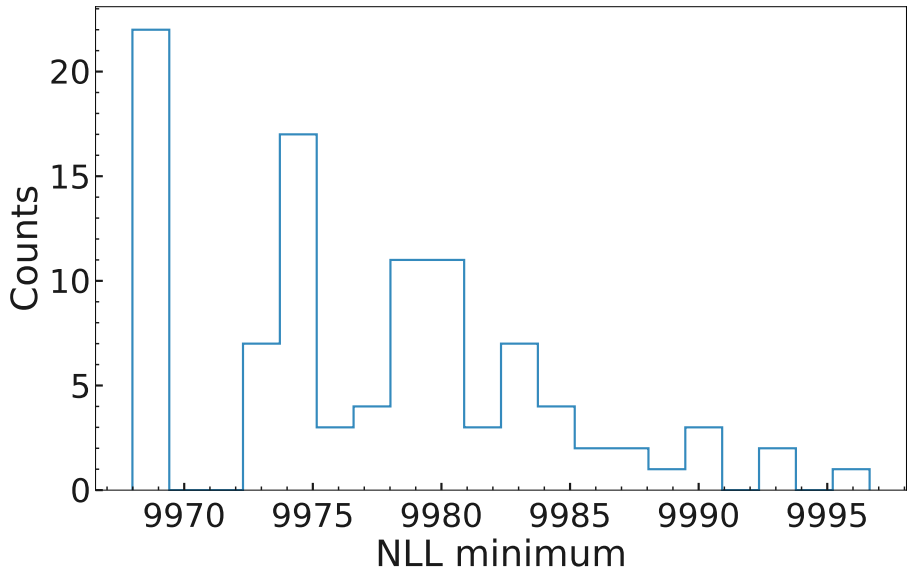

Figure 7.3: Distribution of the found minima of 100 fit attempts with randomized starting parameters of $362\,\mathrm{fb}^{-1}$ of simulated data.

As expected the minimization procedure can end in several minima, depending on the starting parameters. However, the best minimum (i.e. the global minimum) is found in more than 20% of the attempts. Concluding, when fitting the real data, we need to perform several fit attempts to find the global minimum.

7.3 Ensemble Tests

In order to examine the fitting procedure for internal problems we perform so-called *ensemble tests* (or *Toy MC* studies). We generate 200 datasets of the same size as the real data. The datasets are generated from the individual signal and background PDFs where we fluctuate the number of events according to Poisson statistic around the expected

number of events as determined in one fit to simulated data. We then fit each of these datasets. To avoid ending in a local minimum we set the starting parameters of the fit close to their true values. Subsequently, we determine the pull (or normalized residuals) as Eq. 7.2 for the physics parameters of interest. We then fit the pull distribution with a Gaussian function. If the estimator of our fit is unbiased the pull distribution follows a Gaussian distribution with mean zero and width one, i.e. a standard normal distribution. This means, that our fit determines on average the "correct" value. Potential deviations from the standard normal distribution reveal internal problems of the fit. A reason could be that the distributions of two components are too similar such that the fit cannot fully distinguish them.

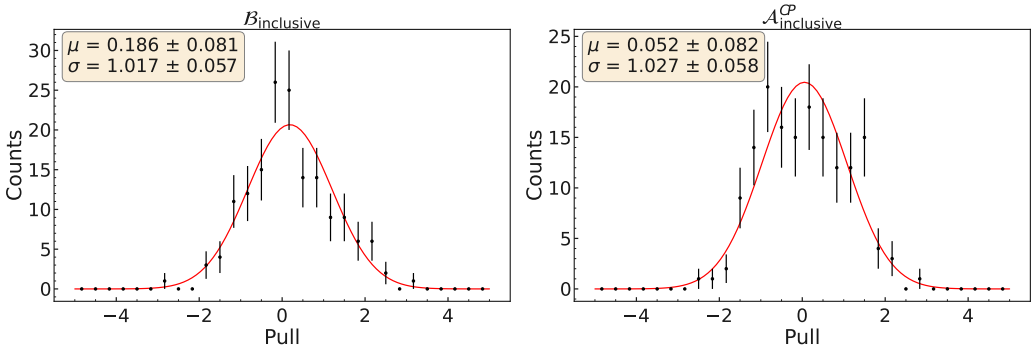

Figure 7.4: Pull distribution of 200 ensemble tests for the $\mathcal{B}_{\text{inclusive}}$ (left) and $\mathcal{A}^{CP}_{\text{inclusive}}$ (right). The fit of a Gaussian function is overlaid.

The resulting distributions for $\mathcal{B}_{\text{inclusive}}$ and $\mathcal{A}^{CP}_{\text{inclusive}}$ are shown in Figure 7.4. The distribution of $\mathcal{A}^{CP}_{\text{inclusive}}$ nicely follows the expected standard normal distribution. The width of the pull distribution of $\mathcal{B}_{\text{inclusive}}$ is compatible with one, however its mean is shifted by 18%. This means on average the fit overestimates the value of $\mathcal{B}_{\text{inclusive}}$ by 18% of its statistical uncertainty. We assign this value as systematic uncertainty.

The determined means and widths of the of the Gaussian fits for the branching fractions and direct *CP*-violating parameters of the resonances are shown in Figures 7.5 and 7.6. Also here, we observe several small biases up to 30% of the statistical uncertainty. The fit biases are assigned as systematic uncertainties.

Reasons for such biases could be problems distinguishing signal and background components. Additionally, we use histograms to model our backgrounds, acceptance and resolutions function. They are extracted from a finite sample of simulated data, i.e. the bins have a certain size and we average out smaller effects. Possible improvements to the fit could be to completely fix yields of small background components, however this comes again at the cost of a systematic uncertainty. Larger sets of simulated data would allow for more granular binning in the used histograms. Maybe statistical methods to subtract the backgrounds or analytical functions instead of histogram could be used in future iterations of this analysis. In any case, all of the observed biases are more than a factor two smaller than the expected statistical uncertainty and do not pose a limiting factor given the current amount of collected data.

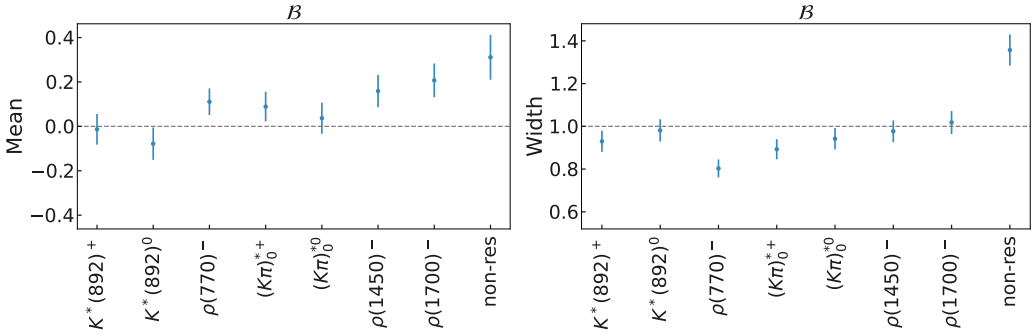

Figure 7.5: Means (left) and widths (right) of the pull distributions, determined by a Gaussian fit, of the resonance branching fractions.

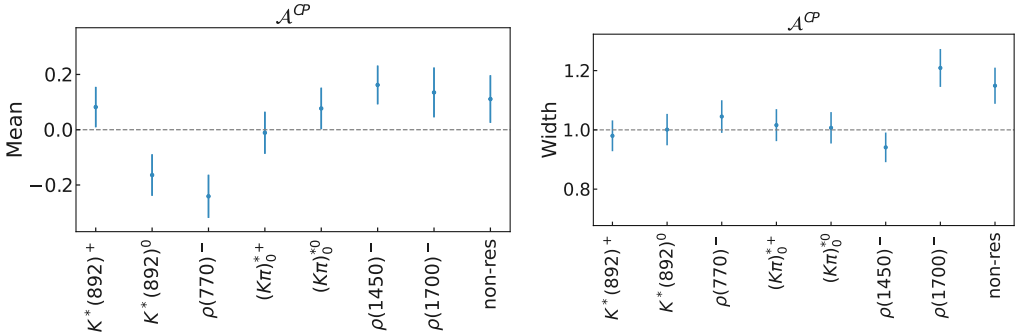

Figure 7.6: Means (left) and widths (right) of the pull distributions, determined by a Gaussian fit, of the resonance direct *CP*-violation parameters.

8 Data - Simulation Calibrations

As explained, the analysis is conducted "blind", meaning it is developed and validated on simulated data and sideband data only. Hence, we rely heavily on our simulations of the physics processes and the detector response. Given the complexity of the overall system these simulations are prone to mis-modeling and can show discrepancies to the real data. This chapter explains a few corrections we apply to mitigate these imperfections in our simulated data.

8.1 $B^- \to D^0[K^-\pi^+\pi^0]\pi^-$ control Mode Analysis

The $B^- \to D^0[K^-\pi^+\pi^0]\pi^-$ control channel has a similar topology as the $B^0 \to K^+\pi^-\pi^0$ signal channel, with a charged kaon, charged pion and a neutral pion emerging from a D^0 plus an additional high momentum charged pion. Its branching fraction is about 18 times higher than the $B^0 \to K^+\pi^-\pi^0$ signal channel, which allows to validate the analysis and extract correction factors on a more abundant sample. The reconstruction of the control mode is similar to the one used in the signal mode, with an additional requirement on the invariant $m_{K^+\pi^-}$ mass to be within $\pm 3\sigma$ around its nominal mass, where σ is the detector resolution, to reject a large majority of combinatorial background.

8.1.1 Determination of Data - Simulation Correction Factors

The shapes of the fit models of the signal component in ΔE and C' are fixed to values extracted from fits to large samples of simulated data. Due to possible differences between real data and simulated data we extract three correction factors from the $B^- \to D^0[K^-\pi^+\pi^0]\pi^-$ channel. Compared to simulated data, in the fit in real data, we allow for a shift Δ_μ of the ΔE peak position as well as a scale factor Δ_σ of the width. For the C' shape we extract a tilt factor Δ_t. They are applied as follows

$$\begin{aligned} &\text{simulated data} \to \text{real data} \\ &\mu \to \mu + \Delta_\mu \quad (\Delta E) \\ &\sigma \to \sigma \cdot \Delta_\sigma \quad (\Delta E) \\ &0 \to 0 + \Delta_t \quad (C'). \end{aligned}$$

The shape of ΔE is mainly determined by the kinematics of the neutral pion which is different in the $B^0 \to K^+\pi^-\pi^0$ and $B^- \to D^0[K^-\pi^+\pi^0]\pi^-$ channel. The π^0 in the $B^0 \to K^+\pi^-\pi^0$ channel has higher momentum since it is emerging directly from the B^0. The momentum of the π^0 in the $B^- \to D^0[K^-\pi^+\pi^0]\pi^-$ channel is shifted to lower momenta, since it is coming from the D^0. To account for this kinematical difference we reweight

the π^0 momentum of the control channel to match the signal channel. The corresponding plot is shown in Figure 8.1. The effect of the reweighting on the ΔE shape is shown in

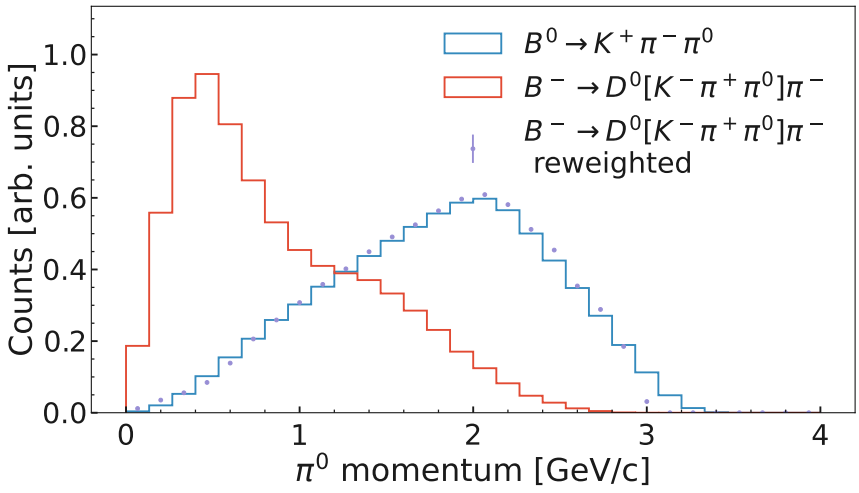

Figure 8.1: Comparison of the π^0 momentum in the $B^0 \to K^+\pi^-\pi^0$ channel (blue) and the $B^- \to D^0[K^-\pi^+\pi^0]\pi^-$ channel (red). To have a more close comparison, we reweight the π^0 momentum in the control channel to match the signal channel (purple).

Figure 8.2. After the reweighting the histograms in ΔE are a lot more similar. A small difference remains due to other kinematics in the control channel, which is a four body decay compared to the three body decay in the signal channel.

In the fit of the control channel we use similar shapes as in the signal channel (i.e. Crystal Ball functions or Chebyshev polynomials). We then extract the shape parameters from simulated data. Subsequently, we fit real data, with the shape parameters fixed and allow the correction factors Δ_μ, Δ_σ and Δ_t to float. Fit projections to the $362\,\text{fb}^{-1}$ of real data are shown in Figure 8.3. The results of the fit are summarized in Table 8.1.

Table 8.1: Fit results of the correction factors and branching fraction of $B^- \to D^0[K^-\pi^+\pi^0]\pi^-$ decays in LS1 data, along with the current PDG branching fraction. Uncertainties are statistical only.

Parameter	Fit result
Δ_μ	$(-0.36 \pm 0.85)\,\text{MeV}$
Δ_σ	0.99 ± 0.04
Δ_t	-0.052 ± 0.053
$\mathcal{B}_{fit}$	$(6.56 \pm 0.13) \times 10^{-3}$
$\mathcal{B}_{PDG}$	$(6.64 \pm 0.31) \times 10^{-3}$

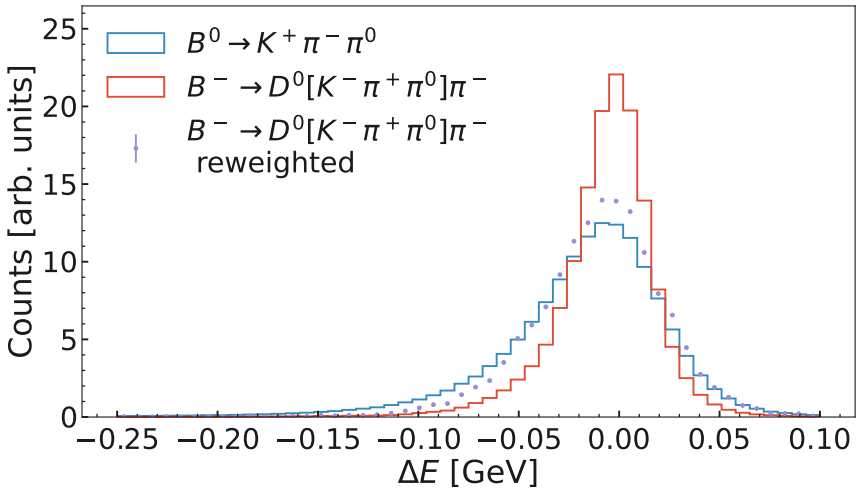

Figure 8.2: Comparison of the ΔE shape in the $B^0 \to K^+\pi^-\pi^0$ channel (blue) and the $B^- \to D^0[K^-\pi^+\pi^0]\pi^-$ channel (red). The purple dots with errorbars show the shape of ΔE with the reweighted π^0 momentum.

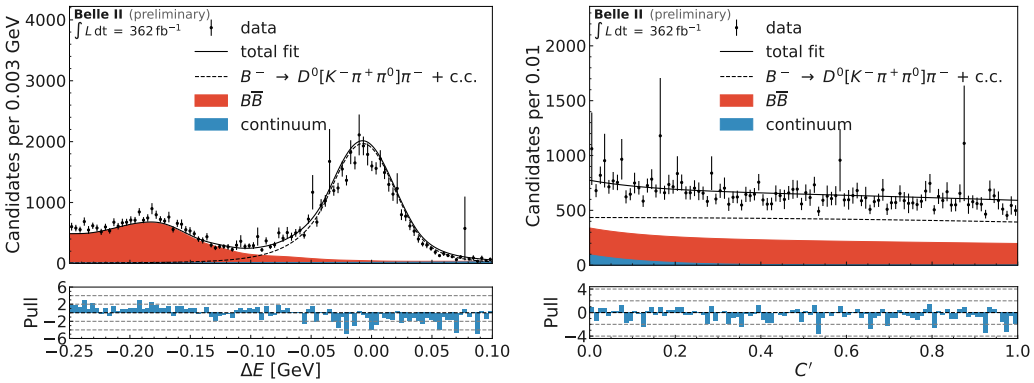

Figure 8.3: ΔE (left) and C' (right) distributions of $B^- \to D^0[K^-\pi^+\pi^0]\pi^-$ decays. Fit projections are overlaid.

We observe a small shift of $-0.36\,\text{MeV}$ of the ΔE peak and the width scaling factor compatible with 1 in real data compared to simulated data. In C' we extract a tilt of -0.052. The determined branching fraction is compatible with known determinations [15]. We include the determined correction factors into our likelihood functions as nuisance parameters. We implement them with a Gaussian constraint (see Eq. 6.27).

8.1.2 Determination of the Continuum Suppression Efficiency

The continuum suppression GBDT is trained on simulated data. Due to imperfections in our simulations, the efficiency of the GBDT might be different in simulated data and real

data. We use the $B^- \to D^0[K^-\pi^+\pi^0]\pi^-$ channel to deduce the efficiency ratio between real data and simulated data. To extract the efficiency in each sample, we split it into two disjoint samples. One passing the criteria on the GBDT and one failing it. We then perform a fit to the unbinned distributions of ΔE and C' simultaneously to both samples to extract the efficiency

$$\varepsilon_{CS} = \frac{\text{passed events}}{\text{passed events} + \text{failed events}}. \tag{8.1}$$

Again, the fit shapes are similar to the ones used in the $B^0 \to K^+\pi^-\pi^0$ channel. The fit projections for simulated data and in real data are shown in Figure 8.4 and Figure 8.5.

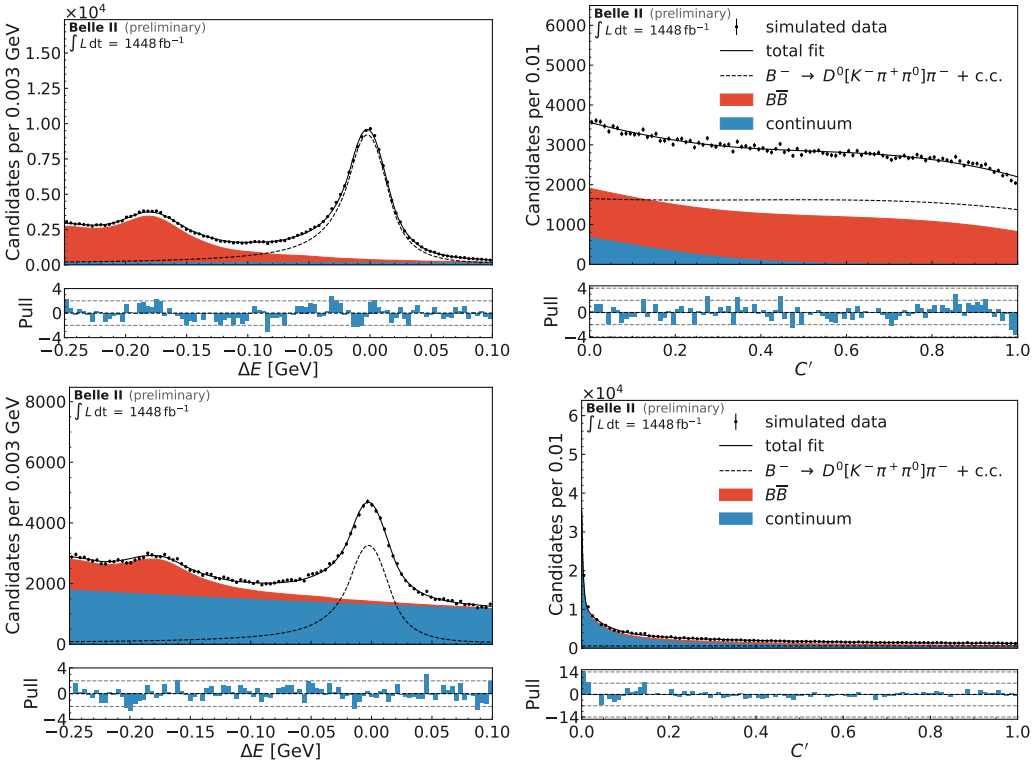

Figure 8.4: ΔE (left) and C' (right) distributions of $B^- \to D^0[K^-\pi^+\pi^0]\pi^-$ simulated events passing (top) and failing (bottom) the continuum suppression requirement. Fit projections are overlaid.

The results of fits to simulated data and real data are summarized in Table 8.2. The ratio of the efficiencies in simulations and data is 0.9841 ± 0.0048, which is not compatible with 1. We scale our determined branching fractions by 0.98 and assign 0.5% as a systematic uncertainty.

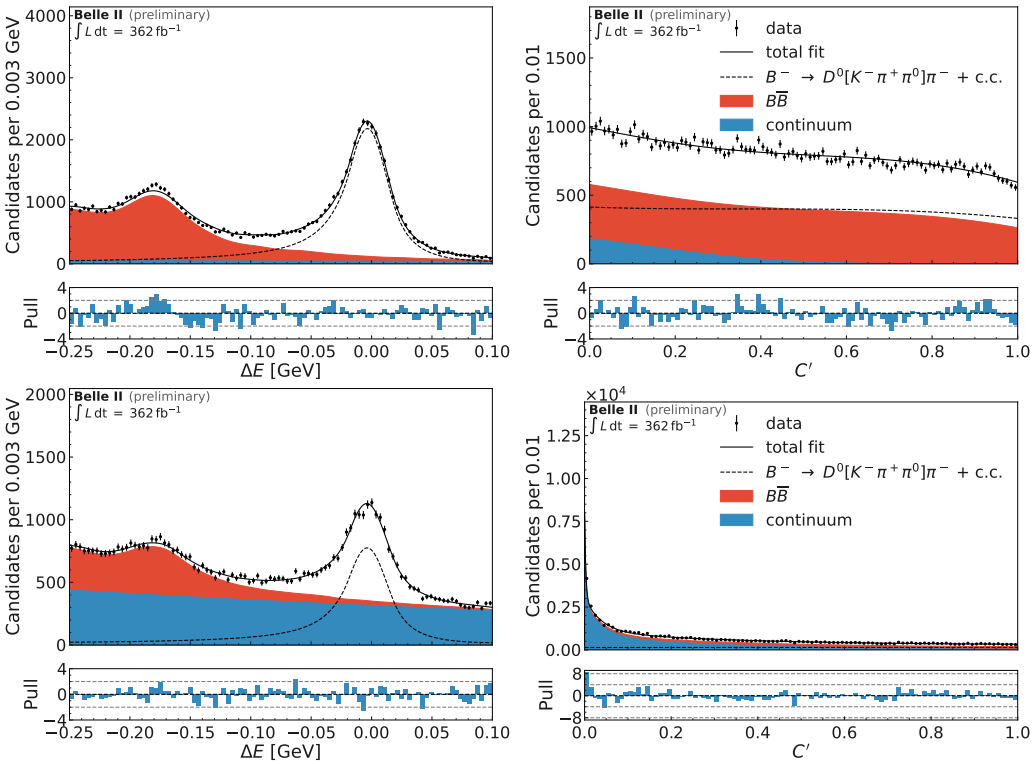

Figure 8.5: ΔE (left) and C' (right) distributions of $B^- \to D^0[K^-\pi^+\pi^0]\pi^-$ real events passing (top) and failing (bottom) the continuum suppression requirement. Fit projections are overlaid.

Table 8.2: Efficiency of the continuum suppression requirement extracted in simulated data and real data.

	efficiency
simulated data	$(74.37 \pm 0.16)\%$
real data	$(73.26 \pm 0.32)\%$
ratio	0.9850 ± 0.0047

8.2 Particle Identification (PID) Corrections

PID information plays an essential role in the differentiation of charged particles. Imposing requirements on the PID information helps to suppress background from mis-identified particles and purifies the data sample. As stated in Table 5.2 we require the global kaon/pion ID to be larger than 0.1 for the charged kaons/pions and the binary kaon ID to be larger than 0.96 for the kaon candidates. The PID combines information from several sub-detectors and is heavily dependent on the momentum and polar angle of the corresponding track. Both are prone to mis-modeling in simulated data compared to real

data and thus yield different efficiencies. To correct the efficiency differences the so called `Systematics Correction Framework` was developed for Belle II [65]. It uses control modes where the signal tracks can be easily determined without any knowledge on the PID. The $D^{*+} \to D^0[K^+\pi^-]\pi^+$ and $K^0_S \to \pi^+\pi^-$ channels are used for the kaon and pion ID, respectively. A fit of invariant mass distributions in these channels allows the extraction of sWeights [66] to derive "background-free" distributions of PID, track momentum and polar angle. This is done with the LS1 dataset corresponding to a luminosity of $362\,\mathrm{fb}^{-1}$ and simulated data of four times this size. We then compare the selection efficiencies for the tracks in bins of the track momentum and polar angle. The efficiency ratios for our PID requirements are shown in the Appendix in Figures A.5, A.6 and A.7. Depending on the corresponding bin we deduce weights for the simulated data. A comparison of the original and reweighted distributions of the fit variables for generic simulated data is shown in Figure 8.6.

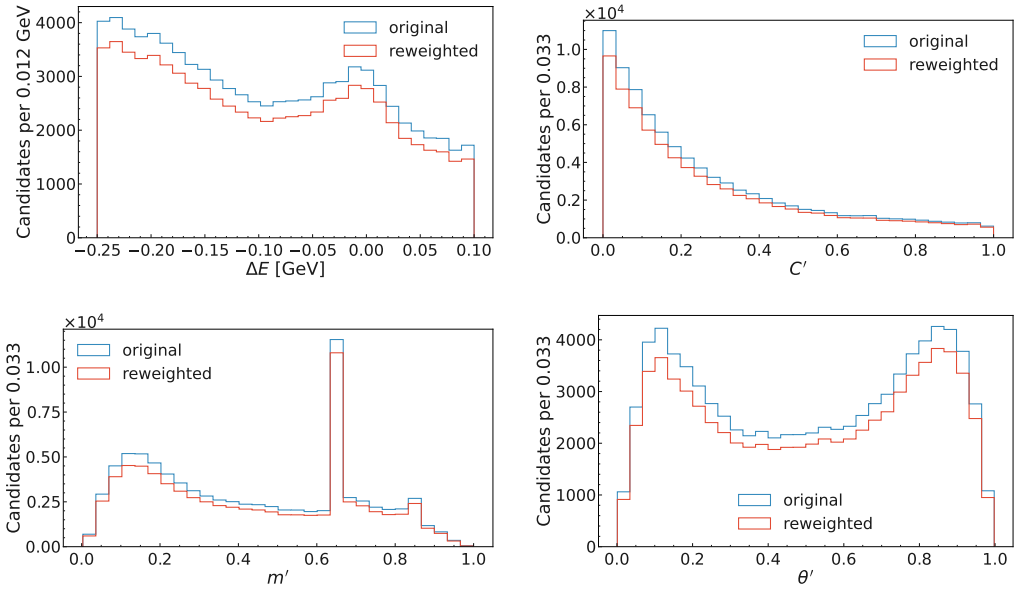

Figure 8.6: Effect of the PID weights applied on generic simulated data for the four fit variables, ΔE (top left), C' (top right), m' (bottom left) and θ' (bottom right).

The mean efficiency ratio and its error calculated over a large sample of signal events simulated uniformly in the Dalitz plane are $93.4\% \pm 0.8\%$.

8.3 π^0 Corrections

The requirements on our π^0 candidate help to suppress background from fake π^0, e.g. where a wrong photon is used in the reconstruction. Due to mis-modeling of ECL variables in our simulated data compared to real data, the efficiencies can be different. To adjust for these differences, weights are deduced in bins of the π^0 momentum and helicity angle

$\cos(\theta)$. The weights are provided by the Belle II performance group. They are extracted from $D^0 \to K^-\pi^+\pi^0$ and $D^0 \to K^-\pi^+$ decays. The efficiency ratio between real data and simulated data (i.e. the weights) is calculated as follows

$$\frac{\epsilon_{\text{real data}}(\pi^0)}{\epsilon_{\text{simulated data}}(\pi^0)} = \frac{N_{\text{real data}}(D^0 \to K^-\pi^+\pi^0)/N_{\text{simulated data}}(D^0 \to K^-\pi^+\pi^0)}{N_{\text{real data}}(D^0 \to K^-\pi^+)/N_{\text{simulated data}}(D^0 \to K^-\pi^+)}, \tag{8.2}$$

where N is the number of reconstructed signal events. N is determined in a fit to the invariant mass distributions of the D^0. The efficiency ratios for our π^0 selection is shown in the Appendix in Figure A.8. A comparison of the effect of the π^0 weights on a sample of generic simulated events is shown in Figure 8.7.

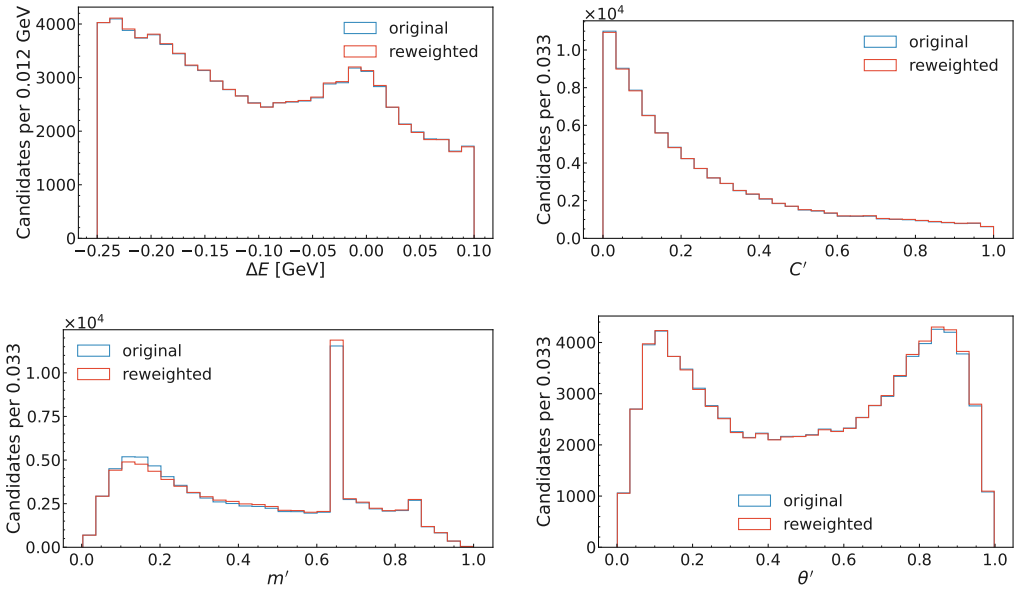

Figure 8.7: Effect of the π^0 weights applied on generic simulated data for the four fit variables, ΔE (top left), C' (top right), m' (bottom left) and θ' (bottom right).

The mean efficiency ratio and its error calculated over a large sample of signal events simulated uniformly in the Dalitz plane are $103.2\% \pm 4.1\%$.

9 Fit on $362\,\mathrm{fb}^{-1}$ of Belle II data

We run the afore described analysis on the full LS1 Belle II dataset. After reconstructing the events and applying all selection requirements, including the continuum suppression GBDT and the single candidate selection the final $B^0 \to K^+\pi^-\pi^0$ dataset contains 19361 events. We perform 40 fits with randomized starting parameters. The best minimum is found in 20% of the fits. All other minima are found less frequently. The obtained values for the best solution are listed in Table 9.1. We measure an average acceptance/efficiency (see Eq. 3.26) of 14.3%, resulting in an error of $\pm 3.28 \times 10^{-6}$ on the inclusive branching fraction, while *BABAR* measured $\pm 1.0 \times 10^{-6}$ [8]. Other fit solutions yield higher efficiencies of up to 34.7% where the uncertainty on the inclusive branching fraction is $\pm 1.36 \times 10^{-6}$. Consequently, the efficiency is heavily dependent on the resonance couplings. To get some feeling on the variation of the physics parameters depending on the minimum of the negative log-likelihood we calculate the ratios between the global minimum (solution 1) and the second lowest minimum (solution 2), e.g.

$$\text{ratio} = \frac{\mathcal{B}_{\text{inclusive}}(\text{NLL(solution 1)})}{\mathcal{B}_{\text{inclusive}}(\text{NLL(solution 2)})}. \tag{9.1}$$

The ratios for all determined parameters are summarized in Table 9.2. We observe sizable differences. As the negative log-likelihood function is highly complex and the resonance couplings are correlated different minima can expose such large effects. Therefore, it is important to perform multiple fit attempts with randomized starting values to make sure we really find the parameters that describe the data best, i.e. the global minimum.

As the analysis is still blind, we only show fit projections in the square Dalitz variables, as they have no direct physical meaning (but no projections in ΔE and C'). They can be seen in Figure 9.1. m' is dominated by the narrow $B^0 \to \overline{D}^0[K^+\pi^-]\pi^0$ decay. The dashed black line shows the complex signal model. The fit projections nicely agree with the data points as can be seen in the pull plots, suggesting good modeling of the underlying physics processes.

Table 9.1: Summary of the fit results to the full long shutdown 1 Belle II dataset of 362 fb^{-1}. C are the blinded central values.

Wave	Parameter	Fit value
$K^*(892)^+$	$\mathcal{B}$ $[10^{-6}]$	$C \pm 1.67$
	$\mathcal{A}^{CP}$	$C \pm 0.109$
$K^*(892)^0$	$\mathcal{B}$ $[10^{-6}]$	$C \pm 0.52$
	$\mathcal{A}^{CP}$	$C \pm 0.132$
$\rho(770)^-$	$\mathcal{B}$ $[10^{-6}]$	$C \pm 1.37$
	$\mathcal{A}^{CP}$	$C \pm 0.068$
$(K\pi)_0^{*+}$	$\mathcal{B}$ $[10^{-6}]$	$C \pm 10.06$
	$\mathcal{A}^{CP}$	$C \pm 0.064$
$(K\pi)_0^{*0}$	$\mathcal{B}$ $[10^{-6}]$	$C \pm 3.02$
	$\mathcal{A}^{CP}$	$C \pm 0.123$
$\rho(1450)^-$	$\mathcal{B}$ $[10^{-6}]$	$C \pm 0.81$
	$\mathcal{A}^{CP}$	$C \pm 0.220$
$\rho(1700)^-$	$\mathcal{B}$ $[10^{-6}]$	$C \pm 0.49$
	$\mathcal{A}^{CP}$	$C \pm 0.460$
non-resonant	$\mathcal{B}$ $[10^{-6}]$	$C \pm 1.09$
	$\mathcal{A}^{CP}$	$C \pm 0.239$
	$\mathcal{B}_{\text{inclusive}}$ $[10^{-6}]$	$C \pm 3.28$
	$\mathcal{A}^{CP}_{B^0 \to \overline{D}^0[K^+\pi^-]\pi^0}$	$C \pm 0.044$
	$N_{B^0 \to \overline{D}^0[K^+\pi^-]\pi^0}$	$C \pm 16$
	$\mathcal{A}^{CP}_{B^0 \to D^-[\pi^-\pi^0]K^+}$	$C \pm 0.31$
	$N_{B^0 \to D^-[\pi^-\pi^0]K^+}$	$C \pm 3$
	$\mathcal{A}^{CP}_{q\bar{q}}$	$C \pm 0.010$
	$N_{q\bar{q}}$	$C \pm 150$
	$\mathcal{A}^{CP}_{\text{charm}}$	$C \pm 0.029$
	N_{charm}	$C \pm 46$
	$\mathcal{A}^{CP}_{\text{charmless}}$	$C \pm 0.047$
	$N_{\text{charmless}}$	$C \pm 110$

Table 9.2: Ratios (Eq. 9.1) of the physics parameters between the global minimum of the negative log-likelihood and the second smallest minimum.

	$\mathcal{B}$	$\mathcal{A}^{CP}$
inclusive	0.83	−3.40
$K^*(892)^+$	0.82	0.88
$K^*(892)^0$	0.84	1.05
$\rho(770)^-$	0.85	0.82
$(K\pi)_0^{*+}$	1.00	0.20
$(K\pi)_0^{*0}$	0.82	0.94
$\rho(1450)^-$	0.65	0.96
$\rho(1700)^-$	0.59	0.88
non-resonant	0.25	−0.63

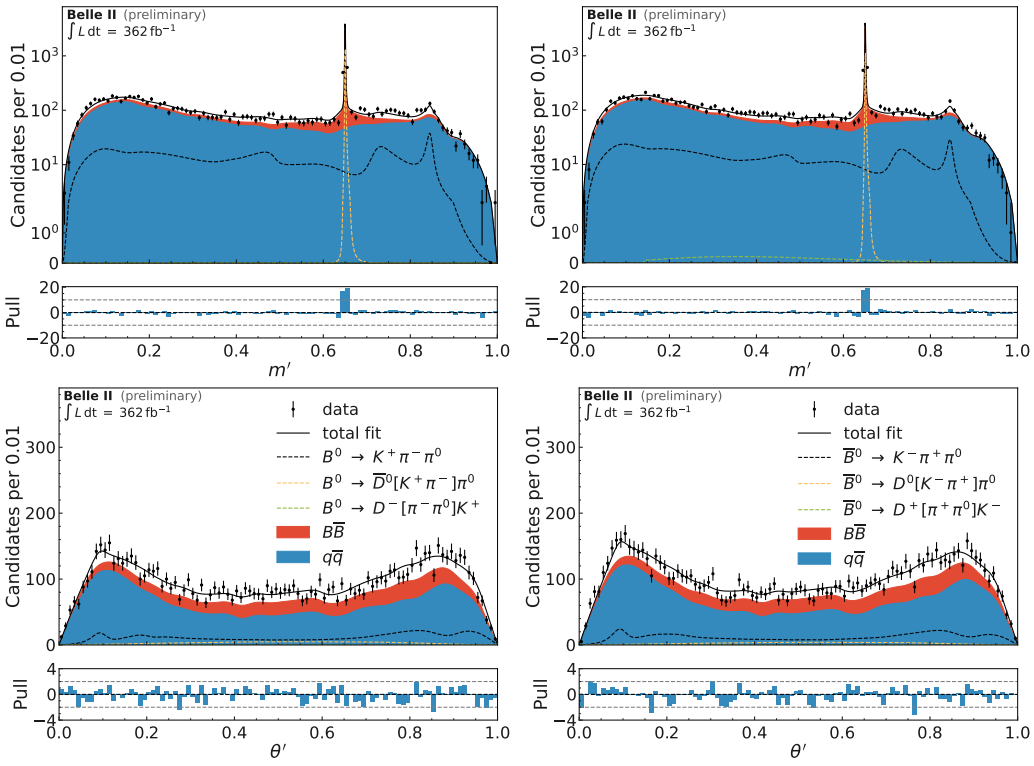

Figure 9.1: Distributions of m' (top) and θ' (bottom) for $B^0 \to K^+\pi^-\pi^0$ (left) and $\overline{B}^0 \to K^-\pi^+\pi^0$ (right) decays in 362 fb^{-1} of Belle II data. Fit projections are overlaid.

10 Systematic Uncertainties

This chapter lists all the systematic uncertainties we consider. They are summarized for the inclusive branching fraction and direct *CP*-violation in Table 10.1 and for the individual resonances in Table 10.2, 10.3, 10.4 and 10.5. The total systematic uncertainty is the quadratic sum of the individual uncertainties. Each source of systematic is explained in the following.

Table 10.1: Summary of relative systematic uncertainties on $\mathcal{B}_{\text{inclusive}}$ and the absolute uncertainties on $\mathcal{A}_{\text{inclusive}}^{CP}$.

Source	$\mathcal{B}_{\text{inclusive}}$	$\mathcal{A}_{\text{inclusive}}^{CP}$
Fit bias	1.3%	< 0.001
Tracking efficiency	0.5%	-
$B\overline{B}$ pair counting	1.5%	-
f^{00}	2.5%	-
Continuum suppression efficiency	0.5%	-
PID efficiency	1.7%	0.001
π^0 efficiency	4.6%	0.001
Resonances lineshape parameters	1.0%	0.002
Amplitude model	4.2%	0.018
Continuum model	0.5%	0.001
$B\overline{B}$ model	0.4%	0.002
Total	7.3%	0.018

Table 10.2: Summary of relative systematic uncertainties on $\mathcal{B}$ and the absolute uncertainties on $\mathcal{A}^{CP}$ of the resonances.

Resonance	Source	$\mathcal{B}$	$\mathcal{A}^{CP}$
$K^*(892)^+$	Fit bias	$< 0.1\%$	0.009
	Tracking	0.5%	-
	$B\overline{B}$ pair counting	1.5%	-
	f^{00}	2.5%	-
	Continuum suppression efficiency	0.5%	-
	PID efficiency	1.5%	0.002
	π^0 efficiency	1.5%	0.003
	Resonances lineshape parameters	3.6%	0.007
	Amplitude model	8.0%	0.026
	Continuum model	1.5%	0.004
	$B\overline{B}$ model	1.5%	0.003
	Total	9.7%	0.029
$K^*(892)^0$	Fit bias	1.2%	0.021
	Tracking	0.5%	-
	$B\overline{B}$ pair counting	1.5%	-
	f^{00}	2.5%	-
	Continuum suppression efficiency	0.5%	-
	PID efficiency	1.7%	0.004
	π^0 efficiency	1.2%	0.002
	Resonances lineshape parameters	2.7%	0.007
	Amplitude model	6.6%	0.048
	Continuum model	1.6%	0.004
	$B\overline{B}$ model	1.6%	0.003
	Total	8.4%	0.053

Table 10.3: Summary of relative systematic uncertainties on $\mathcal{B}$ and the absolute uncertainties on $\mathcal{A}^{CP}$ of the resonances.

Resonance	Source	$\mathcal{B}$	$\mathcal{A}^{CP}$
$\rho(770)^-$	Fit bias	1.1%	0.016
	Tracking	0.5%	-
	$B\overline{B}$ pair counting	1.5%	-
	f^{00}	2.5%	-
	Continuum suppression efficiency	0.5%	-
	PID efficiency	1.0%	0.003
	π^0 efficiency	0.6%	0.005
	Resonances lineshape parameters	2.8%	0.012
	Amplitude model	13.8%	0.078
	Continuum model	0.7%	0.003
	$B\overline{B}$ model	0.6%	0.003
	Total	14.5%	0.081
$(K\pi)_0^{*+}$	Fit bias	0.8%	< 0.001
	Tracking	0.5%	-
	$B\overline{B}$ pair counting	1.5%	-
	f^{00}	2.5%	-
	Continuum suppression efficiency	0.5%	-
	PID efficiency	1.1%	0.004
	π^0 efficiency	0.8%	0.006
	Resonances lineshape parameters	20.3%	0.018
	Amplitude model	3.2%	0.070
	Continuum model	0.9%	0.006
	$B\overline{B}$ model	1.1%	0.007
	Total	20.9%	0.073

Table 10.4: Summary of relative systematic uncertainties on $\mathcal{B}$ and the absolute uncertainties on $\mathcal{A}^{CP}$ of the resonances.

Resonance	Source	$\mathcal{B}$	$\mathcal{A}^{CP}$
$(K\pi)_0^{*0}$	Fit bias	$< 0.1\%$	0.009
	Tracking	0.5%	-
	$B\overline{B}$ pair counting	1.5%	-
	f^{00}	2.5%	-
	Continuum suppression efficiency	0.5%	-
	PID efficiency	2.1%	
	π^0 efficiency	1.0%	0.011
	Resonances lineshape parameters	22.4%	0.020
	Amplitude model	19.0%	0.070
	Continuum model	1.0%	0.009
	$B\overline{B}$ model	1.0%	0.009
	Total	29.7%	0.075
$\rho(1450)^-$	Fit bias	6.0%	0.036
	Tracking	0.5%	-
	$B\overline{B}$ pair counting	1.5%	-
	f^{00}	2.5%	-
	Continuum suppression efficiency	0.5%	-
	PID efficiency	1.8%	0.007
	π^0 efficiency	2.3%	0.015
	Resonances lineshape parameters	19.0%	0.101
	Amplitude model	52.7%	0.063
	Continuum model	4.3%	0.015
	$B\overline{B}$ model	3.7%	0.014
	Total	56.8%	0.127

Table 10.5: Summary of relative systematic uncertainties on $\mathcal{B}$ and the absolute uncertainties on $\mathcal{A}^{CP}$ of the resonances.

Resonance	Source	$\mathcal{B}$	$\mathcal{A}^{CP}$
$\rho(1700)^-$	Fit bias	13.2%	0.062
	Tracking	0.5%	-
	$B\overline{B}$ pair counting	1.5%	-
	f^{00}	2.5%	-
	Continuum suppression efficiency	0.5%	-
	PID efficiency	4.1%	0.021
	π^0 efficiency	4.1%	0.037
	Resonances lineshape parameters	84.5%	0.154
	Amplitude model	10.5%	0.521
	Continuum model	3.8%	0.033
	$B\overline{B}$ model	3.5%	0.017
	Total	86.6%	0.550
non-resonant	Fit bias	8.5%	0.026
	Tracking	0.5%	-
	$B\overline{B}$ pair counting	1.5%	-
	f^{00}	2.5%	-
	Continuum suppression efficiency	0.5%	-
	PID efficiency	2.8%	0.037
	π^0 efficiency	2.4%	0.046
	Resonances lineshape parameters	22.3%	0.129
	Amplitude model	83.9%	0.334
	Continuum model	5.2%	0.040
	$B\overline{B}$ model	4.3%	0.037
	Total	87.6%	0.368

10.1 Fit bias

In the ensemble test performed in Sec. 7.3 we observe small biases on the physics parameters of interest. If the mean of the Gaussian fit to the pull distribution is not compatible with zero within its uncertainty, we assign the mean as a systematic uncertainty. $\mathcal{A}^{CP}_{\text{inclusive}}$ is compatible with zero. For $\mathcal{B}_{\text{inclusive}}$ we observe a bias, which is 18% of the statistical uncertainty. The uncertainties of the resonances are summarized in Table 10.6. They are given as relative uncertainties on the statistical uncertainty and translated into relative uncertainties on the branching fractions in Tables above via the blinded central values of the fit on data.

Table 10.6: Summary of the branching fraction and direct *CP*-violation parameter uncertainties for the resonances due to fit biases. The values are given in percent of the statistical uncertainty.

	$\mathcal{B}$	$\mathcal{A}^{CP}$
$K^*(892)^+$	$< 0.1\%$	8.2%
$K^*(892)^0$	7.7%	16.4%
$\rho(770)^-$	11.1%	24.1%
$(K\pi)_0^{*+}$	8.9%	$< 0.1\%$
$(K\pi)_0^{*0}$	$< 0.1\%$	7.7%
$\rho(1450)^-$	15.8%	16.2%
$\rho(1700)^-$	20.6%	13.5%
non-resonant	31%	11.1%

10.2 Tracking Efficiency

The efficiency of the track reconstruction is provided by the Belle II performance group and is described in detail in the Belle II internal note [67]. It is determined in $e^+e^- \to \tau^+\tau^-$ events, where one tau decays leptonically ($\tau \to l^\pm \nu_\ell \overline{\nu}_\tau$, $l = e,\ \mu$) while the other decays hadronically to three charged pions ($\tau \to 3\pi^\pm \nu_\tau + n\pi^0$). The lepton and two of the charged pions are used to tag τ-pair events. The existence of the last pion can be inferred from charge conservation. The efficiency is determined by checking whether the last track is reconstructed or not. As suggested, we include a systematic uncertainty of 0.24% per charged track.

10.3 $B\overline{B}$ Pair Counting

The total number of produced $B\overline{B}$ pairs (i.e. $B^0\ \overline{B}^0$ and $B^+\ B^-$) is provided by the Belle II performance group and is described in detail in the Belle II internal notes [68, 69]. To this end, the produced hadronic events in on-resonance and off-resonance data, recorded at a center-of-mass energy of $10.519\,\mathrm{GeV}/c^2$, are studied. The number of $B\overline{B}$ pairs is given as

$$N_{B\overline{B}}^{tot} = \frac{N_{\mathrm{on-res}} - R \cdot N_{\mathrm{off-res}} \cdot k}{\epsilon_{B\overline{B}}} \tag{10.1}$$

where $N_{\mathrm{on-res}}$ is the number of all hadronic events in on-resonance data, $R \cdot N_{\mathrm{off-res}} \cdot k$ is the number of non-$B\overline{B}$ events in the on-resonance data and $\epsilon_{B\overline{B}}$ is the efficiency of the hadronic selection for $B\overline{B}$ events. $R = \frac{\mathcal{L}_{\mathrm{on-res}}}{\mathcal{L}_{\mathrm{off-res}}}$ is the luminosity ratio between the on- and off-resonace data, which is 10. k describes the variation in non-$B\overline{B}$ efficiencies and cross-sections with beam energy. The reported number of produced $B\overline{B}$ pairs is $N_{B\overline{B}}^{tot} = (387 \pm 6(stat. + sys.)) \times 10^6$. Hence, we assign a systematical uncertainty of 1.5%.

10.4 f^{00}

f^{00} is the decay rate of $\Upsilon(4S) \to B^0\overline{B}^0$. Multiplying f^{00} with the afore described number of total $B\overline{B}$ pairs yields the number of B^0 $\overline{B}^0$ pairs. The value of f^{00} is taken from [70] where $B^0 \to J/\psi K^0$ and $B^+ \to J/\psi K^+$ decays are used to measure

$$f^{00}/f^{+-} = 1.065 \pm 0.052 \tag{10.2}$$

where f^{+-} is the decay rate of $\Upsilon(4S) \to B^+B^-$. This yields an uncertainty of 2.5% on f^{00}, which we state as systematic uncertainty.

10.5 Continuum Suppression Efficiency

As explained in Subesec. 8.1.2 we state a 1.6% uncertainty on the continuum suppression efficiency determined in the $B^- \to D^0[K^-\pi^+\pi^0]\pi^-$ channel as systematic uncertainty.

10.6 Particle ID (PID) Correction

As explained in Sec. 8.2 we use the `Systematics Correction Framework` to correct for different efficiencies of PID selection in real and simulated data. Correction weights as well as their statistical and systematical uncertainties are deduced in bins of the track momentum and the polar angle. We then use the `PIDvar` framework [71] to apply the weights on our dataset. Additionally, `PIDvar` can generate alternative weights. The alternative weights are sampled from multivariate Gaussian functions with the widths corresponding to the statistical and systematical uncertainties. The statistical uncertainties are assumed to be uncorrelated, while systematical uncertainties are assumed to be fully correlated [72]. We generate 200 alternative weights and fit the real data. The standard deviations of the resulting distributions of the physics parameters are taken as systematic uncertainty.

10.7 π^0 Efficiency

As described in Sec. 8.3 we correct for different π^0 reconstruction efficiencies between simulated and real data. To this end, we deduce weights in bins of the π^0 momentum and polar angle. Additionally, we determine 200 alternative weights, sampled from multivariate Gaussian functions with the widths corresponding to the statistical and systematical uncertainties of the nominal weights. The statistical uncertainties are assumed to be uncorrelated, while systematical uncertainties are assumed to be fully correlated. We then fit the real data with these alternative weights. We state the standard deviations of the distributions of the physics parameters as systematic uncertainty.

10.8 Resonance Lineshape Parameters

The resonance parameters (masses, widths and radii) in our amplitude model are fixed to the best know values. In order to evaluate the related uncertainties, we perform 400 ensemble test. We randomly fluctuate these parameters within their measured uncertainties (see Table 3.1) and draw samples from the fluctuated models. Due to the lack of better knowledge, we assume all parameters to be uncorrelated, although especially the masses and widths of the resonances certainly expose some correlations. We then fit the fluctuated and the nominal model. For direct *CP*-violation parameters we calculate the difference between the nominal and the fluctuated fit, i.e.

$$x_{\text{nominal}} - x_{\text{fluctuated}}. \tag{10.3}$$

Since the branching fraction is an absolute value and not a ratio like the direct *CP*-violation, we normalize the difference with the value determined from the fit of the nominal model, i.e.

$$\frac{x_{\text{nominal}} - x_{\text{fluctuated}}}{x_{\text{nominal}}}. \tag{10.4}$$

This means, that we determine a relative error on branching fractions and an absolute error on direct *CP*-violation parameters. We then fit these distributions with a Gaussian function.

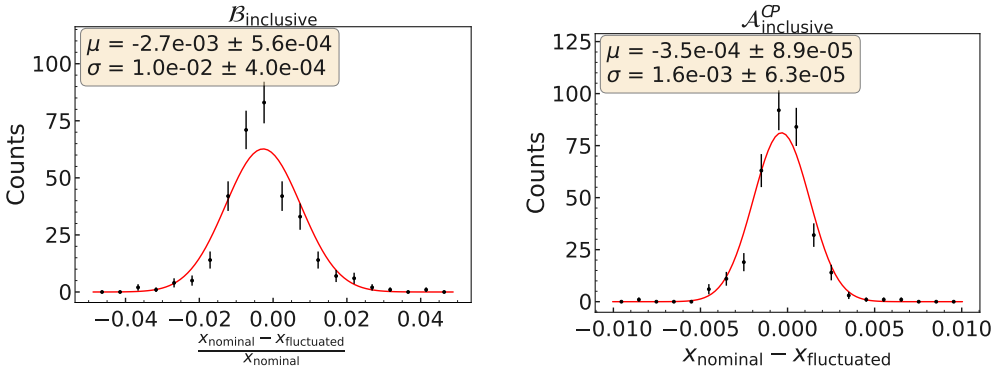

Figure 10.1: Distributions of differences between fits of the nominal and the fluctuated lineshape model for $\mathcal{B}_{\text{inclusive}}$ (left) and $\mathcal{A}^{CP}_{\text{inclusive}}$ (right). A Gaussian fit is overlaid.

The obtained distributions for $\mathcal{B}_{\text{inclusive}}$ and $\mathcal{A}^{CP}_{\text{inclusive}}$ are shown in Figure 10.1. Both distribution are compatible with zero within one standard deviation (width). The width of $\mathcal{B}_{\text{inclusive}}$ is 1% which is assigned as systematic uncertainty. The width of $\mathcal{A}^{CP}_{\text{inclusive}}$ is $\ll 1\%$ and we consider it negligible. Both Gaussian fits show some deviation from the black data points, i.e. its questionable whether the assumption of Gaussian error is valid here. However, as the overall effects are so small we stick to the Gaussian error assumption.

The results of the Gaussian fits to the resonance branching fractions and direct *CP*-violation parameters are show in Figure 10.2. The central values are the mean and the

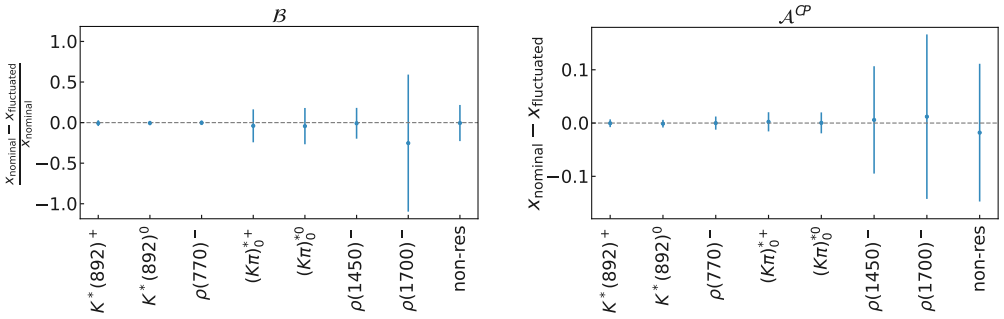

Figure 10.2: Results of the Gaussian fits to the determined differences between nominal and fluctuated lineshape model for the resonance branching fractions (left) and direct *CP*-violation parameters (right). The central value is the mean and the errorbars are the width of the Gaussian function.

errorbars are the width of the fitted Gaussian function. For the parameters that are compatible with zero within one standard deviation, we assign the width of the Gaussian fit as a systematic uncertainty. For the parameters that are not compatible with zero within on standard deviation, we assign the mean of the Gaussian fit as uncertainty. The uncertainties are summarized in Table 10.7. On our main parameters of interest, i.e. $K^*(892)^+$, $K^*(892)^0$ (and also $\rho(770)^-$) we observe small effects as the resonance lineshape parameters are measured precisely. Larger effects are seen on the $(K\pi)$ s-wave contributions and especially the non-resonant, $\rho(1450)^-$ and $\rho(1700)^-$ are heavily influenced. The reason being, that they are small contributions as well as their resonance parameters are measured rather imprecisely. Peculiarly, the widths of the ρ resonances have large uncertainties, such that different widths can make the resonances overlap more heavily and influence their measured couplings.

Table 10.7: Summary of the relative branching fraction uncertainties and absolute direct *CP*-violation parameter uncertainties for the resonances determined for a fluctuated lineshape model.

	$\mathcal{B}$	$\mathcal{A}^{CP}$
$K^*(892)^+$	3.5%	0.007
$K^*(892)^0$	2.7%	0.007
$\rho(770)^-$	2.8%	0.012
$(K\pi)_0^{*+}$	20.3%	0.018
$(K\pi)_0^{*0}$	22.4%	0.020
$\rho(1450)^-$	19.0%	0.101
$\rho(1700)^-$	84.5%	0.155
non-resonant	22.3%	0.129

10.9 Amplitude Model

The amplitude model is not a-priori defined. In principle one can add resonances with higher masses or angular momenta. However, the available phase space decreases and they contribute less to the overall amplitude. Our model contains seven intermediate resonances and one non-resonant component. To estimate the uncertainty due to our fixed amplitude model we fit two different amplitude models to real data. In the first alternative model, we drop the two $\rho(1450)^-$ and $\rho(1700)^-$ resonances, as they are expected to be small. In the second alternative model, we in include four additional resonances. They are listed in Table 10.8.

Table 10.8: Lineshape parameters of additional resonances, included to evaluate the systematic uncertainty related to the amplitude model. The parameters are taken form [15]. Since the length parameters R are not well measured, we assume a value of 5, which corresponds to 1 fm.

Resonance	Lineshape	Parameters
	Spin $J = 1$	
$K^*(1680)^0$	RBW	$M = 1718\,\mathrm{MeV}/c^2$
		$\Gamma^0 = 322\,\mathrm{MeV}$
		$R = 5(\,\mathrm{GeV})^{-1}$
$K^*(1680)^+$	RBW	$M = 1718\,\mathrm{MeV}/c^2$
		$\Gamma^0 = 322\,\mathrm{MeV}$
		$R = 5(\,\mathrm{GeV})^{-1}$
	Spin $J = 2$	
$K_2^*(1430)^0$	RBW	$M = 1432\,\mathrm{MeV}/c^2$
		$\Gamma^0 = 109\,\mathrm{MeV}$
		$R = 5(\,\mathrm{GeV})^{-1}$
$K_2^*(1430)^+$	RBW	$M = 1427\,\mathrm{MeV}/c^2$
		$\Gamma^0 = 100\,\mathrm{MeV}$
		$R = 5(\,\mathrm{GeV})^{-1}$

For direct *CP*-violation parameters we evaluate the differences (see Eq. 10.3) between the fit results of the nominal and alternative model. For branching fractions we evaluate the normalized differences (see Eq. 10.4). The results for the inclusive branching fraction and direct *CP*-violation parameters are summarized in Table 10.9.

Table 10.9: Summary of relative differences on $\mathcal{B}_{\mathrm{inclusive}}$ and the absolute differences on $\mathcal{A}^{CP}_{\mathrm{inclusive}}$ between the nominal and the two alternative amplitude models.

Amplitude model	$\mathcal{B}_{\mathrm{inclusive}}$	$\mathcal{A}^{CP}_{\mathrm{inclusive}}$
no $\rho(1450)^-$ and $\rho(1700)^-$	4.2%	0.007
$K^*(1680)^0$, $K^*(1680)^+$, $K_2^*(1430)^0$ and $K_2^*(1430)^+$	1.1%	0.018

Table 10.10: Summary of relative differences on the resonance branching fractions and the absolute differences on the resonance direct *CP*-violation parameters between the nominal amplitude model and two alternative amplitude models. One without the $\rho(1450)^-$ and $\rho(1700)^-$ resonances and one including the $K^*(1680)^0$, $K^*(1680)^+$, $K_2^*(1430)^0$ and $K_2^*(1430)^+$ resonances.

	w/o $\rho(1450)^-$ and $\rho(1700)^-$		w/ $K^*(1680)^0$, $K^*(1680)^+$, $K_2^*(1430)^0$ and $K_2^*(1430)^+$	
	$\mathcal{B}$	$\mathcal{A}^{CP}$	$\mathcal{B}$	$\mathcal{A}^{CP}$
$K^*(892)^+$	8.0%	0.023	7.7%	0.026
$K^*(892)^0$	6.3%	0.013	1.4%	0.048
$\rho(770)^-$	13.8%	0.078	9.2%	0.031
$(K\pi)_0^{*+}$	3.2%	0.023	1.2%	0.070
$(K\pi)_0^{*0}$	2.9%	0.014	19.0%	0.070
$\rho(1450)^-$	-	-	52.7%	0.063
$\rho(1700)^-$	-	-	10.5%	0.521
non-resonant	83.8%	0.334	1.7%	0.003

The results on the resonance parameters are listed in Table 10.10. We state the larger values between the two alternative models as uncertainties. The largest effects are observed on the non-resonant contribution in the model without the two ρ resonances. Probably, the missing ρ waves are compensated by the non-resonant contribution. Large effects are also seen for the $\rho(1450)^-$ and $\rho(1700)^-$ in the model with the four additional waves. As they are small contributions different amplitude models impact them more heavily.

10.10 Continuum Model

As described in Subsec. 6.3.1 the continuum Dalitz model is extracted from a $M_{\rm bc}$ sideband which is re-weighted to match the $M_{\rm bc}$ signal region. The weights are taken from simulated data. To evaluate the effect of the limited sample size of simulated data, we perform 200 ensemble test, where we draw samples from the PDF with the weights randomly fluctuated within their uncertainties. We assume Poisson uncertainties for the weights. We then fit the fluctuated and the nominal model. For direct *CP*-violation parameters we calculate the difference between the nominal and the fluctuated fit (see Eq. 10.3). For the branching fractions we determine the normalized difference (see Eq. 10.4). We then fit these distributions with a Gaussian function. The obtained distributions for $\mathcal{B}_{\rm inclusive}$ and $\mathcal{A}^{CP}_{\rm inclusive}$ are shown in Figure 10.3. Both distribution are compatible with zero within one standard deviation (width). The distance to zero, as well as the widths of both distributions are $\ll 1\%$, i.e. the effect of a potentially different continuum model on these two physics parameters seems negligible and we do not assign a systematic uncertainty.

The results of the Gaussian fits to the resonance branching fractions and direct *CP*-violation parameters are show in Figure 10.4. The central values are the mean and the

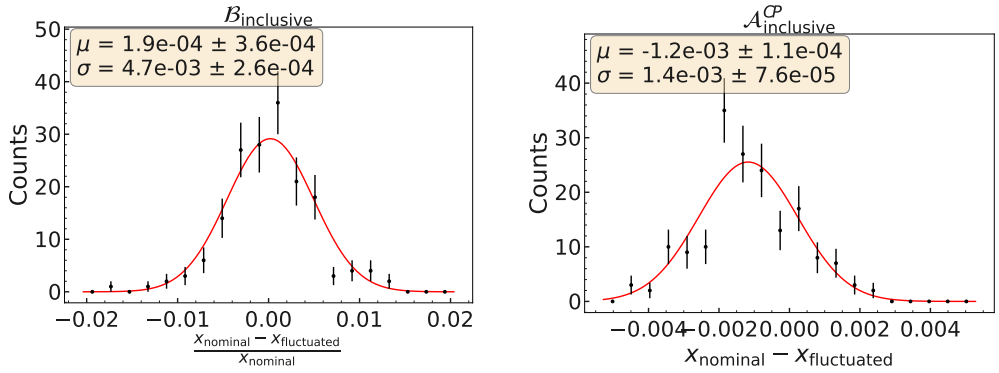

Figure 10.3: Distributions of differences between fits of the nominal and the fluctuated continuum model for $\mathcal{B}_{\text{inclusive}}$ (left) and $\mathcal{A}^{CP}_{\text{inclusive}}$ (right). A Gaussian fit is overlaid.

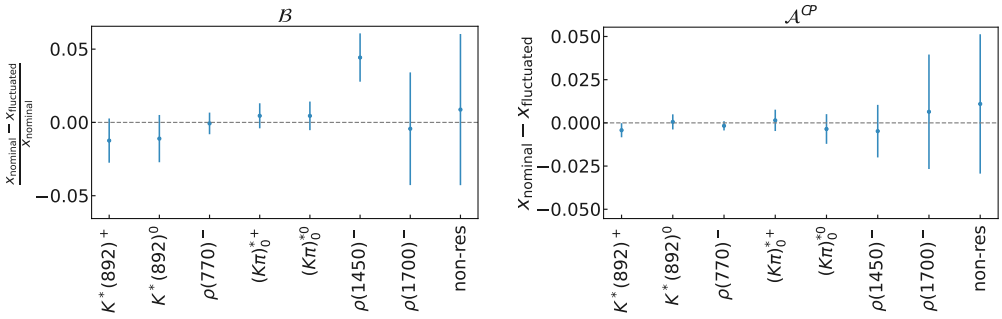

Figure 10.4: Results of the Gaussian fits to the determined differences between nominal and fluctuated continuum model for the resonance branching fractions (left) and direct *CP*-violation parameters (right). The central value is the mean and the errorbars are the width of the Gaussian function.

errorbars are the width of the fitted Gaussian function. Here we observe larger effects than for the inclusive parameters, i.e. single resonances are more susceptible to different continuum models. The reason being that a fluctuation of a background in the resonance region of the Dalitz plot (largely) affect that resonance, while for the inclusive parameters these effects average out over the Dalitz plot. For the parameters that are compatible with zero within one standard deviation, we assign the width of the Gaussian fit as a systematic uncertainty. For the parameters that are not compatible with zero within on standard deviation, we assign the mean of the Gaussian fit as uncertainty.

The continuum model uncertainties for the resonances are summarized in Table 10.11. Mainly, the non-resonant and the two $\rho(1450)^-$ and $\rho(1700)^-$ resonances are affected. As they are expected to be small, even small variations in the affect their physics parameters.

Table 10.11: Summary of the relative branching fraction uncertainties and absolute direct *CP*-violation parameter uncertainties for the resonances determined for a fluctuated continuum model.

	$\mathcal{B}$	$\mathcal{A}^{CP}$
$K^*(892)^+$	1.5%	0.004
$K^*(892)^0$	1.6%	0.004
$\rho(770)^-$	0.7%	0.003
$(K\pi)_0^{*+}$	0.9%	0.006
$(K\pi)_0^{*0}$	1.0%	0.009
$\rho(1450)^-$	4.4%	0.015
$\rho(1700)^-$	3.8%	0.033
non-resonant	5.2%	0.040

10.11 $B\overline{B}$ Model

The $B\overline{B}$ Dalitz model is extracted from simulated data as 2D-histograms. To evaluate the uncertainty given the limited amount of simulated data, we perform 200 ensemble test. We draw samples from the PDF where we randomly fluctuate the bins of the histograms within their Poisson uncertainties. We then fit the fluctuated and the nominal model. For direct *CP*-violation parameters we calculate the difference between the nominal and the fluctuated fit (see Eq. 10.3). For the branching fractions we determine the normalized difference (see Eq. 10.4). We then fit these distributions with a Gaussian function.

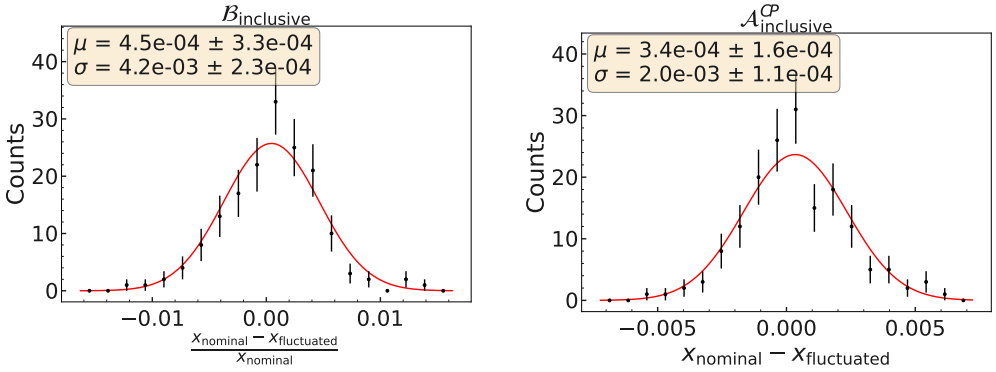

Figure 10.5: Distributions of differences between fits of the nominal and the fluctuated $B\overline{B}$ model for $\mathcal{B}_{\text{inclusive}}$ (left) and $\mathcal{A}^{CP}_{\text{inclusive}}$ (right). A Gaussian fit is overlaid.

The obtained distributions for $\mathcal{B}_{\text{inclusive}}$ and $\mathcal{A}^{CP}_{\text{inclusive}}$ are shown in Figure 10.5. Both distribution are compatible with zero within one standard deviation (width). The distance to zero, as well as the widths of both distributions are $\ll 0.1\%$, i.e. the effect of a potentially different $B\overline{B}$ model on these two physics parameters seems negligible and we do not assign a systematic uncertainty.

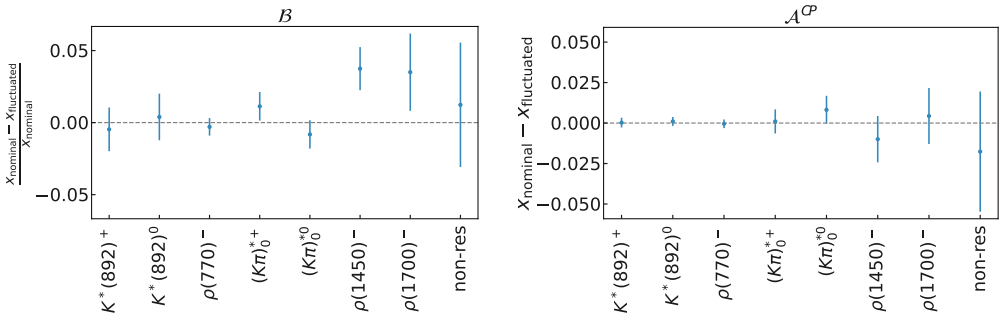

Figure 10.6: Results of the Gaussian fits to the determined differences between nominal and fluctuated $B\overline{B}$ model for the resonance branching fractions (left) and direct *CP*-violation parameters (right). The central value is the mean and the errorbars are the width of the Gaussian function.

The results of the Gaussian fits to the resonance branching fractions and direct *CP*-violation parameters are show in Figure 10.6. The central values are the mean and the errorbars are the width of the fitted Gaussian function. We observe similar effects as in the above continuum uncertainty. For the parameters that are compatible with zero within one standard deviation, we assign the width of the Gaussian fit as a systematic uncertainty. For the parameters that are not compatible with zero within on standard deviation, we assign the mean of the Gaussian fit as uncertainty.

Table 10.12: Summary of the relative branching fraction uncertainties and absolute direct *CP*-violation parameter uncertainties for the resonances determined for a fluctuated $B\overline{B}$ model.

	$\mathcal{B}$	$\mathcal{A}^{CP}$
$K^*(892)^+$	1.5%	0.003
$K^*(892)^0$	1.6%	0.003
$\rho(770)^-$	0.6%	0.003
$(K\pi)_0^{*+}$	1.1%	0.007
$(K\pi)_0^{*0}$	1.0%	0.009
$\rho(1450)^-$	3.7%	0.014
$\rho(1700)^-$	3.5%	0.017
non-resonant	4.3%	0.037

The $B\overline{B}$ model uncertainties for the resonances are summarized in Table 10.12. Overall, the effect of different $B\overline{B}$ models on the resonance parameters is small with the largest effect on small resonances like $\rho(1450)^-$ and $\rho(1700)^-$ or the non-resonant contribution.

10.12 Discussion

The dominating systematic uncertainties are the amplitude model itself and the uncertainties on the resonance lineshape parameters. The lineshape parameters are external inputs and therefore cannot be improved, unless spectroscopy experiments determine them more precisely. The large error on the amplitude model stems from the fact, that we include a certain set of waves in our model. However, in principle there can be more resonances with higher masses or angular momenta. Currently we are developing a systematic approach to determine the "correct" wave set. The idea is a two step fit approach. In the first fit the amplitude model contains a large set of waves. Additionally, we include a compensation term, that pulls down the couplings, if a wave is not strongly represented. By running this first fit on data, we can determine the resonances that are significantly contributing to the overall amplitude in real data. In the subsequent second fit we only include those resonances in our amplitude model, remove the compensation term and determine the couplings. This way we get a wave set that is justified by real data and we can better determine its uncertainties, instead of just randomly adding or dropping resonances, as it is done in this thesis.

Sub-leading uncertainties are the uncertainty on f^{00}, PID and π^0 efficiency, which all contain a statistical component and will decrease with a larger dataset.

Potentially, the observed fit biases from the ensemble test can be decreased by more elaborate techniques than simple histograms used throughout this analysis. However, such studies have not been conducted yet.

In any case, large systematic effects are only observed for the contributions, which are expected to be small, like the higher ρ resonances or the non-resonant component. The main goal of this analysis is the determination of the branching fraction and direct CP-violation of the $B^0 \to K^*\pi$ modes to measure the $K^*\pi$ isospin sum rule. For these channels the systematic uncertainties are well under control.

11 Results

Combining the statistical and systematic uncertainties, we obtain an inclusive branching fraction and direct *CP*-violation of

$$\begin{aligned}\mathcal{B}_{\text{inclusive}} &= (C \pm [3.28]\,(\text{stat.}) \pm [C \times 7.3\%]\,(\text{sys.})) \times 10^{-6} \text{ and}\\ \mathcal{A}^{CP}_{\text{inclusive}} &= C \pm [0.041]\,(\text{stat.}) \pm [0.018]\,(\text{sys.}),\end{aligned}$$

where C are the blinded central values.

For the resonance branching fractions we report

$$\begin{aligned}\mathcal{B}(B^0 \to K^*(892)^+\pi^-) &= (C \pm [1.67]\,(\text{stat.}) \pm [C \times 9.7\%]\,(\text{sys.})) \times 10^{-6},\\ \mathcal{B}(B^0 \to K^*(892)^0\pi^0) &= (C \pm [0.52]\,(\text{stat.}) \pm [C \times 8.4\%]\,(\text{sys.})) \times 10^{-6},\\ \mathcal{B}(B^0 \to \rho(770)^-K^+) &= (C \pm [1.37]\,(\text{stat.}) \pm [C \times 14.5\%]\,(\text{sys.})) \times 10^{-6},\\ \mathcal{B}(B^0 \to (K\pi)_0^{*+}\pi^-) &= (C \pm [10.06]\,(\text{stat.}) \pm [C \times 20.9\%]\,(\text{sys.})) \times 10^{-6},\\ \mathcal{B}(B^0 \to (K\pi)_0^{*0}\pi^0) &= (C \pm [3.02]\,(\text{stat.}) \pm [C \times 29.7\%]\,(\text{sys.})) \times 10^{-6},\\ \mathcal{B}(B^0 \to \rho(1450)^-K^+) &= (C \pm [0.81]\,(\text{stat.}) \pm [C \times 56.8\%]\,(\text{sys.})) \times 10^{-6},\\ \mathcal{B}(B^0 \to \rho(1700)^-\pi^0) &= (C \pm [0.49]\,(\text{stat.}) \pm [C \times 86.6\%]\,(\text{sys.})) \times 10^{-6}, \text{ and}\\ \mathcal{B}(B^0 \to K^+\pi^-\pi^0 \text{ non-resonant}) &= (C \pm [1.09]\,(\text{stat.}) \pm [C \times 87.6\%]\,(\text{sys.})) \times 10^{-6}\end{aligned}$$

and for the direct *CP*-violation parameters

$$\begin{aligned}\mathcal{A}^{CP}(B^0 \to K^*(892)^+\pi^-) &= C \pm [0.109]\,(\text{stat.}) \pm [0.029]\,(\text{sys.}),\\ \mathcal{A}^{CP}(B^0 \to K^*(892)^0\pi^0) &= C \pm [0.132]\,(\text{stat.}) \pm [0.053]\,(\text{sys.}),\\ \mathcal{A}^{CP}(B^0 \to \rho(770)^-K^+) &= C \pm [0.068]\,(\text{stat.}) \pm [0.081]\,(\text{sys.}),\\ \mathcal{A}^{CP}(B^0 \to (K\pi)_0^{*+}\pi^-) &= C \pm [0.064]\,(\text{stat.}) \pm [0.073]\,(\text{sys.}),\\ \mathcal{A}^{CP}(B^0 \to (K\pi)_0^{*0}\pi^0) &= C \pm [0.123]\,(\text{stat.}) \pm [0.075]\,(\text{sys.}),\\ \mathcal{A}^{CP}(B^0 \to \rho(1450)^-K^+) &= C \pm [0.220]\,(\text{stat.}) \pm [0.127]\,(\text{sys.}),\\ \mathcal{A}^{CP}(B^0 \to \rho(1700)^-\pi^0) &= C \pm [0.460]\,(\text{stat.}) \pm [0.550]\,(\text{sys.}), \text{ and}\\ \mathcal{A}^{CP}(B^0 \to K^+\pi^-\pi^0 \text{ non-resonant}) &= C \pm [0.239]\,(\text{stat.}) \pm [0.368]\,(\text{sys.}).\end{aligned}$$

We compare the precisions achieved in this thesis and the *BABAR* analysis by translating our relative uncertainties on the resonance branching fractions into absolute uncertainties using the central values of the *BABAR* analysis (The used *BABAR* values are listed in the Appendix in Table A.1). The comparisons are shown in Figures 11.1 and 11.2. Most of our channels would be systematically limited if our central values are similar to the *BABAR*

values, i.e. we will improve the precisions simply by acquiring more data. Overall we are able to achieve similar uncertainties as the *BABAR* analysis.

The differences on the statistical uncertainties could be due to statistical fluctuations. E.g. if we would measure a resonance branching fraction twice as high as *BABAR* did, our absolute errors might be larger, while the relative error could be smaller.

The large difference on the systematic uncertainty on the non-resonant component stems from the way we evaluate the amplitude model dependent uncertainty (see Sec. 10.9). *BABAR* only fitted one alternative amplitude model, adding the $K^*(1680)^0$, $K^*(1680)^+$, $K_2^*(1430)^0$ and $K_2^*(1430)^+$ resonances. We are also fitting an alternative model where we drop the $\rho(1450)^-$ and $\rho(1700)^-$ resonances, which yields an relative uncertainty of 87.6% on the non-resonant branching fraction. If we would take the uncertainty we get form the amplitude model with the four additional resonances, the relative uncertainty would be 1.7%, i.e. our estimation is more conservative.

The extremely small systematical uncertainty on the direct *CP*-violation parameter in the $B^0 \to (K\pi)_0^{*+}\pi^-$ channel in the *BABAR* is difficult to explain without knowing the internal details.

However, on the $B^0 \to K^*(892)^+\pi^-$ and $B^0 \to K^*(892)^0\pi^0$ channels, which are our main interest to measure the $K^*\pi$ isospin sum rule, we achieve very similar uncertainties.

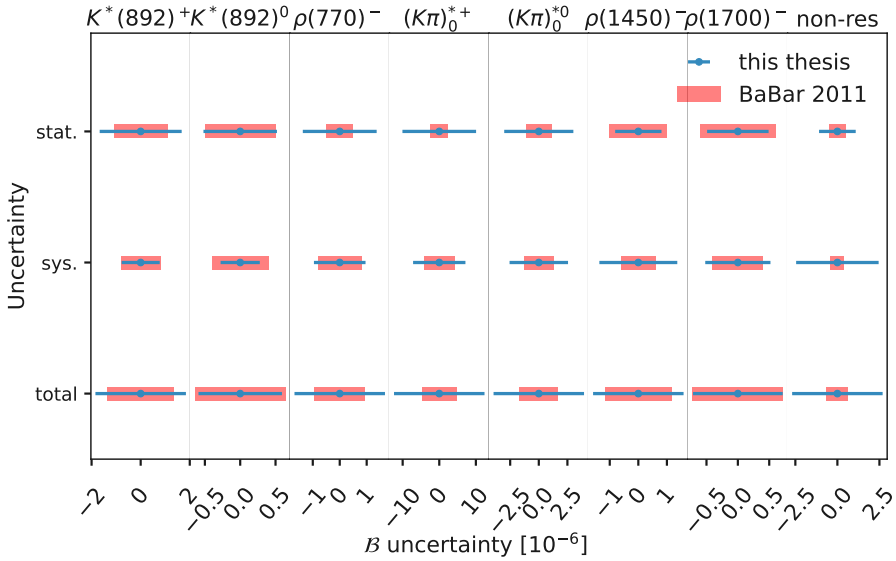

Figure 11.1: Comparison of the statistical, systematic and total uncertainties of the resonance branching fractions between this thesis and the *BABAR* analysis [8].

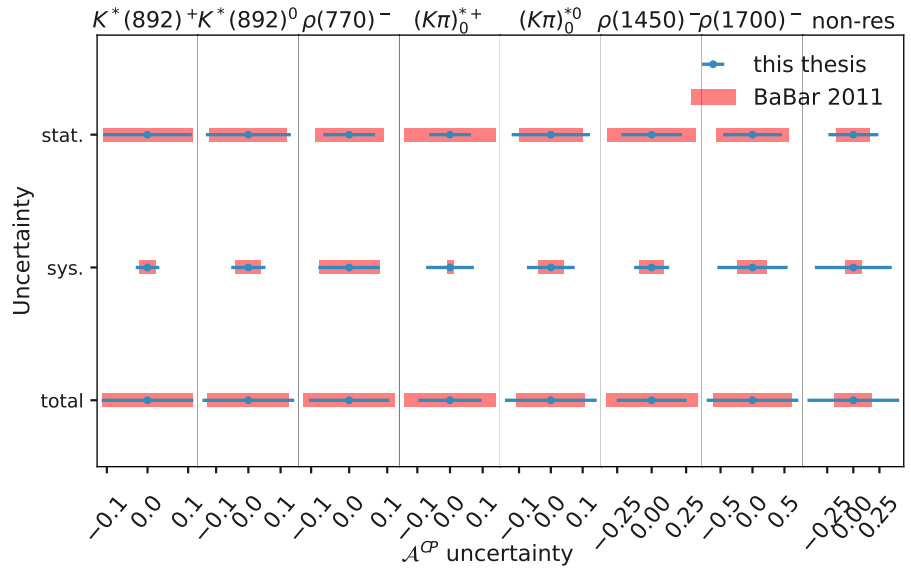

Figure 11.2: Comparison of the statistical, systematic and total uncertainties of the resonance direct *CP*-violation parameters between this thesis and the *BABAR* analysis [8].

11.1 Estimation of the Precision on the $K^*\pi$ Isospin Sum Rule

We evaluate the statistical precision on $I_{K^*\pi}$ (see Eq. 2.43) using the statistical uncertainties of $B^0 \to K^*(892)^+\pi^-$ and $B^0 \to K^*(892)^0\pi^0$ measured in this thesis and

$$\begin{aligned}
\mathcal{B}(B^+ \to K^*(892)^0\pi^+) &= (11.6 \pm 0.5\,(\text{stat.}) \pm 1.1\,(\text{sys.})) \times 10^{-6}, \\
\mathcal{A}^{CP}(B^+ \to K^*(892)^0\pi^+) &= 0.025 \pm 0.050\,(\text{stat.}) \pm 0.016\,(\text{sys.}), \\
\mathcal{B}(B^+ \to K^*(892)^+\pi^0) &= (8.8 \pm 1.0\,(\text{stat.}) \pm 0.6\,(\text{sys.})) \times 10^{-6}, \text{ and} \\
\mathcal{A}^{CP}(B^+ \to K^*(892)^+\pi^0) &= -0.39 \pm 0.12\,(\text{stat.}) \pm 0.003\,(\text{sys.})
\end{aligned}$$

from a Dalitz plot analysis of $B^+ \to K^0_S\pi^+\pi^0$ decays at *BABAR* [73]. The lifetime ratio is $\tau_{B^0}/\tau_{B^+} = 0.9294 \pm 0.0035$ [15]. The development of the statistical precision on $I_{K^*\pi}$ is shown in Figure 11.3, where we assume that the statistical precision $\Delta_{\text{stat.}}$ scales with integrated luminosity $L_{\text{int.}}$ like

$$\begin{aligned}
L_{\text{int.}} &\to 2 \times L_{\text{int.}}, \\
\Delta_{\text{stat.}} &\to \frac{1}{\sqrt{2}} \times \Delta_{\text{stat.}}.
\end{aligned}$$

We will achieve statistical precisions of about 5% at an integrated luminosity of $5\,\text{ab}^{-1}$ and a precision of about 1% at the target integrated luminosity of $50\,\text{ab}^{-1}$. The current systematical uncertainty is calculated assuming no correlations between the individual systematical uncertainties of the measurements. This is just an approximation as e.g. the

PID efficiency uncertainties in this thesis are calculated from the same efficiency ratio tables and are therefore certainly correlated. Assuming no improvement in the systematic uncertainty the maximal total precision is about 6.5%, governed by the systematic uncertainties. However, some of them, such as the PID and π^0 efficiency uncertainties, have a statistical component and will also shrink with increasing luminosities. Therefore, it is not yet known which precision can finally be achieved. As currently the measurements are statistically limited, we can still significantly improve our precisions by acquiring more data at Belle II.

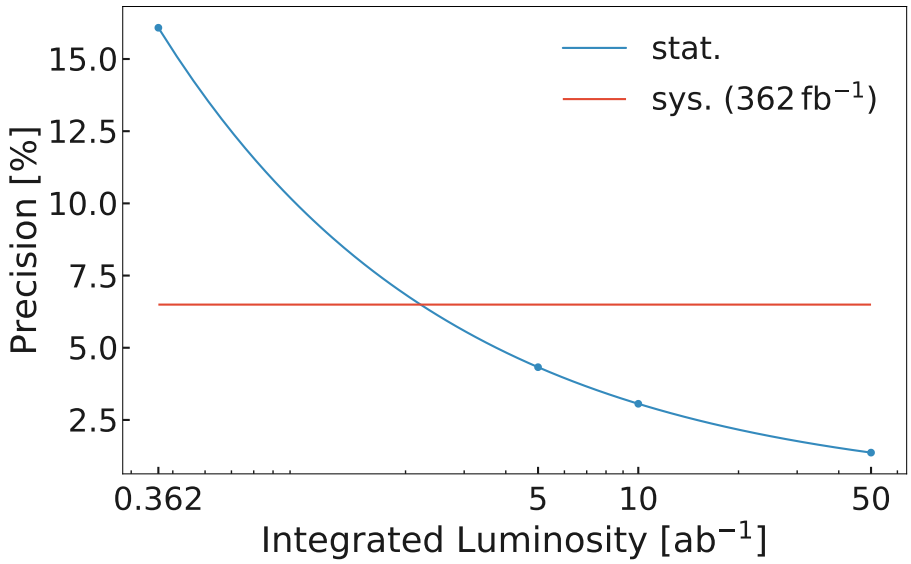

Figure 11.3: Estimated development of the statistical precision of $I_{K^*\pi}$ with the integrated luminosity at Belle II.

12 Summary and Outlook

This thesis reports on a model dependent Dalitz plot analysis of $B^0 \to K^+\pi^-\pi^0$ decays at the Belle II experiment. In total, 387×10^6 pairs of bottom-antibottom mesons, produced in e^+e^- collisions at the SuperKEKB accelerator, are studied. Our model contains seven intermediate resonances and a non-resonant contribution. In particular the $B^0 \to K^*(892)^0\pi^0$ and $B^0 \to K^*(892)^+\pi^-$ decays are of interest, since they serve as inputs for the $K^*\pi$ isospin sum rule to probe the Standard Model. The $B^0 \to K^+\pi^-\pi^0$ decay has a small branching fraction of $\mathcal{O}(10^{-5})$ and is therefore heavily background dominated. The first challenge of the analysis is to reconstruct $B^0 \to K^+\pi^-\pi^0$ decays with a high efficiency, while at the same time rejecting backgrounds. To this end, dedicated multivariate analysis techniques (GBDT) are employed, which exploit the topological differences between B-meson events and lighter $q\overline{q}$ events, which pose the main background. Subsequently, we develop a complex amplitude model and account for detector effects like acceptance and resolution. The Dalitz plot shapes of remaining backgrounds are modeled with histograms. For $B\overline{B}$ backgrounds we extracted the histograms from simulated data. Due to poor modeling of $q\overline{q}$ backgrounds in simulated data, we extract its shape from an M_{bc} sideband in real data. To correct for different kinematics in the M_{bc} sideband and signal region we reweight the histogram. The fit model is validated in control modes and ensemble tests. Furthermore, several corrections are deduced in control modes to account for shape and efficiency differences between simulated data and real data. Finally, we estimate major sources of systematic uncertainties. As the analysis is still under Belle II internal review, we blind the central values and state uncertainties only. Most uncertainties are governed by the limited size of the data sample (i.e. statistically). Hence, the precision will improve significantly with the large Belle II dataset. The dominating systematical uncertainties stem from the fixed set of considered waves in the amplitude model. As the optimal wave set is not a priori known, we fit two alternative amplitude models with more and less resonances included. We observe large differences on the physical parameters and state them as uncertainties. To improve on that, we are currently developing an approach to extract the optimal wave set directly from real data. Other systematic uncertainties will improve as they are data based (like the efficiency related ones) or by simulating more data (like the background model related ones).

We achieve precisions on par with a similar *BABAR* analysis [8] from 2011 despite using a $\sim 14\%$ smaller dataset. As this is the first model dependent Dalitz plot analysis at Belle II, we paved the way for further such measurements.

To eventually test the Standard Model via the $K^*\pi$ isospin sum rule, requires the measurement of all four $B \to K^*\pi$ modes. $B^0 \to K^{*0}\pi^0$ and $B^0 \to K^{*+}\pi^-$ are covered in this thesis. The missing modes $B^+ \to K^{*+}\pi^0$ and $B^+ \to K^{*0}\pi^+$ can be extracted in an analog

Dalitz plot analysis of $B^+ \to K^0_S \pi^+ \pi^0$, which is currently ongoing at Belle II, following the approach developed in this thesis. Combining both analysis will allow us to test the $K^*\pi$ isospin sum rule. We expect to achieve a statistical precision of about 1% at the target Belle II dataset of an integrated luminosity of $50\,\mathrm{ab}^{-1}$. It remains to be shown whether such a measurement can find tensions with Standard Model.

A Appendix

A.1 Analysis Workflow

Figure A.1 shows the main steps in the analysis from signal reconstruction, over selection and background suppression to the fit model, its validation towards the final result.

A.2 Input Variables of the Continuum Suppression GBDT

Figures A.2, A.3 and A.4 show the input variables used in the training of the continuum suppression GBDT.

A.3 PID and π^0 Weight Tables

Figures A.5, A.6, A.7 and A.8 show the efficiency correction weights between simulated data and real data for the PID and π^0 selection requirements.

A.4 Results of the *BABAR* analysis

Table A.1 lists the central values and uncertainties as determined by the *BABAR* analysis. These values are used to compare the precision achieved in this thesis.

Table A.1: Results of the *BABAR* 2011 analysis [8]. The first uncertainty is statistical an the second is systematical.

	$\mathcal{B}$ $[10^{-6}]$	$\mathcal{A}^{CP}$
$B^0 \to K^*(892)^+\pi^-$	$8.0 \pm 1.1 \pm 0.8$	$-0.29 \pm 0.11 \pm 0.02$
$B^0 \to K^*(892)^0\pi^0$	$3.3 \pm 0.5 \pm 0.4$	$-0.15 \pm 0.12 \pm 0.04$
$B^0 \to \rho(770)^- K^+$	$6.6 \pm 0.5 \pm 0.8$	$0.20 \pm 0.09 \pm 0.08$
$B^0 \to (K\pi)_0^{*+}\pi^-$	$34.2 \pm 2.4 \pm 4.1$	$0.07 \pm 0.14 \pm 0.01$
$B^0 \to (K\pi)_0^{*0}\pi^0$	$8.6 \pm 1.1 \pm 1.3$	$-0.15 \pm 0.10 \pm 0.04$
$B^0 \to \rho(1450)^- K^+$	$2.4 \pm 1.0 \pm 0.6$	$-0.10 \pm 0.32 \pm 0.09$
$B^0 \to \rho(1700)^- K^+$	$0.6 \pm 0.6 \pm 0.4$	$-0.36 \pm 0.57 \pm 0.23$
$B^0 \to K^+\pi^-\pi^0$ non-resonant	$2.8 \pm 0.5 \pm 0.4$	$0.10 \pm 0.16 \pm 0.08$

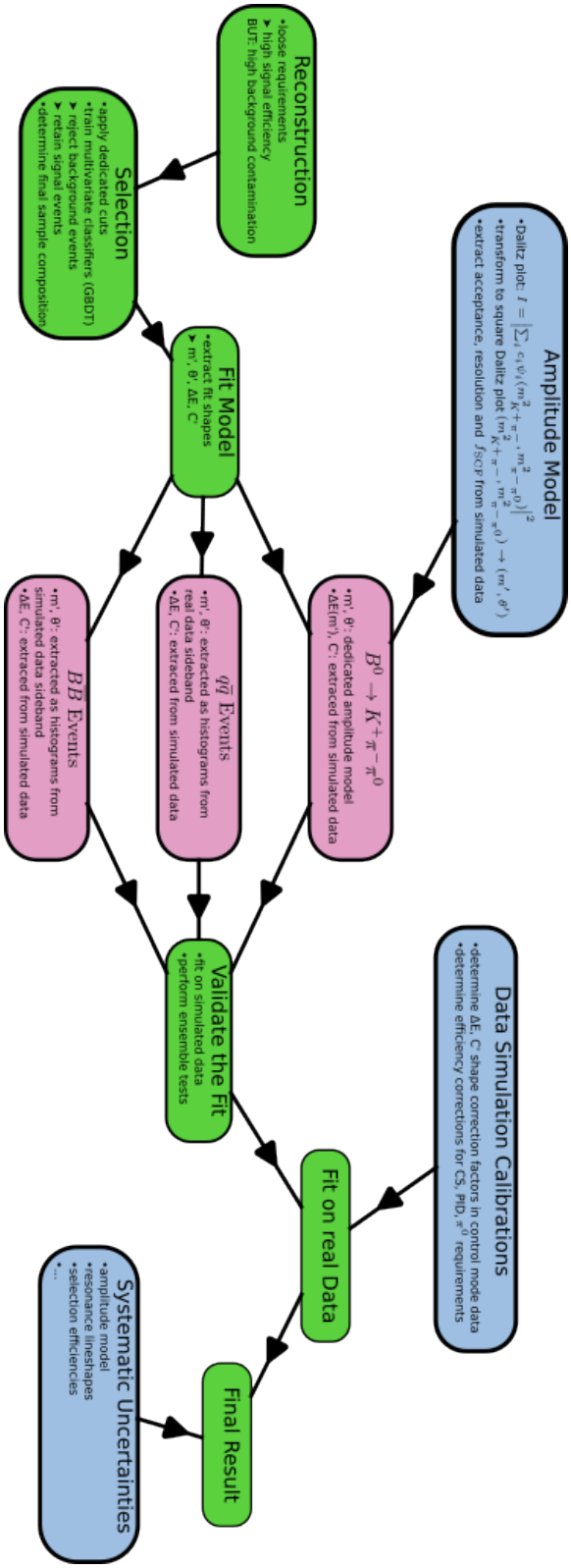

Figure A.1: Flowchart of the basic analysis steps.

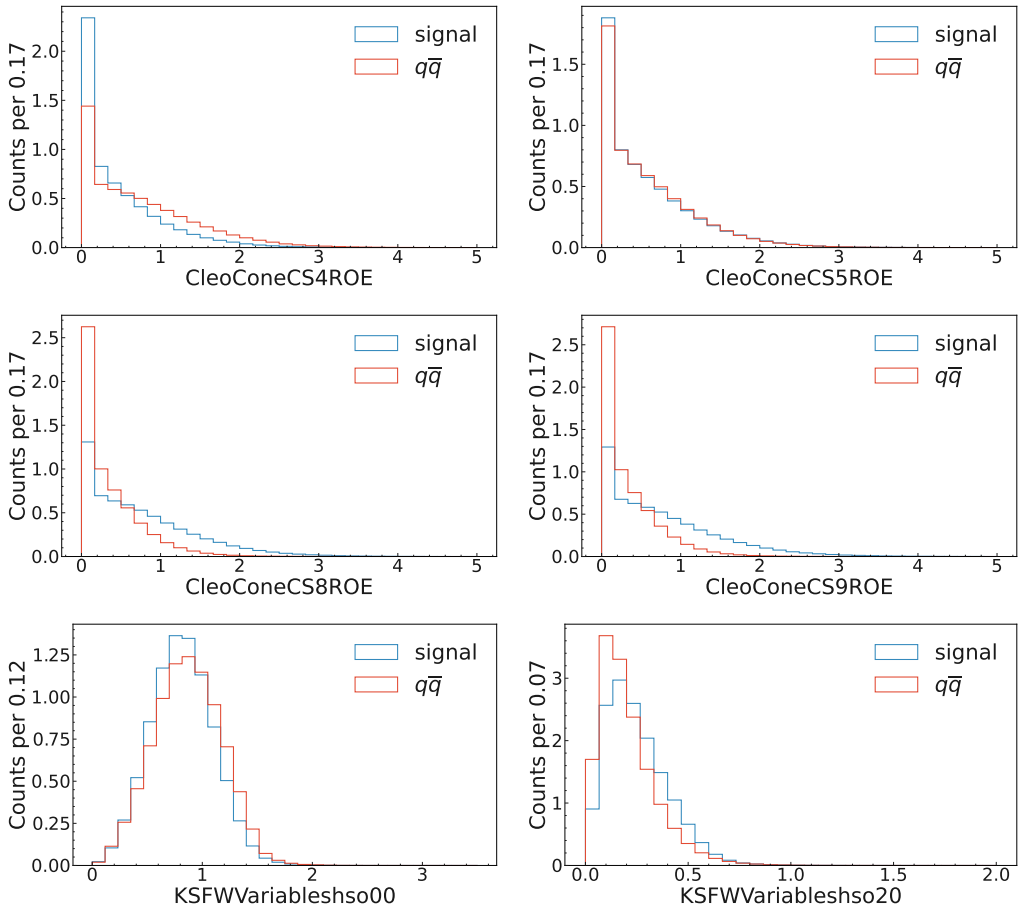

Figure A.2: Signal and $q\bar{q}$ distributions of the input variables of the continuum suppression GBDT in simulated data (1).

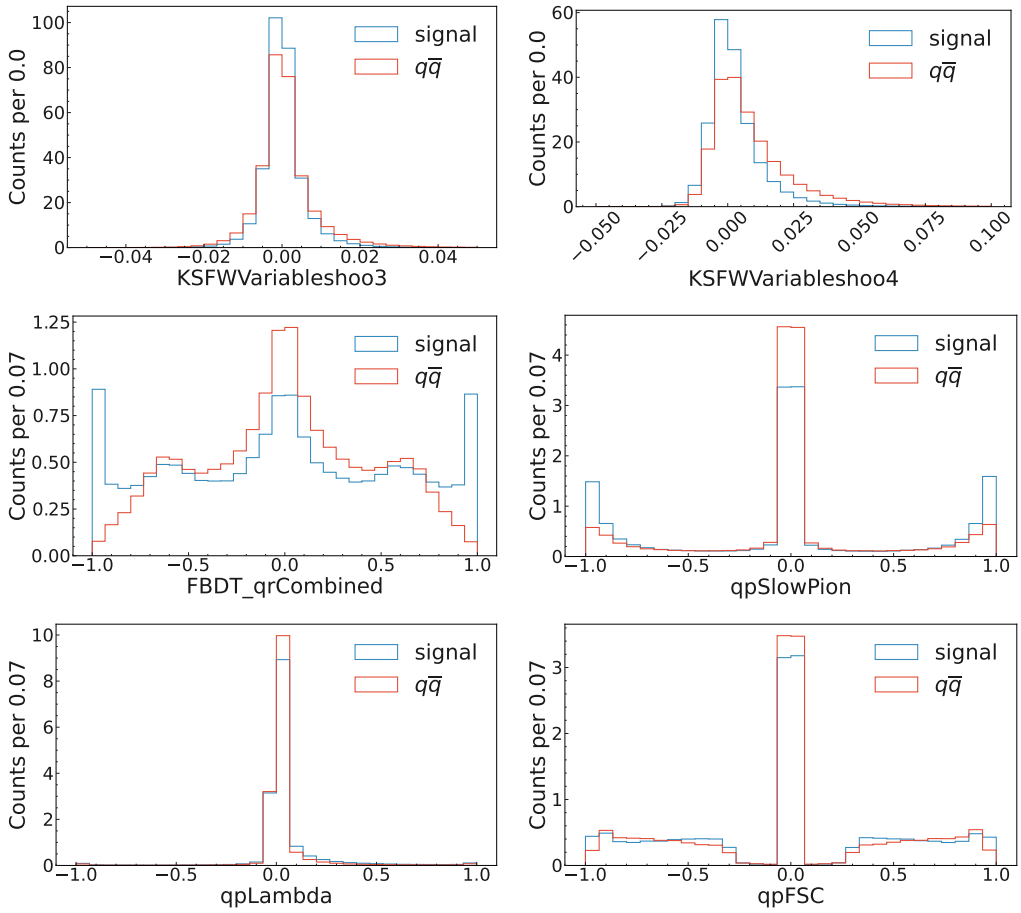

Figure A.3: Signal and $q\bar{q}$ distributions of the input variables of the continuum suppression GBDT in simulated data (2).

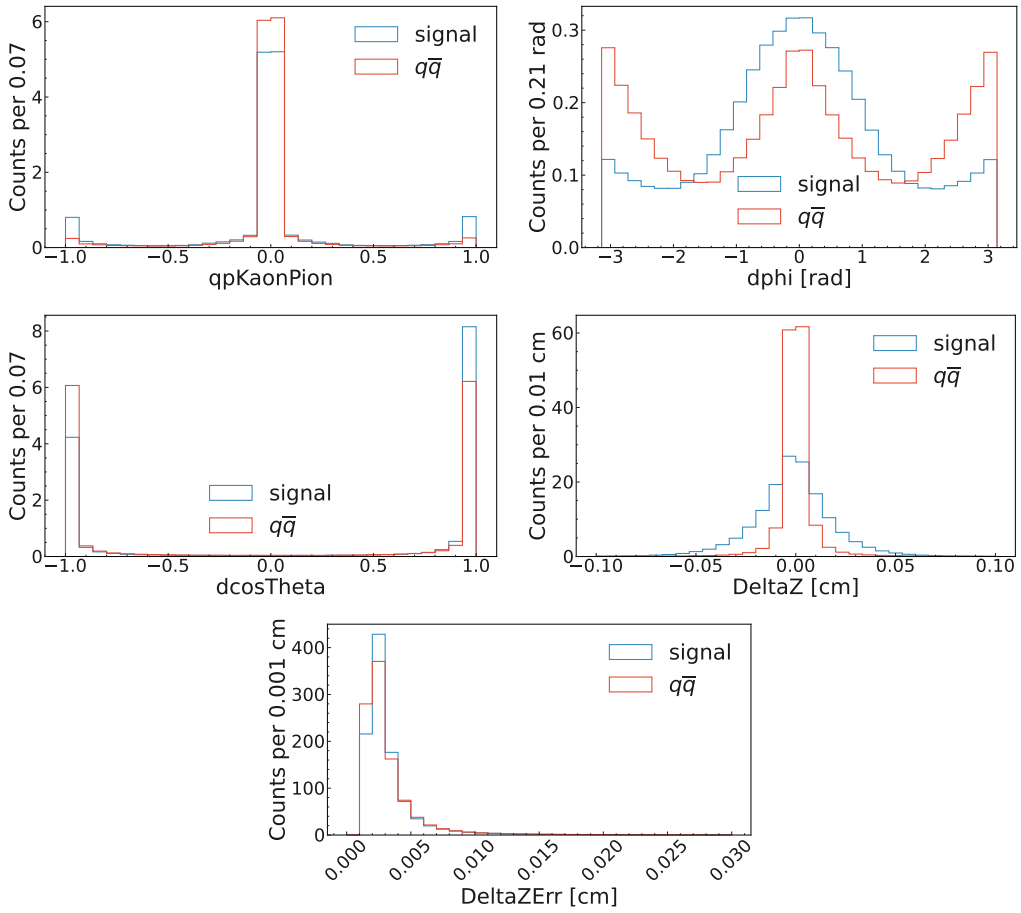

Figure A.4: Signal and $q\bar{q}$ distributions of the input variables of the continuum suppression GBDT in simulated data (3).

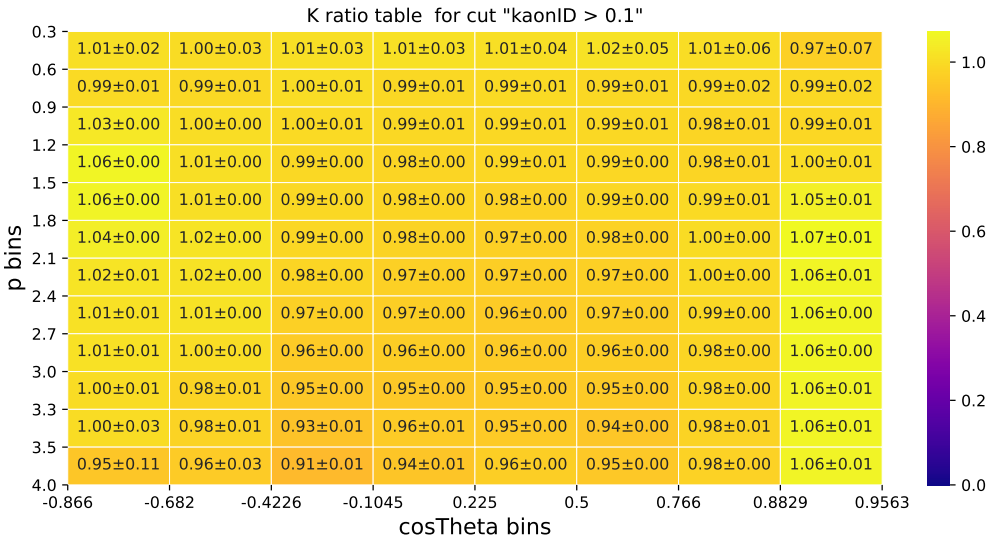

Figure A.5: Efficiency ratio in % between LS1 data and simulated data in bins of the track momentum and cosine of the polar angle for a global kaon ID requirement of 0.1. The errors are the quadratic sum of statistical and systematical errors.

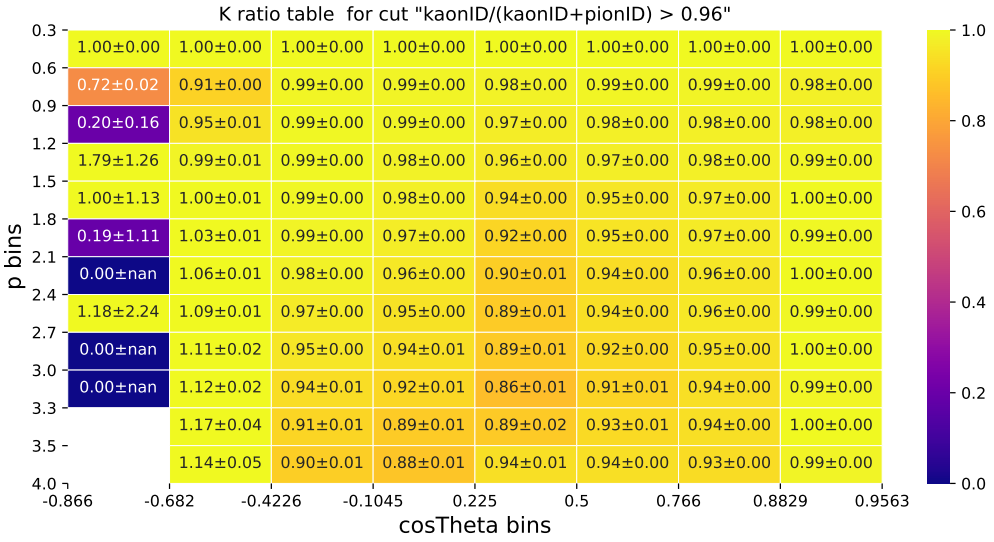

Figure A.6: Efficiency ratio in % between LS1 data and simulated data in bins of the track momentum and cosine of the polar angle for a binary kaon ID requirement of 0.96. The left-most bins suffer from low statistics of the used sample, however non of the $B^0 \to K^+\pi^-\pi^0$ decays fall into these bins. The errors are the quadratic sum of statistical and systematical errors.

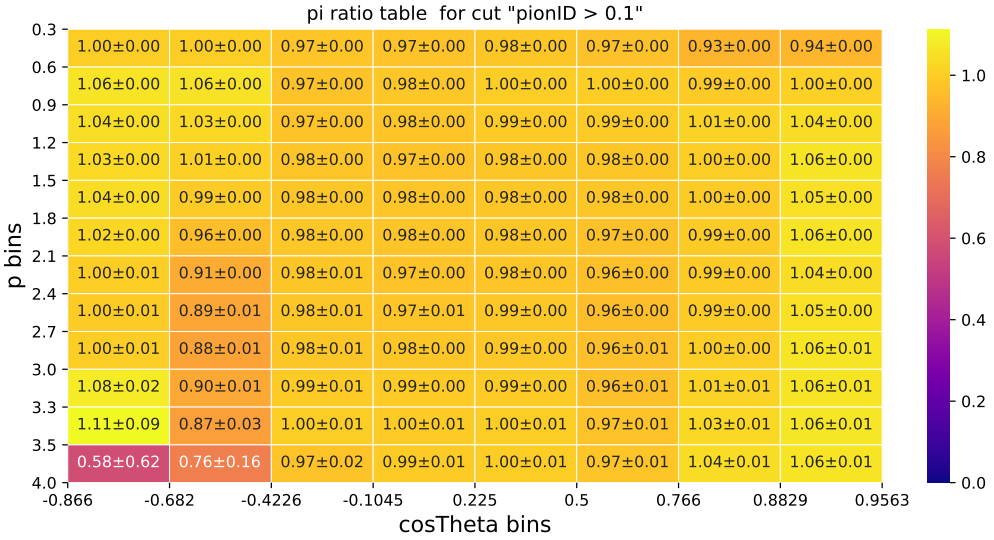

Figure A.7: Efficiency ratio in % between LS1 data and simulations in bins of the track momentum and cosine of the polar angle for a global pion ID requirement of 0.1. The errors are the quadratic sum of statistical and systematical errors.

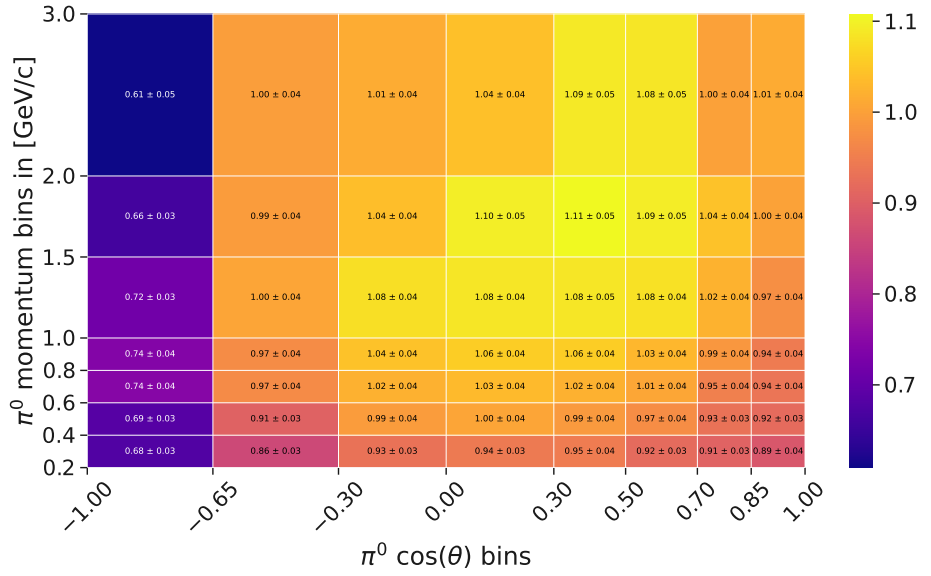

Figure A.8: Efficiency ratio in % between LS1 data and simulated data in bins of the π^0 momentum and cosine of the polar angle for our π^0 selection. The errors are the quadratic sum of statistical and systematical errors.

Bibliography

[1] ESA. *What is the Universe made of?* Dec. 2003.

[2] M. B. GAVELA et al. „STANDARD MODEL CP-VIOLATION AND BARYON ASYMMETRY“. *Modern Physics Letters A* 09.09 (Mar. 1994), pp. 795–809. ISSN: 1793-6632. DOI: 10.1142/s0217732394000629.

[3] E. Kou et al. „The Belle II Physics Book“. *Prog Theor Exp Phys (2019)* 2019.12 (Dec. 2018). DOI: 10.1093/ptep/ptz106. arXiv: 1808.10567 [hep-ex].

[4] I. Adachi et al. „Measurement of branching fractions and direct CP asymmetries for $B \to K\pi$ and $B \to \pi\pi$ decays at Belle II“. *Physical Review D* 109.1 (Jan. 2024). ISSN: 2470-0029. DOI: 10.1103/physrevd.109.012001.

[5] R.H. Dalitz. „CXII. On the analysis of τ-meson data and the nature of the τ-meson“. *The London, Edinburgh, and Dublin Philosophical Magazine and Journal of Science* 44.357 (Oct. 1953), pp. 1068–1080. ISSN: 1941-5990. DOI: 10.1080/14786441008520365.

[6] R. H. Dalitz. „Decay of τ Mesons of Known Charge“. *Physical Review* 94.4 (May 1954), pp. 1046–1051. ISSN: 0031-899X. DOI: 10.1103/physrev.94.1046.

[7] Marko Petric. „Measurement of CP Violation in Weak Decays of $B^0 \to K^+\pi^-\pi^0$ with the Belle Detector“. PhD thesis. Ljubljana U., 2014.

[8] J. P. Lees et al. „Amplitude analysis of $B^0 \to K^+\pi^-\pi^0$ and evidence of direct CP violation in $B \to K^*\pi$ decays“. *Physical Review D* 83.11 (June 2011). ISSN: 1550-2368. DOI: 10.1103/physrevd.83.112010.

[9] Hermann Nicolai. „Quantengravitation und Vereinheitlichung“ (2017). DOI: 10.17617/1.55.

[10] Virginia Trimble. „Existence and Nature of Dark Matter in the Universe“. *Annual Review of Astronomy and Astrophysics* 25.1 (Sept. 1987), pp. 425–472. ISSN: 1545-4282. DOI: 10.1146/annurev.aa.25.090187.002233.

[11] W. N. Cottingham and D. A. Greenwood. *An Introduction to the Standard Model of Particle Physics*. Cambridge University Press, July 2023. ISBN: 9781009401708. DOI: 10.1017/9781009401685.

[12] Mark Thomson. *Modern Particle Physics*. Cambridge University Press, Sept. 2013. ISBN: 9781139525367. DOI: 10.1017/cbo9781139525367.

[13] Alessandro De Angelis and Mário Pimenta. *Introduction to Particle and Astroparticle Physics*. Springer International Publishing, 2018. ISBN: 9783319781815. DOI: 10.1007/978-3-319-78181-5.

[14] *Standard Model*. (accessed: 3 April, 2024). URL: https://en.wikipedia.org/wiki/Standard_Model.

[15] P A Zyla et al. „Review of Particle Physics“. *Progress of Theoretical and Experimental Physics* 2020.8 (Aug. 2020). ISSN: 2050-3911. DOI: 10.1093/ptep/ptaa104.

[16] M. Robinson et al. *A Simple Introduction to Particle Physics*. 2008. DOI: 10.48550/ARXIV.0810.3328.

[17] E. Noether. „Invariante Variationsprobleme“. ger. *Nachrichten von der Gesellschaft der Wissenschaften zu Göttingen, Mathematisch-Physikalische Klasse* 1918 (1918), pp. 235–257. URL: http://eudml.org/doc/59024.

[18] Peter W. Higgs. „Broken Symmetries and the Masses of Gauge Bosons“. *Physical Review Letters* 13.16 (Oct. 1964), pp. 508–509. ISSN: 0031-9007. DOI: 10.1103/physrevlett.13.508.

[19] T. D. Lee and C. N. Yang. „Question of Parity Conservation in Weak Interactions“. *Physical Review* 104.1 (Oct. 1956), pp. 254–258. ISSN: 0031-899X. DOI: 10.1103/physrev.104.254.

[20] C. S. Wu et al. „Experimental Test of Parity Conservation in Beta Decay“. *Physical Review* 105.4 (Feb. 1957), pp. 1413–1415. ISSN: 0031-899X. DOI: 10.1103/physrev.105.1413.

[21] Jost, Res. „Eine Bemerkung zum CTP Theorem“ (1957). DOI: 10.5169/SEALS-112824.

[22] J. H. Christenson et al. „Evidence for the 2π Decay of the K_2^0 Meson“. *Physical Review Letters* 13.4 (July 1964), pp. 138–140. ISSN: 0031-9007. DOI: 10.1103/physrevlett.13.138.

[23] Particle Data Group. *CP Violation in K_L^0 Decays*. (accessed: 15 April, 2024). URL: https://pdg.lbl.gov/2022/reviews/rpp2022-rev-cp-viol-kl-decays.pdf.

[24] James Cronin. *CP Symmetry Violation – The Search for Its Origin*. Nobel Lecture. NobelPrize.org. Dec. 1980. URL: https://www.nobelprize.org/prizes/physics/1980/cronin/lecture/.

[25] Val Fitch. *The Discovery of Charge – Conjugation Parity Asymmetry*. Nobel Lecture. NobelPrize.org. Dec. 1980. URL: https://www.nobelprize.org/prizes/physics/1980/fitch/lecture/.

[26] Makoto Kobayashi and Toshihide Maskawa. „CP-Violation in the Renormalizable Theory of Weak Interaction“. *Progress of Theoretical Physics* 49.2 (Feb. 1973), pp. 652–657. ISSN: 0033-068X. DOI: 10.1143/ptp.49.652.

[27] Nicola Cabibbo. „Unitary Symmetry and Leptonic Decays“. *Physical Review Letters* 10.12 (June 1963), pp. 531–533. ISSN: 0031-9007. DOI: 10.1103/physrevlett.10.531.

[28] S. L. Glashow, J. Iliopoulos, and L. Maiani. „Weak Interactions with Lepton-Hadron Symmetry“. *Physical Review D* 2.7 (Oct. 1970), pp. 1285–1292. ISSN: 0556-2821. DOI: 10.1103/physrevd.2.1285.

[29] Thomas Kuhr. *Flavor Physics at the Tevatron: Decay, Mixing and CP-Violation Measurements in pp-Collisions*. Springer Berlin Heidelberg, 2013. ISBN: 9783642103001. DOI: 10.1007/978-3-642-10300-1.

[30] Lincoln Wolfenstein. „Parametrization of the Kobayashi-Maskawa Matrix“. *Physical Review Letters* 51.21 (Nov. 1983), pp. 1945–1947. ISSN: 0031-9007. DOI: 10.1103/physrevlett.51.1945.

[31] Robert Fleischer. „Flavor physics and CP violation“. *European School on High-Energy Physics*. May 2004, pp. 81–150. arXiv: hep-ph/0405091.

[32] Markus Röhrken. *Time-Dependent CP Violation Measurements: Analyses of Neutral B Meson to Double-Charm Decays at the Japanese Belle Experiment*. Springer International Publishing, 2014. ISBN: 9783319007267. DOI: 10.1007/978-3-319-00726-7.

[33] B. Aubert et al. „Observation of *CP* Violation in the B^0 Meson System“. *Phys. Rev. Lett.* 87 (9 Aug. 2001), p. 091801. DOI: 10.1103/PhysRevLett.87.091801. URL: https://link.aps.org/doi/10.1103/PhysRevLett.87.091801.

[34] K. Abe et al. „Observation of Large *CP* Violation in the Neutral B Meson System“. *Phys. Rev. Lett.* 87 (9 Aug. 2001), p. 091802. DOI: 10.1103/PhysRevLett.87.091802. URL: https://link.aps.org/doi/10.1103/PhysRevLett.87.091802.

[35] Michael Gronau. „A precise sum rule among four $B \to K\pi$ CP asymmetries“. *Physics Letters B* 627.1–4 (Oct. 2005), pp. 82–88. ISSN: 0370-2693. DOI: 10.1016/j.physletb.2005.09.014.

[36] Michael Gronau et al. „Electroweak penguin diagrams and two-bodyBdecays“. *Physical Review D* 52.11 (Dec. 1995), pp. 6374–6382. ISSN: 0556-2821. DOI: 10.1103/physrevd.52.6374.

[37] Nicolas Boisvert Beaudry et al. „The $B \to \pi K$ puzzle revisited“. *Journal of High Energy Physics* 2018.1 (Jan. 2018). ISSN: 1029-8479. DOI: 10.1007/jhep01(2018)074.

[38] Javier Virto. „Charmless Non-Leptonic Multi-Body B decays“ (2016). DOI: 10.48550/ARXIV.1609.07430.

[39] A. J. Bevan et al. „The Physics of the B Factories“ (2014). DOI: 10.48550/ARXIV.1406.6311.

[40] Charles Zemach. „Three-Pion Decays of Unstable Particles“. *Physical Review* 133.5B (Mar. 1964), B1201–B1220. ISSN: 0031-899X. DOI: 10.1103/physrev.133.b1201.

[41] G. J. Gounaris and J. J. Sakurai. „Finite-Width Corrections to the Vector-Meson-Dominance Prediction for $\rho \to e^- e^+$“. *Physical Review Letters* 21.4 (July 1968), pp. 244–247. ISSN: 0031-9007. DOI: 10.1103/physrevlett.21.244.

[42] D. Aston et al. „A study of $K^-\pi^+$ scattering in the reaction $K^- p \to K^-\pi^+ n$n at 11 GeV/c“. *Nuclear Physics B* 296.3 (Jan. 1988), pp. 493–526. ISSN: 0550-3213. DOI: 10.1016/0550-3213(88)90028-4.

[43] Bill Dunwoodie. *Fits to K pi I=1/2 S-wave Amplitude and Phase Data*. Oct. 2013. URL: https://www.slac.stanford.edu/~wmd/kpi_swave/kpi_swave_fit.note.

[44] B. Aubert et al. „Amplitude analysis of the decay $B^{\pm} \to \pi^{\pm}\pi^{\pm}\pi^{\mp}$“. *Physical Review D* 72.5 (Sept. 2005). ISSN: 1550-2368. DOI: 10.1103/physrevd.72.052002.

[45] T. Abe et al. „Belle II Technical Design Report“ (Nov. 2010). DOI: 10.48550/ARXIV.1011.0352. arXiv: 1011.0352 [physics.ins-det].

[46] Demin Zhou et al. *Luminosity performance of SuperKEKB*. 2023. DOI: 10.48550/ARXIV.2306.02692.

[47] *First particles circulate in SuperKEKB accelerator*. (accessed 8 March, 2024). URL: https://phys.org/news/2016-04-particles-circulate-superkekb.html.

[48] P. Raimondi. „Status on SuperB effort“. 2006. URL: http://www.lnf.infn.it/conference/superb06/talks/raimondi1.ppt.

[49] Karlheinz Ackermann. personal communication.

[50] Leo Piilonen. *Belle II KLM - KL and Muon Detection*. URL: https://indico.cern.ch/event/361123/contributions/856620/attachments/1135126/1625995/KLM-Piilonen.pdf.

[51] S. Jadach, B.F.L. Ward, and Z. Wąs. „The precision Monte Carlo event generator for two-fermion final states in collisions“. *Computer Physics Communications* 130.3 (Aug. 2000), pp. 260–325. ISSN: 0010-4655. DOI: 10.1016/s0010-4655(00)00048-5.

[52] Torbjörn Sjöstrand et al. „An introduction to PYTHIA 8.2“. *Computer Physics Communications* 191 (June 2015), pp. 159–177. ISSN: 0010-4655. DOI: 10.1016/j.cpc.2015.01.024.

[53] David J. Lange. „The EvtGen particle decay simulation package“. *Nuclear Instruments and Methods in Physics Research Section A: Accelerators, Spectrometers, Detectors and Associated Equipment* 462.1–2 (Apr. 2001), pp. 152–155. ISSN: 0168-9002. DOI: 10.1016/s0168-9002(01)00089-4.

[54] Elisabetta Barberio, Bob van Eijk, and Zbigniew Wąs. „Photos — a universal Monte Carlo for QED radiative corrections in decays“. *Computer Physics Communications* 66.1 (July 1991), pp. 115–128. ISSN: 0010-4655. DOI: 10.1016/0010-4655(91)90012-a.

[55] S. Agostinelli et al. „Geant4—a simulation toolkit“. *Nuclear Instruments and Methods in Physics Research Section A: Accelerators, Spectrometers, Detectors and Associated Equipment* 506.3 (July 2003), pp. 250–303. ISSN: 0168-9002. DOI: 10.1016/s0168-9002(03)01368-8.

[56] *Belle II Analysis Software Framework*. URL: https://software.belle2.org/development/sphinx/index.html.

[57] J.-F. Krohn et al. „Global decay chain vertex fitting at Belle II“. *Nuclear Instruments and Methods in Physics Research Section A: Accelerators, Spectrometers, Detectors and Associated Equipment* 976 (Oct. 2020), p. 164269. DOI: 10.1016/j.nima.2020.164269.

[58] Rainer Storn and Kenneth Price. *Journal of Global Optimization* 11.4 (1997), pp. 341–359. DOI: 10.1023/a:1008202821328.

[59] URL: https://docs.scipy.org/doc/scipy/index.html.

[60] Guolin Ke et al. „Lightgbm: A highly efficient gradient boosting decision tree“. *Advances in neural information processing systems* 30 (2017), pp. 3146–3154.

[61] A. Hoecker et al. *TMVA - Toolkit for Multivariate Data Analysis*. 2009. arXiv: physics/0703039 [physics.data-an].

[62] J.Eschle et al. *zfit*. URL: https://zfit.readthedocs.io/en/latest/index.html.

[63] Kyle S. Cranmer. „Kernel Estimation in High-Energy Physics“. *Comp.Phys.Commun. 136 (2001) 198-207* (Nov. 17, 2000). DOI: 10.1016/S0010-4655(00)00243-5. arXiv: hep-ex/0011057v1 [hep-ex].

[64] *Clebsch-Gordon Coefficients Tables*. URL: https://pdg.lbl.gov/2002/clebrpp.pdf.

[65] Belle II Collaboration. *Systematic Corrections Framework*. URL: https://syscorrfw.readthedocs.io/en/latest/index.html.

[66] Muriel Pivk and Francois R. Le Diberder. „sPlot: a statistical tool to unfold data distributions“. *Nucl.Instrum.Meth.A555:356-369,2005* (Feb. 17, 2004). DOI: 10.1016/j.nima.2005.08.106. arXiv: physics/0402083v3 [physics.data-an].

[67] Alexander Glazov et al. *Measurement of the track reconstruction efficiency and fake rate with $e^+e^- \to \tau^+\tau^-$ events*. June 2020. URL: https://docs.belle2.org/record/1867/files/BELLE2-NOTE-PH-2020-006%20%28ICHEP%29.pdf.

[68] C. Cecchi et al. *B counting measurement of the Run 1 Belle II data sample*. Apr. 2023. URL: https://docs.belle2.org/record/3468/files/BELLE2-NOTE-PH-2023-011_v2.pdf.

[69] C. Cecchi et al. *Study of R2 distribution and B counting in Early Phase 3 Data*. July 2020. URL: https://docs.belle2.org/record/1414/files/BELLE2-NOTE-PH-2019-025_v7.pdf.

[70] S. Choudhury et al. „Measurement of the B^+/B^0 production ratio in e^+e^- collisions at the $\Upsilon(4S)$ resonance using $B \to J/\psi(\ell\ell)K$ decays at Belle“. *Phys. Rev. D* 107 (3 Feb. 2023), p. L031102. DOI: 10.1103/PhysRevD.107.L031102. URL: https://link.aps.org/doi/10.1103/PhysRevD.107.L031102.

[71] Michael Eliachevitch et al. William Sutcliffe. *PIDvar*. URL: https://gitlab.desy.de/meliache/pidvar/-/tree/feature/settable-syscorr?ref_type=heads.

[72] Michael Eliachevitch. *PID Corrections and Systematic Uncertainties with PIDvar*. July 2021. URL: https://indico.belle2.org/event/3899/contributions/23592/attachments/11963/18239/pid_systematics.pdf.

[73] J. P. Lees et al. „Evidence for CP violation in $B^+ \to K^*(892)^+\pi^0$ from a Dalitz plot analysis of $B^+ \to K^0_S\pi^+\pi^0$ decays“. *Physical Review D* 96.7 (Oct. 2017). ISSN: 2470-0029. DOI: 10.1103/physrevd.96.072001.

Danksagung

Zum Schluss möchte ich noch all denen danken, ohne die die Erstellung dieser Arbeit nicht möglich gewesen wäre.

Zuerst geht mein Dank an **Professor Dr. Thomas Kuhr**, als Doktorvater, für die Möglichkeit im Belle II Experiment eine Dissertation zu erstellen.

Weiter danke ich **Dr. Hans-Günther Moser**, als Gruppenleiter der MPP Belle II Gruppe, für die Betreuung. Vielen Dank für die Unterstützung in Diskussionen in Arbeitsgruppenmeetings. Außerdem danke ich dir, dass du immer Zeit hast, um mir die physikalischen Hintergründe zu erklären, die ich nicht verstehe.

Ein großes Dankeschön geht auch an **Professor Dr. Christian Kiesling**. Dank dir habe ich erst den Weg ans MPP gefunden. Deine Faszination für Physik ist ansteckend. Deine Geduld und Art und Weise, wie du Dinge erklärst und Geschichten von früher erzählst, sorgen dafür, dass man dir stundenlang zuhören könnte.

Ein riesen Dank geht an **Dr. Stefan Wallner**. Ohne dich wäre die Analyse nicht da, wo sie jetzt ist. Dein Wissen und Verständnis über Amplituden scheint mir unermesslich. Egal welche Frage ich mir über die Analyse überlege, du findest immer eine Antwort.

Vielen Dank auch an alle anderen (ehemaligen) Mitglieder der MPP Gruppe. Ein paar möchte ich hier erwähnen: **Angie, Benedikt, Ceren, Elia, Felix, Justin, Lukas, Oskar, Philipp, Thibaud**. Ihr macht den Arbeitsalltag spaßiger und steht immer für eine Runde Kicker, Tischtennis oder Fußball zur Verfügung.

Furthermore, I'd like to thank the whole Belle II collaboration. The collaboration brings together physicists from so many different cultures in their joint endeavor to unravel nature's secrets. I'm really grateful that I got to meet so many inspiring people at collaboration meetings.

Der größte Dank, zum Schluss, geht an meine Familie. Meine Oma, **Marie Reif**, meinen Bruder, **Alexander Reif**, und meine Eltern **Edith** und **Horst Reif**. Eure Unterstützung ist bedingungslos. Egal ob moralisch oder finanziell. Ich weiß, dass egal wohin mein Weg mich führt, ihr mich immer unterstützen werdet. Ihr habt meine Faszination für Physik entdeckt und entfacht ("Andere Mop is?"). Für alles möchte ich euch Danke sagen.